STRUCTURAL AND ELECTROMECHANICAL PROPERTIES OF EPITAXIAL BIFEO3 THIN FILMS

by

Rebecca J. Sichel

A dissertation submitted in partial fulfillment of

the requirements for the degree of

Doctor of Philosophy

(Materials Science)

at the

UNIVERSITY OF WISCONSIN-MADISON

2011

Abstract

$BiFeO_3$ has coupled ferroelectric and antiferromagnetic properties. Before this multiferroic coupling can be exploited or even completely understood, it is necessary to characterize the structure and electromechanical properties. We used x-ray diffraction to study the structure of thin films of $BiFeO_3$ on $SrRuO_3$ conducting layers epitaxially deposited on a $SrTiO_3$ substrate. For 400 nm (001) oriented $BiFeO_3$ thin films, we found a rotation of the atomic planes in the entire film caused by anisotropic relaxation on the miscut substrate. Mosaic blocks several microns in size had additional small, random rotations caused by the relaxation process. Within each mosaic block we found x-ray scattering signatures of a striped ferroelectric domain structure consistent with a strained rhombohedral phase.

Time resolved synchrotron x-ray microdiffraction was used to probe the piezoelectric response of the film within a single mosaic block. We found that the out of plane d_{33} piezoelectric coefficient was uniform across the entire film (d_{33} = 53 pm/V). The local in-plane response varied widely, however. We believe the variation in the apparent d_{31} is an effect of differences in mechanical constraints for each ferroelectric domain. The variation related to the proximity of the domain to a defect, dislocation, or edge of a mosaic block as well as the neighboring polarization domains.

Forbidden x-ray diffraction reflections were observed which are incompatible with the accepted R3c symmetry of $BiFeO_3$. These reflections were characterized to determine their origin and improve our understanding of the structure. The intensity of the forbidden reflections is larger in films that are relaxed, but are present in bulk crystals of $BiFeO_3$ as well. The pseudocubic ½(111) reflection exhibits a resonant enhancement near the Fe K-edge on top of a non-resonant signal. The observed intensities were compared to structure factor calculations in which Fe cations are displaced from their positions in published structural refinements of $BiFeO_3$. A model in which neighboring Fe cations are displaced in antiparallel directions matches the intensities and wavevectors of the observed reflections. Charge disproportionation induced by oxygen vacancies is a potential driving force for these Fe displacements.

Acknowledgements

Sincere and enthusiastic thanks go to my advisor, Paul Evans, for all the encouragement, support, ideas, and patience he has given me during my graduate career. The staff at the synchrotrons provided innumerable hours of support – Zhonghou Cai, Eric Dufresne, Bernhard Adams, and Martin Holt at the APS, Kenneth Evans-Lutterodt at NSLS, and Osami Sakata at SPring-8. Thanks go to Rasmi Das, Chang-Beom Eom and Sang-Wook Cheong for providing samples. The entire Evans group has been a great help. Alexei Grigoriev and Dal-Hyun Do helped teach me x-ray scattering; Pice Chen and Ji-Young Jo were my fellow soldiers in the trenches during beamtime; and Soonjoo Seo was always there to lend a friendly word of encouragement.

Most of all, I would like to thank my family. My mother- and father-in-law, Kathy and Kevin Tissot, provided child care and hot meals which gave me time and energy to work. My father, Dan Sichel, helped by listening to the science and by asking all the not-so-stupid questions which were so easy to forget. My greatest supporter was my husband, Eric Tissot, who nagged at just the right times and offered unwavering encouragement all the rest. Writing this thesis would not have been possible without him. This thesis is dedicated to my mother Debbie and my son William – the woman who did everything for me, and the boy who taught me to happily do the same for him.

Table of Contents

Table of Figures

Chapter 1. Motivation, Background, and Methods

Bismuth ferrite ($BiFeO_3$) is one of the only single phase magnetic ferroelectric materials discovered so far that is multiferroic at room temperature. Multiferroics are materials which have two or more types of long-range electronic or magnetic ordering. [1] These types of order can include a ferroelectric polarization, a ferromagnetic magnetization, or a ferroelastic structural distortion.[2] In a multiferroic, the two properties are coupled so that by changing the magnitude or direction of one type of order, the other is also changed.[3] For example, in a magnetic ferroelectric, applying a magnetic field to switch the magnetization may also switch the direction of the electrical polarization. $BiFeO_3$ is antiferromagnetic which can cause some challenges in designing appropriate devices.[4] It is, nevertheless, being explored for applications in sensor and memory technologies.[5,6] Many implementations would use thin films, so characterizing $BiFeO_3$ thin films is vital to exploiting its properties.

$BiFeO_3$ thin films are structurally complex, making a detailed understanding of their structure an important step. The substrates available for epitaxial deposition of $BiFeO_3$ are often cubic or orthorhombic, so rhombohedral $BiFeO_3$ can be oriented on the substrate in several directions. $BiFeO_3$ thus forms multiple crystals within the same film. By introducing a miscut to modify the substrate surface, scientists have made substantial progress promoting the growth of a single variant and simplifying the film structure.[7,8] However, as soon as the ferroelectric polarization is switched, multiple structural variants can occur.

The electromechanical properties are also vital to understanding the relationship between the antiferromagnetic order in $BiFeO_3$ and applied electric field. Magnetic ordering is highly dependent on the bond angles and lengths of the magnetic ion, all of which change when a material is strained.[9] In $BiFeO_3$ this strain can arise from the piezoelectric expansion of the lattice. Understanding the structure as a function of electric field for each structural variant is essential to understanding and eventually exploiting the multiferroic properties of $BiFeO_3$.

This thesis describes studies of $BiFeO_3$ thin film structure and electromechanical properties using x-ray microdiffraction. X-ray diffraction is an accurate tool for measuring structure, and the focused beam provides enough spatial resolution to distinguish between structural variants. I used time-resolved x-ray microdiffraction techniques to measure the structure and electromechanical response from the structural variants in $BiFeO_3$ thin films. These results show that relaxation of epitaxial strain makes the in-plane lattice constants and piezoelectric response vary on a the micrometer scale. Several x-ray reflections are observed that are inconsistent with the commonly accepted symmetry of $BiFeO_3$. The weak reflections are a sign of local variations in the cation positions within the unit cell. The local changes in strain, piezoelectric response, and cation displacements mean that the multiferroic coupling will also vary locally in these films.

1.1. Motivation

Multiferroics can in principle be exploited to make memory elements that can be written using a voltage and read using a magnetic field,[10] or used in spintronics applications as tunnel junction barriers.[11] $BiFeO_3$ in particular is one of the most promising multiferroic materials because it has a large ferroelectric polarization and a significant magnetic moment on the Fe^{3+} ions.[12] $BiFeO_3$ is antiferromagnetic and ferroelectric well above room temperature. It has an antiferromagnetic to paramagnetic phase transition at a Néel temperature of $T_N = 643$ K, and a ferroelectric-paraelectric phase transition at a Curie temperature of $T_{FE} = 1143$ K.[13,14] Electrical control of the magnetism has recently been observed experimentally in both bulk and thin-film $BiFeO_3$.[12,15] The coupling between ferroelectric polarization and antiferromagnetic spin direction in $BiFeO_3$ has been theoretically predicted and experimentally demonstrated – the next step is to optimize the ferroelectric and magnetic properties and their coupling.

Thin films of $BiFeO_3$ offer the opportunity to optimize several relevant properties. The strain imposed by the substrate can change the band structure and type of magnetic ordering of thin films.[16] It is relatively easy to apply large electric fields to thin films simply because they are thin and only modest voltages are needed to switch the polarization. Thin films are more robust and do not suffer dielectric breakdown under repeated ferroelectric switching as quickly as bulk crystals.[12]

1.2. Organization of this Thesis

Thin films of $BiFeO_3$ offer opportunities for new experiments and technologies, but an important question is raised: *What is the effect of the substrate on the structure and electromechanical properties of $BiFeO_3$ thin film*s? This thesis answers this question by probing the structure and piezoelectric response of $BiFeO_3$ thin films using x-ray diffraction. I focus on $BiFeO_3$ films deposited on $SrTiO_3$ substrates because these films have moderate compressive epitaxial strains, the substrate is non-magnetic, and are the most widely studied so results can be easily compared to others' work. A mismatch between the rhombohedral $BiFeO_3$ and cubic $SrTiO_3$ symmetries makes the structure of $BiFeO_3$ on $SrTiO_3$ quite complex even before piezoelectric strain is induced.

In order to understand the electromechanical response of this complicated structure, several steps need to be taken. Descriptions of ferroelectric materials, epitaxial thin films, $BiFeO_3$, x-ray diffraction theory, and experimental methods comprise the rest of this introductory chapter. First, the structure of $BiFeO_3$ without an electric field was studied using x-ray diffraction. The effects of anisotropic relaxation on the symmetry and domain pattern are described in Chapter 2. Microdiffraction from $Pb(Zr,Ti)O_3$ thin films was conducted to characterize the dependence of the intensities of x-ray reflections on the photon energy and on the direction of the ferroelectric remnant polarization (Chapter 3). The electromechanical response of $BiFeO_3$ thin films is measured using time-resolved x-ray diffraction in Chapter 4.

Finally, the effect of the substrate on antiparallel cation displacements and rotations of the oxygen octahedra are considered and compared to the bulk structure in Chapter 5.

1.3. Ferroelectric oxides

The defining property of ferroelectric materials is a large, permanent electrical polarization that persists in the absence of an applied electric field and which can be reoriented by an applied electric field.[17] Ferroelectrics possess two or more states which are identical crystallographically but differ in electric polarization direction. Switching between states is accomplished by applying an electric field above the coercive field E_C. Under ideal conditions, when the field is removed the remnant polarization P_r, is stable in the new direction. Many, but not all, ferroelectric materials are transition metal oxides; examples of ferroelectric materials include $BaTiO_3$, $Pb(Zr,Ti)O_3$, and Rochelle salt, $NaKC_4H_4O_6$.

One classic signature of ferroelectricity is the polarization-electric field hysteresis loop. In linear dielectric materials the polarization is proportional to the applied field, but for ferroelectric materials the polarization has an additional hysteretic component. The ferroelectric polarization and coercive fields can be determined from a hysteresis loop, although care must be taken to avoid artifacts.[18,19] An electric field is applied to the sample by applying a voltage across two electrodes. The applied voltage is swept above and below E_C and the displacement current is measured. The current is normalized to electrode area and then integrated to give polarization P as a function of applied field. A schematic of an ideal hysteresis loop is shown in Figure 1.1. Note that the remnant polarization is not the same as

the maximum polarization. Polarization increases after switching at E_C because the material has a linear dielectric polarization ($P = \varepsilon E$) as well as the ferroelectric polarization.

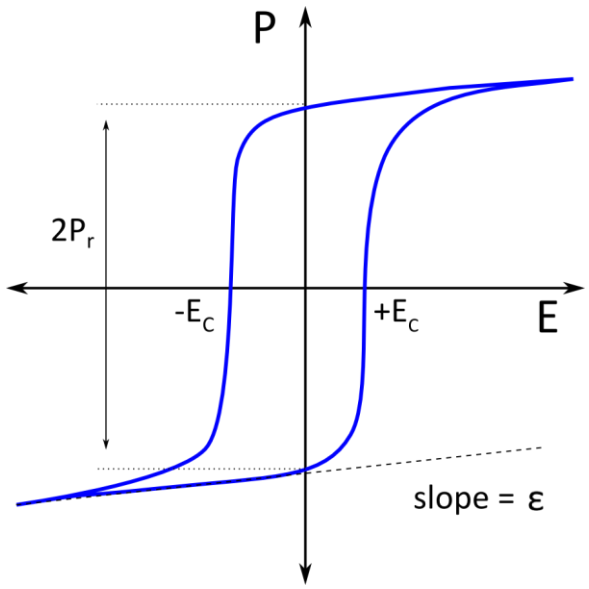

Figure 1.1. Ferroelectric hysteresis loop schematic. The coercive field E_C, where the net polarization is zero, is the field required to switch polarization direction. The remnant polarization, P_r, is the remaining polarization when zero field is applied.

Ferroelectric materials have a number of technological applications. The switchable polarization is used to store information in random access memory devices[20] and to bias transistors.[21] The piezoelectric properties have been exploited in transducers,[22] actuators,[23] and sensor applications.[24]

Only materials which are not centrosymmetric can be ferroelectric.[25] The lack of centrosymmetry produces changes in diffracted intensities of x-ray reflections that would be identical in a centrosymmetric material. For example, the intensities of the (002) and the

(00-2) reflections are different in $Pb(Zr,Ti)O_3$ thin film capacitors.[26] Chapter 3 explores the effects of polarization reversal in the model ferroelectric material $Pb(Zr,Ti)O_3$.

The polarization of a ferroelectric material is rarely homogeneous – typically, it is split into regions of uniform polarization called domains which differ in polarization direction from one another. Ferroelectric domains are regions which have uniform parallel polarization in the absence of an external electric field. In thin films, ferroelectric domains are the result of a competition between the energy required to create the depolarization field outside the material and the energetic cost of creating boundaries between neighboring regions of different polarization directions.[17] The depolarization energy is minimized when the net polarization is zero, so a material could theoretically reduce this energy by making infinitely thin domains of opposite polarization direction. Boundaries between polarization domains also require energy to form, however. The region between domains, called a domain wall, can be strained by the neighboring domains.[27] As a result of the competition between the depolarization field and the domain wall formation energy, ferroelectric thin films often form repeating lamellar patterns of domains.[28,29] In the x-ray microdiffraction studies of Chapter 2, we observe the structural signatures of these repeating domain patterns.

Ferroelectric materials are also piezoelectric, meaning voltage appears across the sample when it is mechanically stretched or compressed. In the converse piezoelectric effect, the lattice expands or contracts when an electric field is applied. Piezoelectric strain is linearly proportional to the applied electric field. Other phenomena such as electrostriction can also contribute to the strain, especially at high fields.[30] At electric fields less than or equal to the coercive field, the contribution of electrostriction to strain is small in the

materials considered here. In Chapter 4, I determine the piezoelectric strain of $BiFeO_3$ thin films by measuring the change in lattice constants using x-ray diffraction while an electric field is applied to a ferroelectric capacitor.

1.4. The perovskite structure

Many multiferroics have a crystal structure similar to the mineral perovskite, in which a transition metal is the central atom of a cubic or nearly cubic unit cell.[31] A large number of fluoride based materials are magnetic ferroelectrics, but as of yet none have magnetic and ferroelectric ordering at room temperature.[32] Perovskites that are magnetic ferroelectrics in particular are quite rare because the partially filled d orbitals of the transition metal, which lead to magnetic ordering, tend to eliminate the cation displacement that causes ferroelectricity.[33] Bismuth-based multiferroics avoid this problem, since the ferroelectricity arises from the bismuth $6s^2$ orbitals.[34]

Perovskites are a broad class of materials with the general formula ABX_3. The perovskite mineral has a cubic structure with Pm-3m symmetry. The cubic symmetry is easily distorted, however, because the structure can accommodate ions of many different elements. As a result materials with tetragonal, orthorhombic, monoclinic, and rhombohedral symmetry are all found in nature.[35,36] The perovskite structure is robust and will expand, contract, and rotate bond angles in order to accommodate a wide range of cation sizes.

The family of oxides with perovskite-derived structures has a variety of fascinating properties. Ferroelectricity, large dielectric constants, superconductivity, ferromagnetism,

and antiferromagnetism have all been observed in materials with the perovskite structure.[9] The versatility of the perovskite structure makes it sensitive to forces which may be too weak to have significant effects in other structures. Thus, small displacements and distortions from the ideal structure are an important factor in understanding and manipulating the wide variety of properties in these materials.

In the ideal perovskite structure, the cubic unit cell has A site atoms in the corners of the cube, a B site atom in the center, and oxygen atoms centered on the faces of the cube. This is called the aristotype structure and is shown below in Figure 1.2. Most materials that are described as having a perovskite structure deviate from the aristotype slightly. The modified structure is called a hettotype.[37] Hettotypes can differ from the aristotype in many ways; changes to the lattice constants, non-cubic symmetry, and displacements of the A or B atoms.

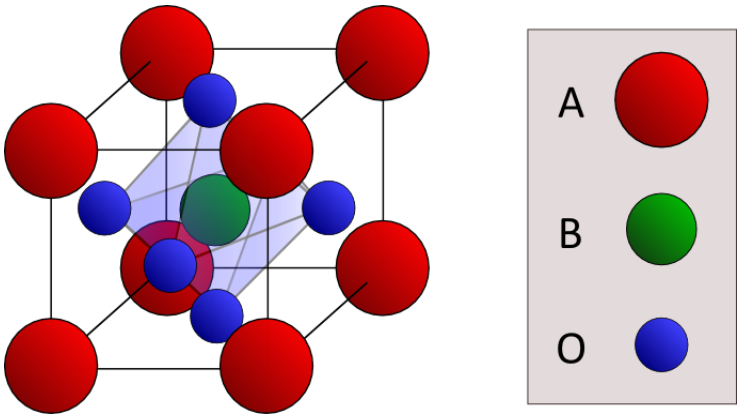

Figure 1.2. Perovskite structure ABO_3. $SrTiO_3$ and $CaRbF_3$ form this ideal cubic structure, unlike the mineral perovskite itself ($CaTiO_3$).

Two parameters are commonly used to describe how well a material fits in the perovskite structure. The tolerance factor, t, quantifies the degree to which a particular ABO_3 compound fits in this structure:

$$t = \frac{r_A + r_O}{\sqrt{2}(r_B + r_O)}$$

where r_A, r_B, and r_O are the A site, B site, and oxygen ionic radii, respectively. [38,39] Most materials that are stable in the perovskite structure have tolerance factors between 0.75 and 1.05. $BiFeO_3$ has a tolerance factor of 0.95. The ratios between A and B ionic radii and r_B/r_O are also important in stabilizing the perovskite structure.[40] If the B radius is too small, then the oxygen octahedra are unstable due to oxygen-oxygen ionic repulsion. A site atoms that have radii less than $r_A < \sqrt{2}(r_B + r_O)/r_O$ can be accommodated to some extent by rotations of oxygen octahedra.[37] Compressive strain can also be accommodated by increasing the rotation angle.

One of the more common modifications to the aristotype is the distortion or rotation of the oxygen octahedra. Rotations can be caused by A or B site atoms which do not fit, polar displacements of the A or B site atom, highly directional bonds (for example Pb^{2+} or Bi^{3+} on the A site), and Jahn-Teller distortions of the BO_6 octahedra. Tilt systems are described in terms of rotations of the octahedra about the ***a***, ***b***, and ***c*** lattice vectors in the notation used by Glazer.[41] A tilt system with rotations about each axis is written $a^+ b^+ c^+$. The first, second, and third letter represent a rotation about the ***a***, ***b***, and ***c*** axis respectively. Rotations of the same magnitude about different axes are indicated by using the same letter, such as $a^+a^+c^+$. The superscript is + when octahedra along the same axis have identical rotations about that

axis. A superscript of – indicates an equal but opposite rotation in adjacent octahedra, and a 0 superscript means no rotation about that axis. Glazer described 23 tilt systems found in a 2×2×2 pseudocubic unit cell structure, although Woodward later found there are only 15 systems in which it is possible to keep octahedra of neighboring cells connected.[42,43]

In this thesis, I study two members of the perovskite family, $BiFeO_3$ and $Pb(Zr,Ti)O_3$. In both of these materials the B-site atom is not located at the center of the unit cell, which creates a ferroelectric dipole. $Pb(Zr,Ti)O_3$ is the simpler of the two structures – it is tetragonal, has an elongated ***c*** axis, and the octahedron is distorted and displaced along the ***c*** axis along with the B site atom. $BiFeO_3$ is rhombohedral and has distortions along the pseudocubic [111] direction. In the next section, I describe the structure and properties of $BiFeO_3$ in detail.

1.5. Bismuth ferrite

1.5.1. Bulk single crystal $BiFeO_3$

The structure of bulk $BiFeO_3$ is commonly described in three different geometrical ways. The most accurate description is that $BiFeO_3$ is rhombohedral at room temperature with the space group R3c. This is equivalent to the hexagonal setting often used by crystallographers, which has six formula units of $BiFeO_3$ in the hexagonal cell and lattice constants of $\boldsymbol{a_{hex}}$ =5.579 Å and $\boldsymbol{c_{hex}}$ = 13.869 Å. However, the most intuitive view of the structure is found by comparing the pseudocubic setting of $BiFeO_3$ to the perovskite

aristotype. The pseudocubic setting contains one formula unit of $BiFeO_3$ and is nearly cubic (but technically rhombohedral) with a_{pc} = 3.96 Å and α_{pc} = 89.4°. Bi^{3+} and Fe^{3+} sit on the A and B sites respectively and are both displaced in the same direction along the $[111]_{pc}$. The oxygen octahedron is flattened in the same direction, most likely by ionic repulsion from the Bi lone pair.[37] Octahedra are rotated in alternating directions about the [111] axis by 13°, corresponding to the $a^-a^-a^-$ tilt system in the Glazer notation. Two pseudocubic unit cells are shown below in Figure 1.3.

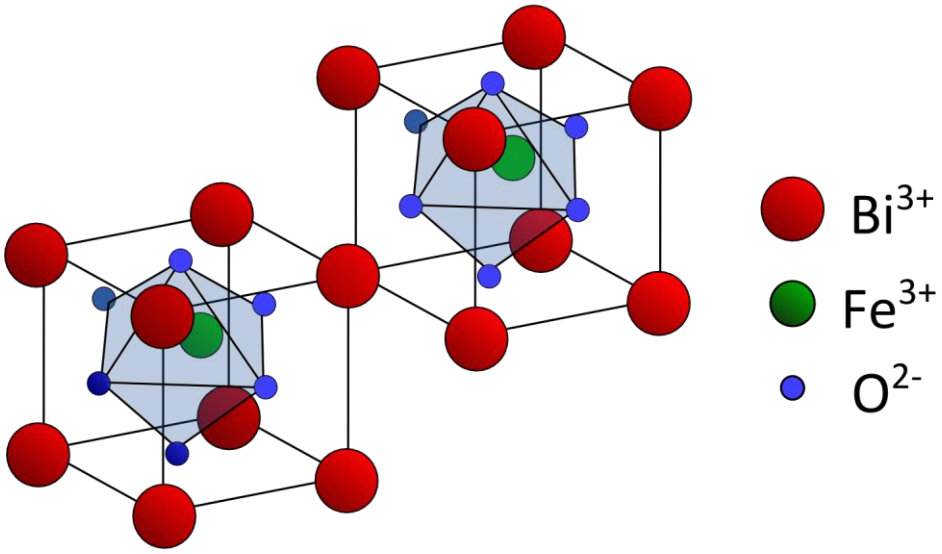

Figure 1.3. Structure of $BiFeO_3$. Two pseudocubic unit cells are shown. Oxygen octahedra are shaded blue.

It has been known for several decades that bulk $BiFeO_3$ is ferroelectric, but it was not until recently that the observed properties[12] came close to theoretical predictions of large remnant polarizations.[34] In bulk crystals, $BiFeO_3$ has a remnant polarization up to 100 $\mu C/cm^2$ parallel to the $[111]_{pc}$ axis and a coercive field of 12 kV/cm.[12] The remnant

polarization is extremely large and is approximately equal to the polarization of common ferroelectrics such as $Pb(Zr,Ti)O_3$ and $BaTiO_3$ that are currently used for ferroelectric memories. The coercive field in bulk $BiFeO_3$ is much smaller than in thin films, similar to other ferroelectric materials.

Despite the large amount of research done on $BiFeO_3$, questions about the type of antiferromagnetic ordering still remain. The antiferromagnetism of $BiFeO_3$ results in magnetic reflections in neutron diffraction.[44,45] $BiFeO_3$ is a G-type antiferromagnet; spins on Fe^{3+} ions are antiparallel to all their nearest neighbors creating planes of parallel spin along the $(111)_{pc}$ planes. This is the $(001)_{hex}$ plane in the hexagonal setting of the crystal.[46] This description proved to be incomplete; neutron scattering evidence for an additional spin spiral with a period of 62 nm was discovered by Sosnowska et al. in 1982.[47] There is still some debate in the literature of whether the magnetic modulation is cycloidal, elliptic, or even a spin density wave.[48,49] Nevertheless, all evidence points to short range antiparallel coupling between Fe^{3+} nearest neighbors.

Coupling between the ferroelectric and antiferromagnetic ordering in $BiFeO_3$ is also linked to the structure. The ferroelectric polarization direction has been shown to be linked to the antiferromagnetic wavevector in $BiFeO_3$ thin films. The spin direction and spiral wavevector can be changed by applying an electric field to switch the ferroelectric polarization direction.[12] The plane of parallel spins then switches so that the plane remains perpendicular to the polarization.[15] The magnetic ordering is strongly influenced by the Fe-

O-Fe bond as described in the double exchange model.[50] In $BiFeO_3$, density functional theory calculations suggest that the magnetic interaction is sensitive to the tilt and rotation of the FeO_6 oxygen octahedra.[51] One prominent consequence of the multiferroic order of $BiFeO_3$ would be the magneto-electric effect, in which the net magnetization would be changed by applying an electric field, or the polarization increased by applying a magnetic field.[52,53] Although the linear magneto-electric effect is supposedly forbidden by the symmetry of bulk $BiFeO_3$,[54,55] a linear effect in $BiFeO_3$ films has been reported.[56,57,58]

Problems with bulk single crystals have lead researchers to focus on thin films of $BiFeO_3$. Although the intrinsic ferroelectric and magnetic properties of bulk single crystals and epitaxial thin films are similar, the single crystals may prove difficult to use in practical applications. The biggest problem with single crystal $BiFeO_3$ is in the leakage and fatigue properties. Lebeugle *et al.* found that $BiFeO_3$ bulk crystals are susceptible to mechanical damage caused by repeated polarization reversal.[12] The large changes in shape result in the formation of cracks and defects during the switching process.[12] The defects have much smaller resistivities, so during successive electrical cycling the leakage current heats and degrades the sample, decreasing the remnant polarization. Lebeugle *et al.* showed that the remnant polarization in single crystals can initially reach up to 100 $\mu C/cm^2$, but show appreciable degradation after even one switching cycle.[12] In comparison, (111)-oriented thin films grown on $SrTiO_3$ have remnant polarizations up to 95$\mu C/cm^2$ and can withstand billions of cycles of polarization switching.[59] In other film orientations, the out-of-plane remnant

polarization is consistent with a simple geometric projection of the <111> onto the film normal. The desirable ferroelectric, piezoelectric, and magnetic ordering are almost the same as the bulk, but the improvement in fatigue properties and decrease in leakage current makes the thin films more useful than the bulk material.

1.5.2. $BiFeO_3$ thin films

$BiFeO_3$ thin films have lower leakage currents and better resistance to fatigue than bulk crystals, but the other properties are essentially the same. Early reports did show a dependence of net magnetization and polarization on film thickness.[56] However, later first-principles calculations using density functional theory predicted very little change of P and M as a function of strain.[60] Epitaxial strain rotates the polarization direction of (001) $BiFeO_3$ films, but does not have a significant effect on the magnitude of the polarization.[61] Further experimental studies of films with thicknesses ranging from 40 nm to 960 nm confirmed that there was very little change in the magnitude of the polarization, although they found the coercive field decreases with thickness.[62] Even the orientation of the film does not change the magnitude of the spontaneous polarization. The out-of-plane remnant polarizations for (111), (101), and (001) $BiFeO_3$ films were measured by Li *et al.*[63] were found to be $P_{111} \approx 100\ \mu C/cm^2$, $P_{101} \approx 80\ \mu C/cm^2$, and $P_{001} \approx 55 \mu C/cm^2$. These values are consistent with a spontaneous polarization along $[111]_{pc}$ being projected on the different out of plane directions, which predicts that $P_{111} \approx \sqrt{2}\ P_{101} \approx \sqrt{3} P_{001}$. It was thought that epitaxial strain in thin films of $BiFeO_3$ might induce ferromagnetism, which would be much easier to detect and

manipulate in potential applications such as multistate memory.[64] The antiferromagnetic ordering in $BiFeO_3$ has proved to be quite robust despite initial reports of switching magnetization using an electric field.[56]

Epitaxial $BiFeO_3$ films can remain coherent above the critical thickness predicted by Matthews and Blakeslee.[65] Matthews and Blakeslee provide an estimate for the maximum thickness for which thin films can remain strained to the lattice constant of the substrate, based on the elastic energy stored in the film. We can apply this method to $BiFeO_3$ on $SrTiO_3$. Assuming that the Poisson ratio of $BiFeO_3$ is 0.3 and misfit dislocations have [110] type Burgers vectors, the thickest defect free film is expected to be 5-15 nm. Coherent, metastable films up to 70 nm have been observed experimentally.[66] Possible explanations for the stability of thicker films include misfit dislocations with large nucleation energies, rotation of the oxygen octahedra to reduce the lattice constant,[37] or non-stoichiometry in the film accommodating strain.[67]

Partially relaxed films offer an opportunity to learn how strain affects the structural, ferroelectric, and magnetic properties. Whether induced by thickness or less than optimal growth conditions, relaxation of epitaxial films affects the magnetic ordering of $BiFeO_3$ films. The magnetic moment depends on strain. In epitaxial $BiFeO_3$ films on $SrTiO_3$ substrates, the saturation magnetization decreases as the film relaxes.[68] X-ray linear dichroism measurements of antiferromagnetic and ferroelectric domains in strained 200 nm and relaxed 1 μm-thick $BiFeO_3$ films indicate that the epitaxial strain in the thinner films changes the type

of antiferromagnetic ordering.[69] The energetic degeneracy for the spin direction within the (111) plane is lifted when epitaxial strain is applied, and there is an easy axis of magnetization along the <112> direction.

1.6. Calculating x-ray scattering intensities

The work in this thesis largely consists of using x-ray diffraction to determine structural parameters including lattice constants, symmetry, and polar displacements. Many of the experiments compare experimental diffracted x-ray intensities to predicted intensities in order to determine the validity of different structural models. In this section, I outline the how the intensities of x-ray reflections can be calculated. Using these equations, I predict how reflections can be split by the presence of multiple ferroelectric domains (Chapter 2), the energy dependence of reflections and the effect of polarization direction (Chapter 3), piezoelectric strain (Chapter 4), and the origin of scattered intensity at ½(*hkl*) type reflections (Chapter 5).

Calculating the x-ray scattering intensity starts with the scattering from an atom, then all the atoms in the crystal's unit cell, and then from the unit cells in the entire crystal. When an x-ray is elastically scattered, we measure the intensity and angle of the scattered beam. The difference in momentum between the incident ($\boldsymbol{k_0}$) and scattered wavevector ($\boldsymbol{k'}$) makes a vector in reciprocal space, $\boldsymbol{q}$, such that $\hbar\boldsymbol{q} = \hbar\boldsymbol{k}' - \hbar\boldsymbol{k}_0$. The three-dimensional components $\boldsymbol{q_x}$ $\boldsymbol{q_y}$ and $\boldsymbol{q_z}$ are related to the x-ray wavelength and angles labeled in Figure 1.4.

$$q_x = \frac{1}{\lambda}(\cos\beta\cos\gamma - \cos\alpha)$$

$$q_y = \frac{1}{\lambda}(\cos\beta \sin\gamma)$$

$$q_z = \frac{1}{\lambda}(\sin\beta + \sin\alpha)$$

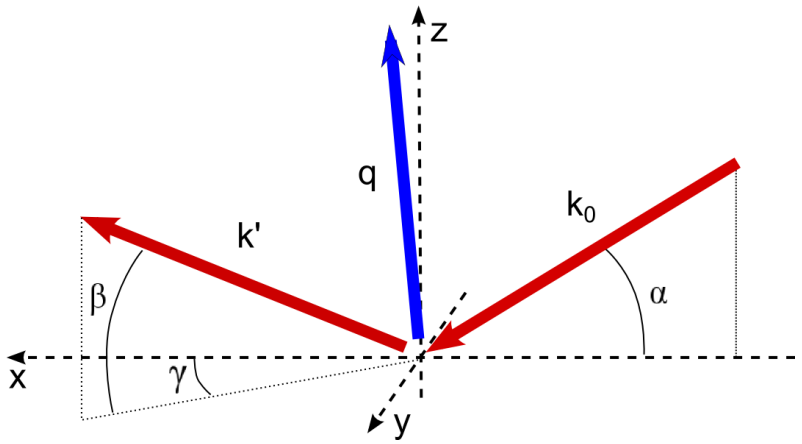

Figure 1.4. Definition of q, scattering angles and incident and scattered x-ray wavevectors. α is the incident angle and β is the scattered angle such that $\alpha+\beta = 2\theta_{Bragg}$. γ is the azimuthal angle, and is generally small or zero.

The units of ***q*** are 1/Å, such that $|q| = 2\sin\theta/\lambda = 1/d$. This last relation can be rearranged to form Bragg's Law $\lambda = 2d \sin\theta$, which gives the relation between the scattered angle 2θ and the interplanar spacing.

1.6.1. Atomic scattering factors

The scattering from an atom is the sum of scattering from all the electrons bound to it. The atomic scattering factor is expressed in units of r_0, the Thompson scattering length. Consequently, the atomic scattering factor depends on a number of factors; the element and bonding of electrons in the scattering atom, the wavevector transfer ***q***, and the photon energy. All of these are summed up in a single atomic scattering factor, *f*.

$$f(q,E) = f^0(q) + f'(E) - if''(E)$$

where f^0 is the part dependent on $\boldsymbol{q}$, f' and f'' are the real and imaginary parts of the energy dependent portion, respectively.

f^0 is approximately the total number of electrons bound to the atom at $\boldsymbol{q} = 0$, and goes to zero as $\boldsymbol{q}$ increases. f^0 can be approximated very well by the sum of three exponential functions with coefficients found by Cromer and Mann.[70] These functions fit observed values of f^0 for $|\boldsymbol{q}|$ less than 2.0 Å^{-1}. At large $|\boldsymbol{q}|$ or for ionized elements, f^0 is better described by Waasmeier and Kirfel's fitting parameters[71] which are discussed in more detail in Section 3.5.

f' and f'' are collectively called the dispersion correction and are assumed to be independent of $\boldsymbol{q}$. Dispersion corrections for many elements have been calculated and are tabulated for x-ray energies between 10 and 30,000 eV.[72] The effect of the dispersion correction on the intensity of Bragg reflections is examined in Section 3.1.2. Typically, it does not have a large effect unless the x-ray energy is close to an absorption edge of an element in the material.

1.6.2. Structure factor

The structure factor is the superposition of the scattered wave from each atom in the unit cell:

$$F_{hkl} = \sum_{r_n} f_n \, e^{2\pi i \boldsymbol{q} \cdot \boldsymbol{r_n}}$$

where $\boldsymbol{q}$ is the wavevector transfer and f_n are the atomic scattering factors for each atom *n*. $\boldsymbol{r}_n$ is the position for the *n*th atom and can be written as a linear superposition of the direct lattice vectors $\boldsymbol{a}$, $\boldsymbol{b}$, and $\boldsymbol{c}$.

$$\boldsymbol{r} = u\boldsymbol{a} + v\boldsymbol{b} + w\boldsymbol{c}$$

The set (*u*,*v*,*w*) are called the fractional indices of the atomic position. The origin (where $\boldsymbol{r}$ = 0) is conventionally taken to be one of the corners of the cubic unit cell. For example, the body-centered atom in a bcc unit cell would have (*uvw*) = (0.5, 0.5, 0.5).

When $\boldsymbol{q}$ is exactly equal to a reciprocal lattice vector $\boldsymbol{g_{hkl}} = h\boldsymbol{a}^* + k\boldsymbol{b}^* + h\boldsymbol{c}^*$ the structure factor is simplified to

$$F_{hkl} = \sum_{r_n} f_n \exp[2\pi i(h\boldsymbol{a}^* + k\boldsymbol{b}^* + h\boldsymbol{c}^*) \cdot (u_n\boldsymbol{a} + v_n\boldsymbol{b} + w_n\boldsymbol{c})]$$

$$F_{hkl} = \sum_{r_n} f_n \exp[2\pi i(hu_n + kv_n + lw_n)]$$

because the reciprocal lattice vector $\boldsymbol{a}^* = \boldsymbol{b} \times \boldsymbol{c}/V_{cell}$ and is orthogonal to $\boldsymbol{b}$ and $\boldsymbol{c}$. The intensity of a reflection is proportional to *FF**, where *F** is the complex conjugate of the structure factor. The sign of the imaginary component in *F** is reversed for f_n and the phase factor.

X-ray diffraction textbooks including Warren,[73] Als-Nielsen,[74] Guinier,[75] and Cullity[76] differ slightly in their definitions of $\boldsymbol{q}$ and the structure factor F_{hkl}. The definitions are different in 1) the sign of $\boldsymbol{q}$ and the sign of the phase factor in F_{hkl} , and 2) whether a factor of $2\pi/\lambda$ is included in the definition of q or in the phase factor in F_{hkl}. No matter which convention is chosen, the correct phase factor is $\exp[+2\pi i\,(h\boldsymbol{a}^*+k\boldsymbol{b}^*+l\boldsymbol{c}^*)(u\boldsymbol{a}+v\boldsymbol{b}+w\boldsymbol{c})]$.

1.6.3. Lattice sum

The scattering from the entire crystal is the superposition of the scattering from each unit cell. To illustrate this more clearly, I first consider the scattering from a one-dimensional line of M_1 unit cells along the $\boldsymbol{a}$ direction. The scattering from the crystal is the superposition of the scattered waves from each unit cell:

$$S_N = \sum_{m_1=0}^{M_1-1} F_{hkl} \exp[2\pi i\, \boldsymbol{q} \cdot \boldsymbol{R}_{m_1}]$$

where $\boldsymbol{R}_{m_1} = m_1 \boldsymbol{a}$. The sum can be rewritten as a geometric series

$$S = a + ar + ar^2 \ldots + l = \frac{rl - a}{r - 1}$$

so the sum over m_1 becomes

$$S_N = F_{hkl} \frac{\exp[2\pi i\, \boldsymbol{q} \cdot M_1 \boldsymbol{a}] - 1}{\exp[2\pi i\, \boldsymbol{q} \cdot \boldsymbol{a}] - 1}$$

Generalizing to three-dimensional parallelpiped with M_2 cells along the $\boldsymbol{b}$ direction and M_3 along the $\boldsymbol{c}$ direction,

$$S_N = F_{hkl} \frac{\exp[2\pi i\, \boldsymbol{q} \cdot M_1 \boldsymbol{a}] - 1}{\exp[2\pi i\, \boldsymbol{q} \cdot \boldsymbol{a}] - 1} \; \frac{\exp[2\pi i\, \boldsymbol{q} \cdot M_2 \boldsymbol{b}] - 1}{\exp[2\pi i\, \boldsymbol{q} \cdot \boldsymbol{b}] - 1} \; \frac{\exp[2\pi i\, \boldsymbol{q} \cdot M_2 \boldsymbol{c}] - 1}{\exp[2\pi i\, \boldsymbol{q} \cdot \boldsymbol{c}] - 1}$$

As M approaches infinity, as in a large single crystal, the lattice sum can be approximated by a series of delta functions when $\boldsymbol{q}$ equals a reciprocal lattice vector $\boldsymbol{g_{hkl}}$. The scattered intensity is proportional to the scattering amplitude times its complex conjugate.

In order to compare calculated scattering amplitudes to real numbers of diffracted photons, I calculate the structure factor at a reciprocal lattice vector $\boldsymbol{g_{hkl}}$ and compute the intensity. For a small number of cells, I calculate the structure factor of the atoms of the

structure by building a supercell made up of many unit cells separated by lattice vectors (Chapter 3). For large numbers of unit cells, I typically omit the lattice sum and approximate $I = F_{hkl} F^*_{hkl}$, since the lattice sum essentially picks out F_{hkl} at each reciprocal lattice vector. This does ignore the problems of mosaic spread in the crystal, dynamical diffraction, and the effect of the film thickness. However, unless otherwise noted, the films studied here are sufficiently thick and imperfect so thickness fringes and dynamical effects cannot be observed. The issue of mosaic spread is addressed by comparing the integrated intensity of the experimentally observed diffraction peak to the calculated maximum intensity at $\boldsymbol{q} = \boldsymbol{g}_{\boldsymbol{hkl}}$.

1.7. Experimental methods

X-ray diffraction was used to characterize the structure and electromechanical properties of $BiFeO_3$ thin films. To completely understand the x-ray scattering, we investigated the effects of polarization reversal on the diffracted intensity in $Pb(Zr,Ti)O_3$ thin film capacitors. Hysteresis loops were taken to characterize the $BiFeO_3$ and $Pb(Zr,Ti)O_3$ capacitors and measure the coercive fields. The steady-state structure of $BiFeO_3$ films was probed with area-averaged diffraction techniques as well as synchrotron microdiffraction. Next, time resolved x-ray microdiffraction was synchronized with electric fields applied to $BiFeO_3$ thin film capacitors to measure the piezoelectric response on a local scale. In order to apply large fields while measuring the piezoelectricity, nanosecond-scale time resolved diffraction techniques were used.

1.7.1. Sample fabrication

The epitaxial $BiFeO_3$ and $Pb(Zr,Ti)O_3$ (001) thin films for this study were grown in the research group of Prof. Chang-Beom Eom.[77] $BiFeO_3$ and $Pb(Zr,Ti)O_3$ layers were deposited using off-axis sputtering on a $SrTiO_3$ (001) substrate. The $Pb(Zr,Ti)O_3$ and 400 nm $BiFeO_3$ samples had an additional 15 nm thick $SrRuO_3$ layer between the substrate and the ferroelectric layers. $SrRuO_3$ is a conducting oxide which served as a bottom electrode and allowed us to create thin film capacitor structures. The $BiFeO_3$ samples were grown on a substrate that was miscut by 4° towards [010]. The miscut substrate helps promote epitaxial growth and select the polarization direction of the domains.[78]

Bulk $BiFeO_3$ samples were grown by Sang-Wook Cheong's research group at Rutgers University using the flux growth method. Single crystals of $BiFeO_3$ were grown using a $Bi_2O_3/Fe_2O_3/B_2O_3$ flux by cooling slowly from 870° to 620° C.[79] Platelets several millimeters across with faces parallel to the pseudocubic (001) were obtained. Multiple ferroelectric domains were observed with x-ray diffraction and with polarized light microscopy.

1.7.2. Ferroelectric characterization and polarization switching

Electric fields were applied to the sample in the out-of-plane direction by applying a voltage across platinum top electrodes and the $SrRuO_3$ layer underneath the $Pb(Zr,Ti)O_3$ or $BiFeO_3$ layers. Circular platinum top electrodes with diameters of 25, 50, 75, 100, and 200 μm were patterned on top of the $Pb(Zr,Ti)O_3$ and $BiFeO_3$ films.

Top electrodes were contacted with a high bandwidth 5μm tungsten probe tip (Cascade Microtech, 107-158). The $SrRuO_3$ bottom electrode was contacted by soldering a thin platinum wire to an area at the corner of the sample where the film had been removed to expose the $SrRuO_3$ bottom electrode. This wire was connected to the outer coaxial connection of the probe tip. This connection is usually grounded in high frequency experiments. In order to make hysteresis loops, however, we isolated the outer connection from ground and used it to connect the sample to the resistor we used to measure the displacement current flowing through the ferroelectric capacitor. Electric fields were applied to the region underneath the top electrode by applying a voltage across the film thickness using a function generator (Agilent 33120A).

Ferroelectric switching properties of the films were determined by measuring the electrical hysteresis loops of capacitor structures. Several periods of a triangle waveform with a amplitudes of 7 to 10 V were applied to the top electrode. A sample of the poling pulse train and the switching current is shown in Figure 1.5.

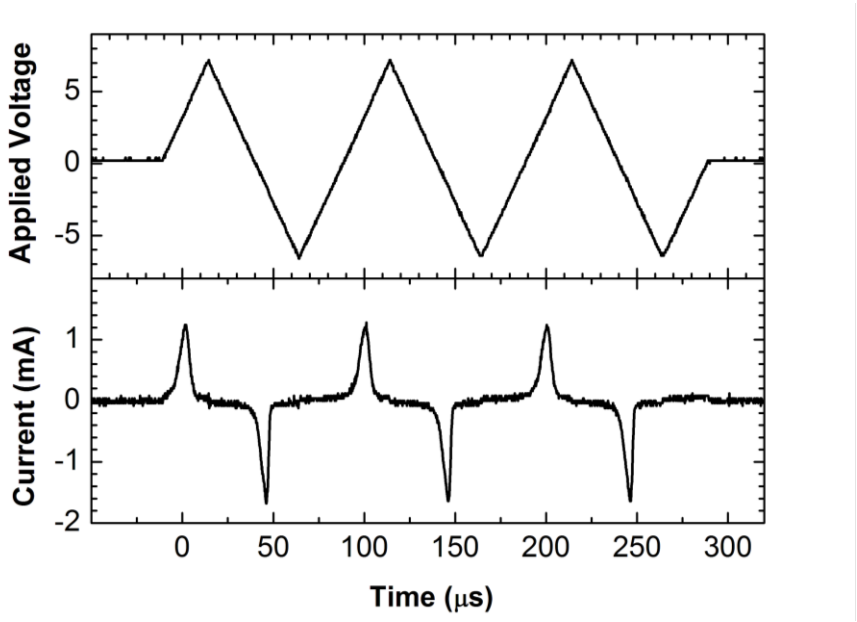

Figure 1.5. Voltage and switching current from a 100μm diameter $Pb(Zr,Ti)O_3$ capacitor measured during a poling pulse train resulting in a P_{up} state.

The current measurement shows that the capacitor is switching and does not have significant leakage current. The sharp current spikes are the switching current from the polarization reversing direction to align parallel to the electric field. In leaky devices, the capacitor develops conduction paths which behave like a resistor in parallel with the capacitor. At low frequencies, the current through a leaky device at is proportional to the applied field. This was not observed for the device shown in Figure 1.5.

To obtain a quantitative measurement of the coercive field, we calculated the polarization versus electric field to get a ferroelectric hysteresis loop. The polarization *P* is measured by integrating the displacement current over time, normalizing to the electrode area, and plotting charge per area as a function of the applied voltage. A hysteresis loop for a 100 μm-diameter $Pb(Zr,Ti)O_3$ capacitor in this sample is shown in Figure 1.6. The coercive fields were +350 kV/cm and -150 kV/cm. Note that the coercive fields are not the same for positive

and negative poling directions, causing the hysteresis loop to be shifted horizontally along the electric field axis. The apparent difference in coercive field is an effect of different materials in the top and bottom electrodes.[80] To avoid artifacts from charging effects, the polarization was measured by taking the difference in polarization when no bias is applied to the capacitor to get twice the remnant polarization, $2P_r$.

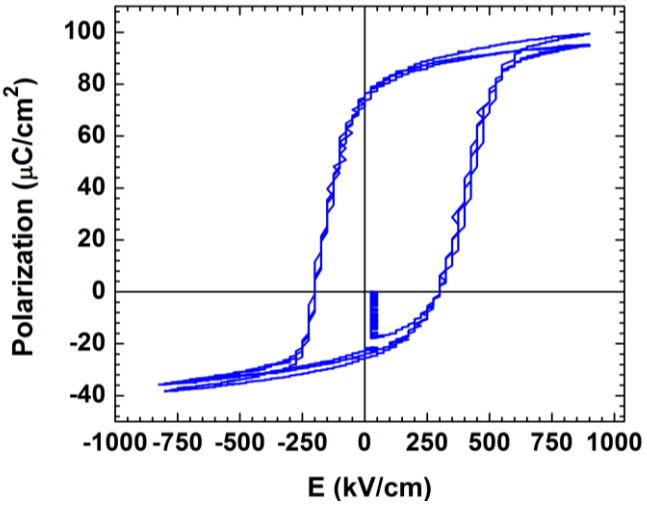

Figure 1.6. Hysteresis loop of 100 μm diameter $Pb(Zr,Ti)O_3$ capacitor at 10 kHz. The vertical line near the origin is an artifact of the noise in the voltage measurement across the resistor. The polarization plotted here is the integrated displacement current from Figure 1.5.

1.7.3. X-ray diffraction structural characterization

This study uses two different types of x-ray sources. A laboratory x-ray diffractometer was used to measure the area-averaged structure of the entire sample. The local structure of the film was probed using focused synchrotron radiation.

1.7.3.1. Area-averaged structure

Laboratory x-ray diffractometers were used to probe the area-averaged structure of $BiFeO_3$ bulk and thin film samples. The millimeter sized x-ray spots diffract from the entire sample, giving information about the average structure of the film. Two diffractometers were used based on a sealed tube source (Panalytical X'Pert MRD) and on a rotating anode (Rigaku UltraX 18 Rotaflex). A monochromatic beam with the Cu K_α wavelength, λ = 1.5406, is selected from the spectrum by diffracting from a crystal monochromator. The sample is mounted on a four-circle diffractometer in a horizontal scattering geometry. Three degrees of freedom are available to rotate the sample to the Bragg condition (θ, χ, and φ); the rotation in 2θ brings the detector to the diffracted beam (Figure 1.7). These naming conventions are used to describe the diffraction geometry through the rest of this thesis.

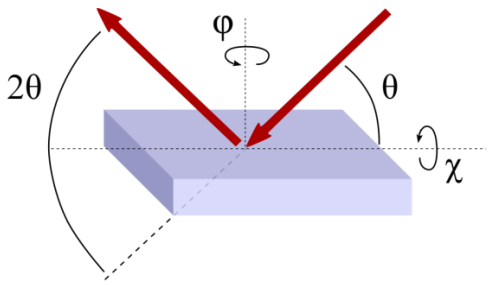

Figure 1.7. Scattering geometry angle definitions for four circle diffractometers.

The Panalytical diffractometer is designed to measure x-ray diffraction and reflectivity of thin epitaxial films. Two dimensional slices of reciprocal space were mapped out to determine the orientation of $BiFeO_3$ films with respect to the substrate, as described in Chapter 2. The 4-bounce Ge monochromator and large beam (1 mm × 10 mm at the source) produce the highly collimated beam that is necessary for high resolution measurements of thin films. Angular resolution in 2θ was set to 0.1° by the detector slits. The film reflections

were more than 0.5° wide in 2θ due to the mosaic spread, so higher angular resolution did not provide any additional information.

The Rigaku rotating anode diffractometer was used for measurements of low-intensity Bragg reflections. This diffractometer is optimized for low-intensity measurements from small samples. The rotation of the anode distributes the heat load more evenly so that higher intensities of x-rays can be produced. This generator was operated in point-focus mode, so the x-ray spot size at the sample (≈1 mm^2) was slightly smaller than for the Panalytical. Attenuation of the beam was reduced by removing the air inside flight paths between the source and sample as well as in front of the detector. The Na:I scintillation detector (Saint Gobain, Bicron 1XPM-040B) is capable of detecting single photons. A lead cap was placed on the end of the detector to absorb high energy photons. Angular resolution in 2θ was determined by slits placed in front of the detector.

1.7.3.2. Synchrotron x-ray microdiffraction

Synchrotron light sources provide the intensity required to measure small scattering signals with a focused x-ray beam. Synchrotron light is coherent and the flux is orders of magnitude higher than the laboratory x-ray sources.[81] These advantages allow for the use of x-ray focusing optics such as zone plates and mirrors. The x-rays are generated in 100 ps pulses spaced 153 ns apart, which is useful for time-resolved scattering.[82] A schematic of the entire setup is shown below in Figure 1.8 and each element is discussed below.

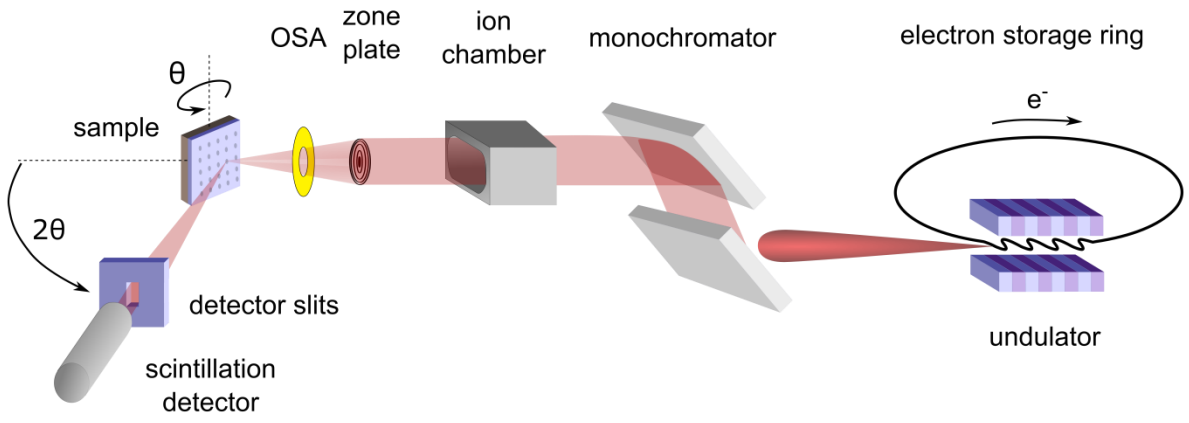

Figure 1.8. Schematic of synchrotron microdiffraction.

Synchrotrons generate x-rays by accelerating electrons in periodically curved path. The electrons pass through undulators – banks of magnets with alternating polarity – which bend the electron's path back and forth at a specific radius. At the photon energies used in these experiments, the emitted beam primarily consists of the desired wavelength λ, but a small component with wavelengths of higher orders 3λ and 5λ are also present.[83,84]

Monochromators were used to reduce the spectral bandwidth sufficiently to allow precise diffraction measurements. In the monochromator, the beam is diffracted from two (111)-oriented Si crystals which are positioned at the Bragg angles of the desired wavelength. Only photons with wavelengths that meet the Bragg condition can pass through the monochromator. The spectral width of the monochromatized beam is limited by the Darwin width of the Si (111) reflection, typically about 1 eV.[81]

The incident beam intensity is monitored using a gas ionization chamber placed after the monochromator in the experimental hutch. The beam passed through the air between two

charged plates. The resulting ionization current is proportional to the beam intensity, but decreases exponentially with increasing photon energy.[85]

For several measurements we focused the monochromatic beam using a Fresnel zone plate. Fresnel zone plates are essentially circular diffraction gratings, with alternating circles of materials with different indices of refraction.[86] The zone plates used in these experiments consist of patterns of concentric gold rings patterned on Si_3N_4 membranes. X-rays passing through the gold Fresnel zones undergo a phase shift. The pattern is designed such that the phase shifts introduced causes constructive interference at focal spot. The focal distance and spot size are determined by the zone plate diameter, photon energy, number of zones, and width of the outermost zone.[83] Zone plates are typically used at synchrotron light sources because coherent x-rays are required and there is a significant loss of intensity (only 10% of the transmitted beam is focused at the first order focal point.)[87]

In order to avoid contamination from the unfocused beam, all but the focused beam is blocked. The unfocused beam is absorbed in two parts – a central beamstop and a pinhole which acts as an order-sorting aperture. The beamstop is a gold sphere either integrally mounted on the zone plate or on a separate Si_3N_4 window. It blocks the direct beam through the center of the zone plate. The order sorting aperture is placed between the zone plate and the focal point in order to block the unfocused beam and any focused x-rays from higher order focal points.

The focused beam is measured by scanning a chromium knife edge across the focal point and measuring the Cr fluorescence. A knife-edge scan from the 160 μm-diameter zone plate at Sector 2-ID-D is shown in Figure 1.9.

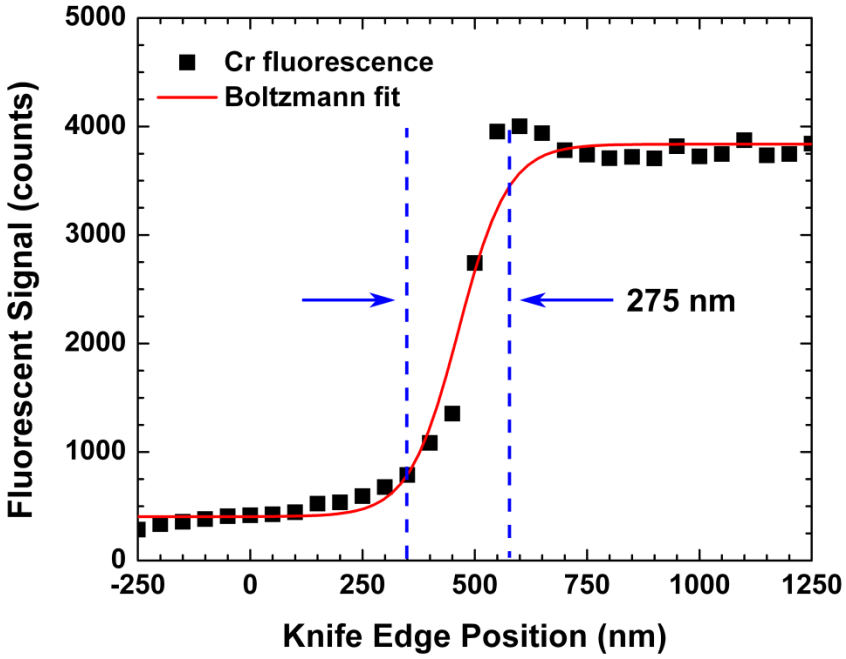

Figure 1.9. Chromium knife edge scan of focused x-ray beam. The sharpest part of the knife edge was scanned across the focal point of the x-ray beam and the fluorescence was measured.

The fluorescence signal was fit to a Boltzmann function. The beam size was estimated as being the width of the Boltzmann function. Typical values for beam size using a 320 μm diameter zone plate at sector 2-ID-D of the Advanced Photon Source are around 400 nm.

Three types of detectors were used to measure the diffracted x-ray beam. Avalanche photodiodes (APD) have a fast response time. These detectors are useful for high count rates up to 10^6 photons per second. An APD was used for nanosecond-scale time-resolved diffraction experiments. A charge-coupled device (CCD) area detector records the diffracted intensity from a large portion of reciprocal space at once. It was used to locate the $BiFeO_3$ (103) reflections and measure the splitting between the (103) reflections from multiple

domains. A scintillation detector (Saint-Gobain, Bicron) was used for low count rates, because it was capable of counting single photons and could filter out higher energy photons to some degree.

1.7.4. Time-resolved microdiffraction

Time-resolved diffraction was used to measure the structural response to electric field of $BiFeO_3$ films. Two time resolution techniques were used. The slower, millisecond-scale method employed a multichannel analyzer to obtain the time-resolved signal. The faster, nanosecond-scale method was a pump-probe type experiment in which only x-ray pulses synchronized with electrical pulses were counted. The millisecond-scale method had longer counting times and was able to measure the responses of very weak reflections. The nanosecond-scale method applied the electric field for very short times, enabling devices to sustain very high electric fields without undergoing dielectric breakdown.

1.7.4.1. Time-resolved microdiffraction – millisecond time scale

Millisecond-scale time resolved diffraction was used to measure the piezoelectric response of $BiFeO_3$ and the changes in the intensity of the ½(*hkl*) reflections. The time resolved intensity of a reflection was measured while an electric field was applied to a capacitor on the sample. Thus, the structural response to an electric field was determined. There were three challenges here – time resolved diffraction, focusing the beam inside a capacitor, and synchronizing the electric field with the time resolved measurements.

The microdiffraction techniques discussed above were used to focus the x-ray beam to a small spot on the sample. Changes in the diffracted intensity and/or the fluorescence from

the platinum electrodes were used to determine the position of the x-ray beam on the sample surface. By mapping areas on the surface, it was possible to image the electrode pattern and place a focused beam on the same top electrode as the electrical probe tip. This ensured that the diffraction volume was entirely within the capacitor and only regions subjected to electric field were probed.

A multichannel analyzer (MCA) was used to record the diffracted intensity as a function of time. The MCA measured the counts from the detector over a 2 second period in 2 ms steps. Any counts which were detected during each 2 ms bin were summed together. The MCA output the time resolved intensity in the form of total counts in each of the 2000 bins. Thus, the time resolution was determined by the MCA counting time per bin. This counting time could be set as low as 8μs, but short counting times proved to be impractical for low-intensity reflections.

We applied an electric field and simultaneously measured the time-dependent intensity. A function generator (Agilent 33120A) was configured to produce linearly varying voltages similar to the triangle pulses in Figure 1.5. The output of the function generator was connected to the electrical probe tip contacting the capacitor top electrode. The bottom electrode was grounded. The function generator was triggered at the same time as the MCA, so the intensity was measured while a series of triangle pulses was applied to the capacitor. By matching the time dependence of the voltage with that of the intensity, we obtained the diffracted intensity as a function of electric field. We summed over thousands of repetitions in order to obtain the time-dependent intensity at each point in reciprocal space.

1.7.4.2. Time resolved microdiffraction – nanosecond time scale

Nanosecond-scale time resolved diffraction was used to measure the piezoelectric strain in $BiFeO_3$ at electric fields above the DC dielectric breakdown limit. Previous studies have found that ferroelectrics subjected to large electric fields do not undergo dielectric breakdown if the pulses have short durations (tens of nanoseconds).[88] Short pulse durations also reduce the amount of resistive heating from leakage current which helps increase device longevity. By measuring the diffracted intensity from single bunches synchronized with short pulses, we were able to measure the piezoelectric strain at large electric fields.

Short voltage pulses were applied to capacitors at the same time as x-ray bunches diffracted from the sample. The electric field was applied to capacitors by a pulse generator (Picosecond Pulse Labs, 2600C). Top electrodes were contacted by the electrical probe tip. A thin platinum wire connected the $SrRuO_3$ bottom electrode to the shielding of the probe tip. Square voltage pulses were applied to the top electrode by a pulse generator with adjustable amplitudes and durations. Typical pulse durations were 15 to 30 ns, with rise times below 300 ps. The pulse generator was triggered by a signal from the timing circuit described below.

The diffracted signal from one x-ray bunch was synchronized with the electric field. An APD detector was chosen to detect the diffracted x-rays because its response is short than the time between x-ray bunches. We selected the APD signal from a single bunch which coincided with the applied voltage pulse. The detector gating and pulse generator triggering electronics required to do this are described in Grigoriev *et al.*[89] The time between the

selected x-ray bunch and voltage pulses was adjusted by delaying the trigger signals for the pulse generator and APD gate with delay generators (Stanford Research Systems, DG535). The experiment is shown schematically in Figure 1.10.

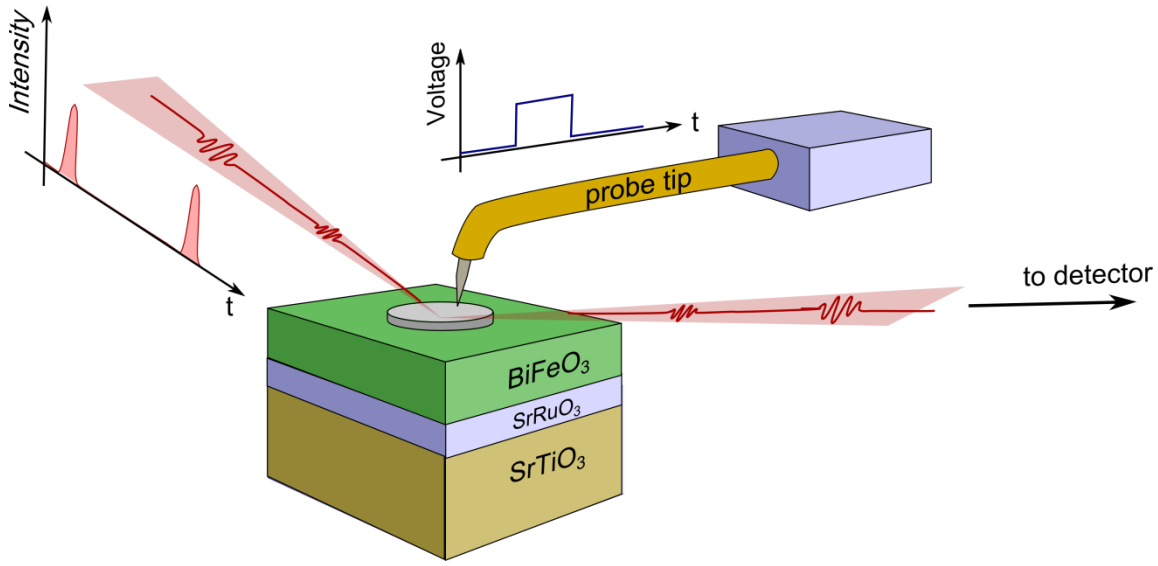

Figure 1.10. Schematic diagram of time resolved microdiffraction. The focused x-ray beam probes the region of $BiFeO_3$ underneath a top electrode contacted by the probe tip while an electric field is applied.

The synchronization was tested by measuring the time-dependent intensity at the peak of a Bragg reflection. When an electric field was applied, the film was piezoelectrically strained which modified the lattice constants. A decrease in diffracted intensity at the peak of a reflection indicated that the voltage pulse was applied at the same time as the selected x-ray bunch. The only x-rays that were counted had diffracted from the sample when the electric field was being applied.

Many voltage pulses/x-ray bunches pairs had to be measured at each point in reciprocal space. The APD could only measure one count per pulse, so a typical θ-2θ scan

would require thousands of pulses at each point in order to distinguish the Bragg reflection from the background. Typically thousands of pulses were applied at each point in a scan in order to improve counting statistics.

1.8. Summary

As $BiFeO_3$ films relax, the epitaxial strain is relieved and the film approaches the bulk structure. The magnetic properties are strongly influenced by the Fe-O-Fe bond angle, which changes as a function of rotation of the oxygen octahedra. The octahedral rotation angle is affected by the epitaxial strain and piezoelectric expansion. In order to understand the coupling between electrical and magnetic order parameters in $BiFeO_3$, we first have to understand the relationship between substrate, structure, and electric field. In the following chapters, I describe how the x-ray diffraction techniques outlined above were used to determine that the strain state, piezoelectric response, and cation displacements vary on the micron scale in $BiFeO_3$ thin films.

1.9. Chapter 1 references

[1] H. Schmid, "*Multiferroic Magnetoelectrics*," Ferroelectrics **162**, 317 (1994).

[2] H. Schmid, *"Some symmetry aspects of ferroics and single phase multiferroics,"* J. Phys.: Condens. Matter **20**, 434201 (2008).

[3] N. A. Spaldin and M. Fiebig, *"The Renaissance of Magnetoelectric Multiferroics,"* Science **309,** 391 (2005).

[4] B. G. Park, J. Wunderlich, X. Marti, V. Holy, Y. Kurosaki, M. Yamada, H. Yamamoto, A. Nishide, J. Hayakawa, H. Takahashi, A. B. Shick, and T. Jungwirth, *"A spin-valve-like magnetoresistance of an antiferromagnet-based tunnel junction,"* Nature Mater. **10,** 347 (2011).

[5] M. Bibes and A. Barthélémy, *"Multiferroics: Towards a magnetoelectric memory,"* Nature Materials **7**, 425 (2008).

[6] H. Bea, M. Bibes, M. Sirena, G. Herranz, K. Bouzehouane, E. Jacquet, S. Fusil, P. Paruch, M. Dawber, J. P. Contour, and A. Barthelemy, *"Combining half-metals and multiferroics into epitaxial heterostructures for spintronics,"* Appl. Phys. Lett. **88**, 062502 (2006).

[7] Y. -H. Chu, M. P. Cruz, C. -H. Yang, L. W. Martin, P .-L. Yang, J. -X. Zhang, K. Lee, P. Yu, L. -Q. Chen, and R. Ramesh, "*Domain control in multiferroic $BiFeO_3$ through substrate vicinality,"* Adv. Mater. **19,** 2662 (2007).

[8] H. W. Jang, D. Ortiz, S. H. Baek, C. M. Folkman, R. R. Das, P. Shafer, Y. Chen, C. T. Nelson, X. Pan, R. Ramesh, and C. B. Eom, "*Domain engineering for enhanced ferroelectric properties of epitaxial (001) $BiFeO_3$ thin films*," Adv. Mater. **21**, 817 (2009).

[9] Y. Tokura (ed.), *Colossal Magnetorestive Oxides*, (Gordon and Breach Science Publishers, Amsterdam, Netherlands, 2000).

[10] M. Bibes and A. Barthelemy, *"Multiferroics: Towards a magnetoelectric memory,"* Nature Mater. **7**, 425 (2008).

[11] H. Bea, M. Gajek, M. Bibes, and A. Barthelemy, "*Spintronics with multiferroics,"* J. Phys.: Cond. Mat. **20**, 434231 (2008).

[12] D. Lebeugle, D. Colson, A. Forget, M. Viret, A. M. Battaille, and A. Gukasov, "*Electric-Field-Induced Spin Flop in $BiFeO_3$ Single Crystals at Room Temperature*", Phys. Rev. Lett. **100,** 227608 (2008).

[13] P. Fischer, M. Polomska, I. Sosnowska, and M. Szymanski, "*Temperature-dependence of the crystal and magnetic structures of $BiFeO_3$*," J. Phys. C **13**, 1931 (1980).

[14] J. R. Teague, R. Gerson, W. J. James, *"Dielectric hysteresis in single crystal $BiFeO_3$"* Solid State Commun. **8**,1073 (1970).

[15] T. Zhao, A. Scholl, F. Zavaliche, K. Lee, M. Barry, A. Doran, M. P. Cruz, Y. H. Chu, C. Ederer, N. A. Spaldin, R. R. Das, D. M. Kim, S. H. Baek, C. B. Eom, and R. Ramesh, "*Electrical control of antiferromagnetic domains in multiferroic $BiFeO_3$ films at room temperature*," Nature Mater. **5**, 823 (2006).

[16] J. H. Lee, K. M. Rabe, "*Coupled magnetic-ferroelectric metal-insulator transitions in epitaxially-strained $SrCoO_3$ from first principles,*" arXiv:1104.2856v1

[17] M. E. Lines and A. M. Glass, *Principles and Applications of Ferroelectric and Related Materials,* (Oxford University Press, New York, 2001).

[18] M. Dawber, K. M. Rabe, and J. F. Scott, "*Physics of Thin Film Ferroelectric Oxides*", Rev. Mod. Phys. **77,** 1083 (2005).

[19] J. F. Scott, "*Ferroelectrics go bananas*," J. Phys. Cond. Matter **20**, 021001 (2000).

[20] G. R. Fox, R. Bailey, W. B. Kraus, F. Chu, S. Sun, and T. Davenport, *"The current status of FeRAM,"* in Ferroelectric Random Access Memories: Fundamentals and Applications (Springer-Verlag, 2004).

[21] H. Kohlstedt, Y. Mustafa, A. Gerber, A. Petraru, M. Fitsilis, R. Meyer, U. Bottger, and R. Waser, "*Current status and challenges of ferroelectric memory devices*", Microelectronic Engineering **80**, 296 (2005).

[22] A. A. Vives, *Piezoelectric Transducers and Applications*, (Springer, 2008).

[23] A. York, *"Experimental characterization and modeling of electro-mechanically coupled ferroelectric actuators."* PhD Thesis (2008).

[24] R. L. Smith, *The Electrical Engineering Handbook,* edited by R. C. Dorf, (CRC Press, 1997). Chapter 56.

[25] J. F. Nye, *Physical Properties of Crystals*, (Oxford University Press, 1985).

[26] D.-H. Do, P. G. Evans, E. D. Isaacs, D. M. Kim, C.-B. Eom and E. M. Dufresne, *"Structural visualization of polarization fatigue in epitaxial ferroelectric oxide devices,"* Nature Mater. **3**, 365 (2004).

[27] M. J. Hytch, E. Snoeck, R. Kilaas, "Quantitative measurement of displacement and strain fields from HREM micrographs," Ultramicroscopy **74,** 131 (1998).

[28] G. B. Stevenson and K. R. Elder, *"Theory for equilibrium 180 degrees stripe domains in $PbTiO_3$ films,"* J. Appl. Phys. **100**, 051601 (2006).

[29] S. K. Streiffer and C. B. Parker, "*Domain patterns in epitaxial rhombohedral ferroelectric films. I. Geometry and experiments"* J. Appl. Phys. **83**, 2744 (1998).

[30] V. Sundar and R. E. Newnham, *The Electrical Engineering Handbook,* edited by R. C. Dorf, (CRC Press, 1997). Chapter 50.

[31] S. W. Cheong and M. Mostovoy, "*Multiferroics: a magnetic twist for ferroelectricity*," Nature Mater. **6**, 13 (2007).

[32] J F Scott and R Blinc, "*Multiferroic magnetoelectric fluorides: Why are there so many magnetic ferroelectrics?"* J. Phys.: Condens. Matter **23**, 113202 (2011).

[33] N. A. Hill, "*Why are there so few magnetic ferroelectrics"*, J. Phys. Chem. B **104**, 6694 (2000).

[34] J. B. Neaton, C. Ederer, U. V. Waghmare, N. A. Spaldin, and K. M. Rabe *"First-principles study of spontaneous polarization in multiferroic $BiFeO_3$,"* Phys. Rev. B **71**, 014113 (2005).

[35] C. Li, K. Chi, K. Soh, and P. Wu, *"Formability of ABO_3 perovskites,"* Journal of Alloys and Compounds **372**, 40 (2004).

[36] L. Liu, *"Silicate Perovskites: A Review,"* Surveys in Geophysics **10**, 63 (1989).

[37] H. D. Megaw and C. Darlington, "*Geometrical and Structural Relations in the Rhombohedral Perovskites*", Acta Cryst. A **31,** 161 (1975).

[38] M. Johnsson and P. Lemmens, "*Crystallography and Chemistry of Perovskites*" in *Handbook of Magnetism and Advanced Magnetic Media*, (ed. H. Kronmüller), (John Wiley & Sons, New York, 2006).

[39] V.M. Goldschmidt, Skrifer Norske Videnskaps-Akad. Oslo, I.Mat.-Nat. Kl. **8** (1926).

[40] C. Li, K. C. K. Soh, P. Wu, "*Formability of ABO_3 Perovskites*," Journal of Alloys and Compounds **372,** 40 (2004).

[41] A. M. Glazer, "*The Classification of Tilted Octahedra in Perovskites,"* Acta Cryst. B **28,** 3384 (1972).

[42] P.M. Woodward, "*Octahedral Tilting in Perovskites. I. Geometrical Considerations*" Acta Cryst. B **53**, 32 (1997).

[43] P.M. Woodward, *"Octahedral Tilting in Perovskites 2. Structure Stabilizing Forces,"* Acta Cryst. B **53**, 44 (1997).

[44] C. Michel, J. M. Moreau, G. D. Achenbach, R. Gerson, R. and J. W. James, Solid State Commun. *"Atomic Structure of $BiFeO_3$,"* **7**, 701 (1969).

[45] S. V. Kiselev, R. P. Ozerov and S. G. Zhdanov, Sou. Phys.-Dokl. **7**, 742 (1963).

[46] C. Blaauw and F. Vanderwoude, "*Magnetic and Structural Properties of $BiFeO_3$*", Journal of Physics C – Solid State Physics **6,** 1422 (1973).

[47] I. Sosnowska, T. Peterlin-Neumaier and E. Steichele, "*Spiral magnetic ordering in bismuth ferrite*," J. Phys. C: Solid State Phys. **15,** 4835 (1982).

[48] S. Lee, T. Choi, W. Ratcliff, R. Erwin, S. W. Cheong, and V. Kiryukhin, "*Single ferroelectric and chiral magnetic domain of single-crystalline $BiFeO_3$ in an electric field,*" Phys. Rev. B **78**, 100101 (2008).

[49] R. Przenioslo, M. Regulski, I. Sosnowska, "*Modulation in multiferroic $BiFeO_3$: Cycloidal, elliptical or SDW?,*" J. Phys. Soc. Japan **75**, 084718 (2006).

[50] J. B. Goodenough, *"Theory of the role of covalence in the perovskite-type manganites [La,M(II)]MnO_3,"* Phys. Rev. **100**, 564 (1955).

[51] C. E. Ederer and N. A. Spaldin, *"Weak ferromagnetism and magnetoelectric coupling in bismuth ferrite,"* Phys. Rev. B **71**, 060401 (2005).

[52] S. Picozzi and C. Ederer, *"First principles studies of multiferroic materials,"* J. Phys. Condens. Matter **21,** 303201 (2009)

[53] H. Schmid, *"On a magnetoelectric classification of materials," Int. J. Magn.* **4,** 337 (1973).

[54] A. Reyes, C. de la Vega, Ma.E. Fuentes and L. Fuentes, *"$BiFeO_3$: Synchrotron radiation structure refinement and magnetoelectric geometry,"* Journal of the European Ceramic Society **27,** 3709 (2007).

[55] C. Tabares-Muñoz, J. –P. Rivera, A. Bezinge, A. Monnier, and H. Schmid, "*Measurement of the Quadratic Magnetoelectric Effect on Single Crystalline $BiFeO_3$* " Jpn. J. Appl. Phys. **24**, 1051 (1985).

[56] J. Wang, J. B. Neaton, H. Zheng, V. Nagarajan, S. B. Ogale, B. Liu, D. Viehland, V. Vaithyanathan, D. G. Schlom, U. V. Waghmare, N. A. Spaldin, K. M. Rabe, M. Wuttig, and R. Ramesh, "*Epitaxial $BiFeO_3$ multiferroic thin film heterostructures"*, Science **299**, 1719 (2003).

[57] Yu.F. Popov, A.M. Kadomtseva and S.S. Krotov *et al.*, "*Features of the magnetoelectric properties of $BiFeO_3$ in high magnetic fields,"* Low Temp. Phys. **27,** 478 (2001).

[58] A.K. Zvezdin, A.M. Kadomtseva and S.S. Krotov, "*Magnetoelectric interaction and magnetic field control of electric polarization in multiferroics*," J. Magn. Magn. Mater. **300,** 224 (2006).

[59] H. Bea, M. Bibes, X. H. Zhu, S. Fusil, K. Bouzehouane, S. Petit, J. Kreisel, and A. Barthelemy, "*Crystallographic, magnetic, and ferroelectric structures of bulklike $BiFeO_3$ thin films,"* Appl. Phys. Lett. **93**, 072901 (2008).

[60] C. Ederer and N. A. Spaldin, "*Influence of strain and oxygen vacancies on the magnetoelectric properties of multiferroic bismuth ferrite*", Phys. Rev. B **71**, 224103 (2005).

[61] H. W. Jang, S. H. Baek, D. Ortiz, C. M. Folkman, R. R. Das, Y. H. Chu, P. Shafer, J. X. Zhang, S. Choudhury, V. Vaithyanathan, Y. B. Chen, D. A. Felker, M. D. Biegalski, M. S. Rzchowski, X. Q. Pan, D. G. Schlom, L. Q. Chen, R. Ramesh, and C. B. Eom, *"Strain-Induced Polarization Rotation in Epitaxial (001) $BiFeO_3$ Thin Films,"* Phys. Rev. Lett. **101**, 107602 (2008).

[62] D. H. Kim, H.N. Lee, M. D. Biegalski, and H. M. Christen, "*Effect of epitaxial strain on ferroelectric polarization in multiferroic $BiFeO_3$ films*", Adv. Phys. Lett. **92,** 012911 (2008).

[63] J. Li, J. Wang, M. Wuttig, R. Ramesh, N. Wang, B. Ruette, A. P. Pyatoakov, A. K. Zvezdin, and D. Viehland, "*Dramatically enhanced polarization in (001), (101), and (111) $BiFeO_3$ thin films due to epitiaxial-induced transitions*", Appl. Phys. Lett. **84,** 5261 (2004).

[64] J. F. Scott, "*Multiferroic Memories*," Nature Mater. **6**, 256 (2007).

[65] J. W. Matthews and A. E. Blakeslee, "*Defects in Epitaxial Multilayers,"* J. Cryst. Growth **27,** 118 (1974).

[66] H. Béa, M. Bibes, M. Sirena, G. Herranz, K. Bouzehouane, E. Jacquet, S. Fusil., P. Paruch, M. Dawber, J.-P. Contour, and A. Barthélémy, "*Combining half-metals and multiferroics into epitaxial heterostructures for spintronics*," Appl. Phys. Lett. **88**, 062502 (2006).

[67] J. Simon, Th. Walther, W. Mader, et al., *"Diffusion and segregation effects in doped manganite/titanate heterostructures,"* Appl. Phys. Lett. **84**, 3882 (2004).

[68] M.S. Kartavtseva, O. Yu. Gorbenko, A.R. Kaul, T.V. Murzina, "*The influence of epitaxial strain on magnetic and electrical properties of $BiFeO_3$ thin films*", Thin Solid Films **518**, 4750 (2010).

[69] M. B. Holcomb, L. W. Martin, A. Scholl, Q. He, P. Yu, C.-H. Yang, S. Y. Yang, P.-A. Glans, M. Valvidares,M. Huijben, J. B. Kortright, J. Guo, Y.-H. Chu, and R. Ramesh, "*Probing the evolution of* antiferromagnetism in multiferroics", Phys. Rev. B 81, 134406 (2010).

[70] D. T. Cromer and B. Mann, *"X-Ray Scattering Factors Computed From Numerical Hartree-Fock Wave Functions*," Acta Cryst. A **24,** 321, (1968).

[71] D. Waasmaeir and A. Kirfel, *"New Analytical Scattering Factor Functions for Free Atoms and Ions for Free Atoms and Ions,"* Acta. Crys. A **51,** 416 (1995).

[72] B.L. Henke, E.M. Gullikson, and J.C. Davis, *"`X-ray Interactions: Photoabsorption, Scattering, Transmission, and Reflection at E=50-30,000 eV, Z=1-92,"* Atomic Data and Nuclear Data Tables **54,** 181 (1993).

[73] B.E. Warren, *X-ray Diffraction*, (Dover Publications, New York, 1990).

[74] J. Als-Nielsen and D. McMorrow, *Elements of Modern X-ray Physics*, (John Wiley & Sons, West Sussex, England, 2001).

[75] A. Guinier, *X-ray Diffraction In Crystals, Imperfect Crystals, and Amorphous Bodies*, (W.H. Freeman and Co., 1963).

[76] B. D. Cullity and S. R. Stock, *Elements of X-ray Diffraction (3rd edition),* (Prentice Hall, 2001).

[77] R. R. Das, D. M. Kim, S. H. Baek,, C. B. Eom, F. Zavaliche, S. Y. Yang, R. Ramesh, Y. B. Chen, X. Q. Pan, X. Ke, M. S. Rzchowski, and S. K. Streiffer, "*Synthesis and ferroelectric properties of epitaxial $BiFeO_3$ thin films grown by sputtering*," Appl. Phys. Lett. **88**, 242904 (2008).

[78] Y. -H. Chu, M. P. Cruz, C. -H. Yang, L. W. Martin, P .-L. Yang, J. -X. Zhang, K. Lee, P. Yu, L. -Q. Chen, and R. Ramesh, "*Domain control in multiferroic $BiFeO_3$ through substrate viscinality*," Adv. Mater. **19,** 2662 (2007).

[79] T. Choi, S. Lee, Y. J. Choi, V. Kirukhin, S.-W. Cheong, *"Switchable Ferroelectric Diode and Photovoltaic Effect in $BiFeO_3$*," Science **324**, 63 (2009).

[80] K. M. Rabe, C. H. Ahn, and J. M. Triscone, *Physics of Ferroelectrics*, (Springer-Verlag, Berlin, 2007). Chapter 1.

[81] J. Als-Nielsen and D. McMorrow, *Elements of Modern X-ray Physics*, (John Wiley & Sons, West Sussex, England, 2001).

[82] Advanced Photon Source operating parameters, http://www.aps.anl.gov/Facility/Storage_Ring_Parameters/node5.html, downloaded 7/22/2011.

[83] D. Attwood, *Soft X-rays and Extreme Ultraviolet Radiation: Principles and Applications* (Cambridge University Press, 1999).

[84] K. J. Kim, *X-ray Data Booklet*, (Lawrence Berkeley National Lab, 2009), Section 2.1B

[85] A. C. Thompson, *X-ray Data Booklet*, (Lawrence Berkeley National Lab, 2009), Section 4.5

[86] K. Miyamoto, *"The Phase Fresnel Lens,"* J. Opt. Soc. Am. **51,** 17 (1961).

[87] A. I. Erko, V. V. Aristov, and B. Vidal, *Diffraction X-ray Optics*, (Institute of Physics Publishing, 1996). Chapter 2.

[88] A. Grigoriev, R. Sichel, H.-N. Lee, E. C. Landahl, B. Adams, E. M. Dufresne, and P. G. Evans, *"Nonlinear Piezoelectricity in Epitaxial Ferroelectrics at High Electric Fields,"* Phys. Rev. Lett. **100**, 027604 (2008).

[89] A. Grigoriev, D.-H. Do, P. G. Evans, B. W. Adams, E. Landahl, and E. M. Dufresne, *"Synchronizing fast electrically driven phenomena with synchrotron x-ray probes,"* Rev. Sci. Instrum. **78**, 023105 (2007).

Chapter 2. Anisotropic Relaxation of Epitaxial (001) $BiFeO_3$ Thin Films

2.1. Introduction

The piezoelectricity, ferroelectric domain structure, and multiferroic properties of thin film $BiFeO_3$ are influenced by aspects of the structure at length scales ranging from single-unit cell to the mesoscopic scale of mosaic blocks. In (001) thin films, $BiFeO_3$ is distorted by epitaxial strain and signatures of monoclinic,[1,2] tetragonal,[3,4] or even coexisting rhombohedral and tetragonal[5] overall symmetries have been reported. For coherent thin films without misfit dislocations, the consensus is that $BiFeO_3$ is strained into a monoclinic state for moderate compressive strains up to 3-4%.[2,6,7,8] At compressive strains above 4.5%, $BiFeO_3$ exhibits coexisting phases.[5] The structure of partially relaxed films is more complicated problem which has not yet been completely solved.

An additional difficulty in determining the structure is that epitaxial thin films of $BiFeO_3$ are often deposited on miscut substrates to assist the epitaxial growth process. A substrate which is miscut by several degrees promotes epitaxial growth by providing a high density of step edges at the surface. Step edges are lower-energy nucleation sites and assist in stabilizing the step-flow growth mode.[9,10] Furthermore, the magnitude and crystallographic direction of the substrate miscut influence the polarization direction in the $BiFeO_3$ layers.[11] The large density of steps and kinks on the surface also appears to help retention of the

volatile Bi species in the film and maintain the desired stoichiometry.[12] However, the vicinal surface can affect the film symmetry in unexpected ways. Miscut substrates stretch or compress the film along the plane defined by the average surface of the substrate. When the atomic planes are not parallel to the surface, different stresses are projected onto the in-plane crystallographic directions of the film. This anisotropic stress changes the structure.

The ferroelectric domain structure present in the film influences the electrical, ferroelectric, and multiferroic properties. In $BiFeO_3$ the conductivity of a (001) film depends on the domain pattern and type of domain wall.[13] The dynamics of ferroelectric switching is affected by defects at the junctions between different types of domain walls.[14] The domain structure also changes the exchange bias with neighboring ferromagnetic layers and affects the piezoelectric properties.[15,16] Understanding how the substrate affects the domain pattern is an important step towards tailoring the properties of $BiFeO_3$ films.

We have used x-ray diffraction to study the effects of the miscut of the substrate on the ferroelectric domain structure, the relaxation of the thin film via dislocations and other defects, and on the anisotropic stress imposed on the film. Diffraction patterns acquired with a large x-ray spot provide information that is averaged over the entire area of the film. These large-spot-size diffraction patterns demonstrate that the crystallographic axes of the film with respect to the substrate that cause anisotropy in the atomic-scale processes that lead to relaxation. Synchrotron x-ray microdiffraction with a focused x-ray beam was used to probe the structure on the scale of individual mosaic blocks, revealing that there are multiple ferroelectric domains within each mosaic block. The diffraction patterns of off-specular reflections from individual mosaic blocks are consistent with relaxed stripe domains,

following a ferroelectric domain structure previously observed in other ferroelectric thin films.

2.2. Experimental methods

The samples used in this study were (001) $BiFeO_3$ epitaxial thin films deposited using off-axis radio frequency sputtering.[11,12] The sample consisted of a 400 nm $BiFeO_3$ film on a 15 nm $SrRuO_3$ ($SrRuO_3$) layer deposited on a miscut (001) $SrTiO_3$ substrate. The substrate was miscut so the sample surface normal was rotated towards the [010] direction by approximately 3° from the [001].

The area-averaged structure of the $BiFeO_3$ layers was analyzed using x-ray diffraction (X'Pert Panalytical MRD). This diffractometer uses a beam with a cross-section extending 1 mm in the horizontal diffraction and 10 mm in height, larger than the approximately 5 mm lateral size of the sample. This instrument used the characteristic radiation from a copper target with an x-ray energy of 8.05 keV. The diffracted beam thus provides information about the structure of the entire $BiFeO_3$ layer.

Structure on the local scale can be very different from the macroscopic average. By focusing an x-ray beam, diffraction can be used to probe the micron-scale structure of the layer. Synchrotron x-ray microdiffraction studies were conducted at station 2-ID-D of the Advanced Photon Source. An 11.5 keV x-ray beam was focused to a 275 nm spot by a Fresnel zone plate as described in Section 1.7.4. The sample was mounted on the diffractometer so that the [010] direction of the $SrTiO_3$ substrate was perpendicular to the

scattering plane. Diffracted photons were collected by either an avalanche photodiode detector (APD) or a charge-coupled device (CCD) area detector.

Reciprocal space maps were acquired by rotating the sample to vary the incident angle of the x-ray beam, while the CCD detector was held at a fixed position. The angular position of each pixel in the CCD was calibrated by measuring the position of the direct beam on the CCD at several positions of the detector arm. The detector arm was then moved to 2θ of the Bragg condition and the incident angle was scanned in discrete steps. A CCD image was captured at each incident angle. The reciprocal space vector of each pixel in the series of images was calculated from three angles as in Section 1.5; 2θ and χ were determined by the pixel position, θ by the incident angle. Two-dimensional maps were created by summing the intensity of all pixels at the same 2θ and calculating only $\boldsymbol{q_x}$ and $\boldsymbol{q_z}$.

2.3. Film rotation caused by substrate miscut

Miscut substrates apply anisotropic stresses to epitaxial films. The effects of these stresses on the area-averaged $BiFeO_3$ lattice constants, relaxation processes, and the orientation of the atomic planes were studied in a laboratory x-ray diffraction experiment. The (002) reflection from the $BiFeO_3$ thin film was used to determine the *c*-axis lattice constants and orientation of the $BiFeO_3$. A similar set of planes indexed as (220) were used to analyze the $SrRuO_3$ layer. By comparing the orientations of the $BiFeO_3$ and $SrRuO_3$ to that of the substrate, we observe that both films are rotated. These rotations were in opposite directions and were caused by two different relaxation mechanisms.

2.3.1. Measurement of film rotation: direction and magnitude

Geometric relationships between the atomic planes of a film and substrate can be inferred from the crystallographic orientations. In pseudomorphic (001) oriented films, $\boldsymbol{a}$ and $\boldsymbol{b}$ are identical to those of the substrate. This requires the (00*l*) reciprocal lattice vectors of film and substrate to be parallel: $\boldsymbol{g}_{00l} = l\,(\boldsymbol{a}\times\boldsymbol{b}) / V$. [17] Differences in the unit cell volumes V_{film} and $V_{substrate}$ can change the magnitude but not the direction of $\boldsymbol{g}_{00l}$. Since reciprocal lattice vectors are perpendicular to the planes they represent, the (00*l*) planes of a pseudomorphic (001) film and substrate are expected to be parallel.

Our initial x-ray diffraction experiments showed that the (00*l*) atomic planes in the $BiFeO_3$ thin film were not parallel to the planes of the $SrTiO_3$ substrate. In order to investigate further, x-ray diffraction patterns of the (002) reflections were taken to determine the orientation of the $BiFeO_3$. Our first indication that the $BiFeO_3$ was rotated with respect to the substrate was that the maxima for the $BiFeO_3$ pseudocubic (002) reflection and the $SrTiO_3$ (002) reflection could not be obtained in a single θ-2θ scan. Instead, these reflections were observed with a small difference between the incident and Bragg angles. We defined the offset angle to be the difference between the incident angle θ, measured with respect to the sample surface, and the Bragg angle 2θ, such that $offset = \theta - \frac{1}{2}(2\theta)$. Our observation that the substrate and film could not be observed in the same θ-2θ scan indicated that the $SrTiO_3$ and $BiFeO_3$ had different offset angles and that their (002) planes were thus not parallel.

The key in defining the orientation of the $BiFeO_3$ thin film was to identify an unambiguous reference for the angular positions of x-ray reflections. We determined the

orientation of $SrTiO_3$ (002) planes and characterized the miscut to provide this orientation reference. We measured the incident angle of the $SrTiO_3$ (002) maximum from θ scans as a function of azimuthal angle ϕ to determine the direction and magnitude of the substrate miscut, as shown in Figure 2.1. We called the azimuthal angle ϕ to be consistent with the names of the angles on x-ray diffractometers. The sample was placed so that two edges of the square substrate were horizontal when $\phi = 0°$ because the edges are nearly parallel to the $SrTiO_3$ <100> directions. The offset at the $SrTiO_3$ (002) maximum is the projection of the miscut angle in the scattering plane. As ϕ was scanned, the projection of the miscut angle varied sinusoidally. A sine function was fit to the observed offset dependence on ϕ to determine the magnitude and direction of the miscut. The amplitude gives a miscut angle of 3.1° and the miscut direction is nearly parallel to the [010] direction of the $SrTiO_3$, such that the surface normal of the substrate is rotated away from the [001] towards the [010]. The magnitude and direction of the substrate miscut was established as a reference point for measuring the $BiFeO_3$ rotation.

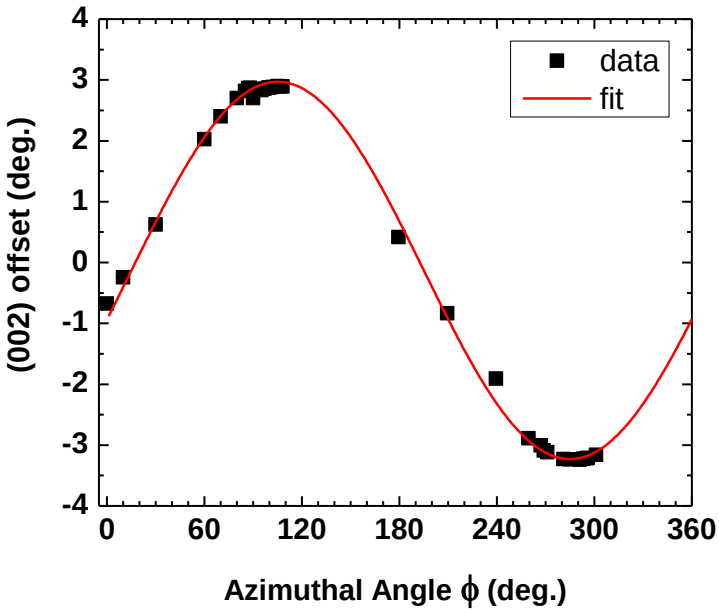

Figure 2.1 Incident angle of peak for (002) reflection as a function of azimuthal angle. Data were fit to a sine wave with amplitude 3.1° and a shift of ϕ=15°. The miscut was 3.1° degrees towards $SrTiO_3$ [010].

The orientation of the $BiFeO_3$ and $SrRuO_3$ films was measured with respect to the $SrTiO_3$ substrate. We made a two dimensional scan of the offset and diffracted angle to accurately measure the rotations between reflections. The two dimensional reciprocal space map spanned a plane in reciprocal space containing the $SrTiO_3$ and $BiFeO_3$ (002) and $SrRuO_3$ (220) peaks. The scattering geometry was chosen such that the $SrTiO_3$ [010] was in the same plane as the incident beam (corresponding to ϕ = 105° in Figure 2.1). The reciprocal space map was taken at the azimuthal angle corresponding to the maximum offset for the $BiFeO_3$ (002) so that the maximum tilt angle could be measured, rather than a projection onto the scattering plane. We found that all three reflections had different orientations.

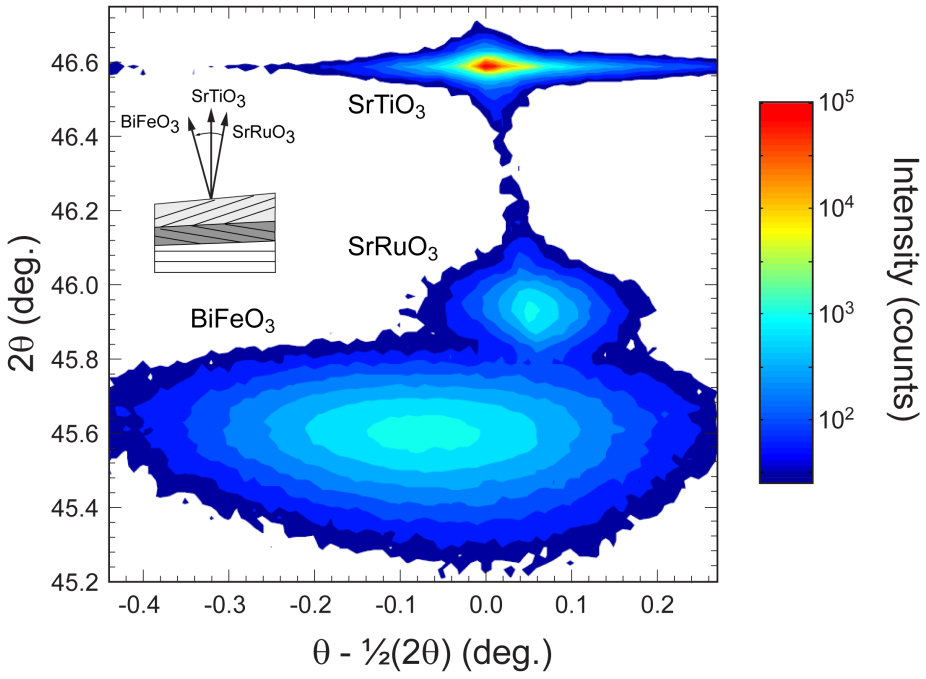

Figure 2.2. Area-averaged reciprocal space map of the $BiFeO_3$ (002), $SrRuO_3$ (220), and $SrTiO_3$ (002) at 8.05 keV. The offset angle is normalized to zero degrees at the $SrTiO_3$ (002).

Rotations of the $SrRuO_3$ and $BiFeO_3$ layers were measured from the reciprocal space map of the $SrTiO_3$ (002), $BiFeO_3$ (002), and $SrRuO_3$ (220) reflections (Figure 2.2). Both the $SrRuO_3$ and $BiFeO_3$ (002) reflections are rotated from the $SrTiO_3$ (002), as shown schematically in the inset of Figure 2.2. The $SrRuO_3$ reflection is rotated by 0.057° from the substrate reflection away from the sample surface. A more accurate value of the $SrRuO_3$ orientation can be obtained by recording the difference in offsets of $SrRuO_3$ and $SrTiO_3$ peak maxima when the miscut direction is in the scattering plane, repeating the measurement after rotating the azimuthal angle 180°, and taking the average. This was 0.053°. The offset for

the $BiFeO_3$ reached a maximum when the miscut direction lay in the scattering plane as in Figure 2.2, meaning that the $BiFeO_3$ tilt direction was parallel to the miscut of the substrate. The $BiFeO_3$ (002) was rotated in the opposite direction, by 0.073° from the substrate, a total of 0.13° from the underlying $SrRuO_3$ film. The $BiFeO_3$ and $SrRuO_3$ layers were rotated by different mechanisms, both of which are discussed in the following sections.

2.3.2. $SrRuO_3$ rotation by expansion at step edges

The rotation of the $SrRuO_3$ film can be described by a simple model of elastic relaxation at step edges. Nagai observed this effect in GaInAs films on GaAs substrates,[18] and explained it based on the insight that the film is clamped to the substrate at step edges, where it is forced to have the same out-of-plane lattice constant as the substrate. At the edge of a terrace, however, there is no clamping effect and the film can take on an elastically relaxed lattice constant. This lattice constant can be predicted using the in-plane compression of the film enforced by the substrate (a_{STO} = 3.905 Å) and assuming a Poisson's ratio of 0.3.[19,7] Nagai's model, sometimes called the "step-edge expansion model," is illustrated for a compressively strained film in Figure 2.3.

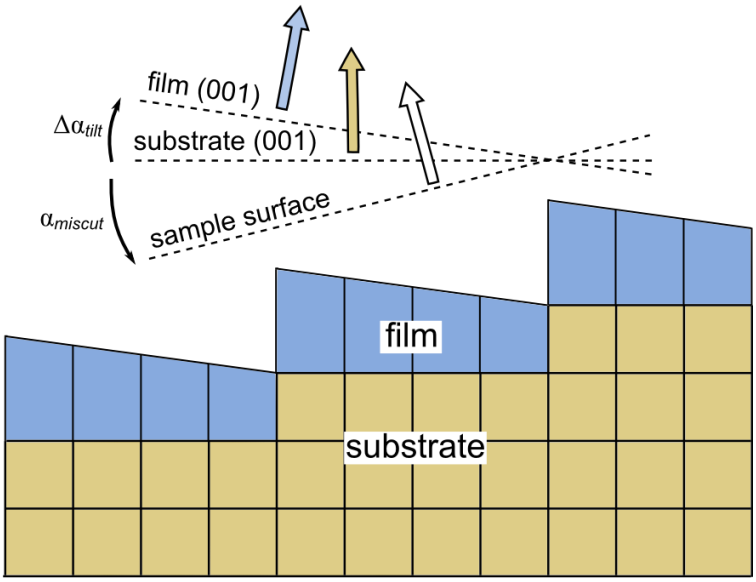

Figure 2.3. Step edge relaxation for a compressively strained epitaxial film, after Nagai (ref. 18). Each unit cell is represented by a quadrilateral. The expansion and miscut angle are greatly exaggerated to illustrate the principle. $\Delta\alpha_{tilt}$ is the rotation angle of the film atomic planes and α_{miscut} is the miscut angle.

A quantitative model of step-edge expansion was formulated by Ayers and Gandhi which predicts the magnitude and direction of the film rotation based on the unit cell parameters.[20] The rotation angle is given by:

$$\Delta\alpha_{tilt} = \tan^{-1}\left(\frac{c_{substrate} - c_{film}}{c_{substrate}}\tan\alpha_{miscut}\right)$$

Here $\Delta\alpha_{tilt}$ is the rotation angle, $c_{substrate}$ and c_{film} are the out-of-plane lattice constants of the substrate and strained film respectively, and α_{miscut} is the miscut angle of the substrate. A negative angle indicates rotation away from the surface normal. Note that this model assumes that the distance between atomic steps and the film's elastic compliance are large enough to fully expand or contract at the edge of a terrace.

The step-edge expansion model accurately describes the rotation of the $SrRuO_3$ layers in Figure 2.2. Using a pseudocubic out-of-plane lattice constant of c_{SRO} = 3.97 Å for the film, a bulk $SrTiO_3$ lattice constant of $c_{substrate}$ = 3.905 Å, and the measured miscut angle of 3.1°, the predicted rotation for $SrRuO_3$ on $SrTiO_3$ is -0.050°. The observed rotation is -0.053°. The observed rotation is thus in excellent agreement with the predicted value, both in direction and magnitude.

The step-edge expansion model does not explain the rotation of the $BiFeO_3$ film. From the reciprocal space map in Figure 2.2, we found that the out-of-plane $BiFeO_3$ lattice constant was c_{BFO} = 3.99 Å. When we use c_{SRO}= 3.97 Å for the substrate lattice constant, the predicted rotation is $\Delta\alpha$ = -0.015°. The observed angle between the $BiFeO_3$ and $SrRuO_3$ was +0.135°. The step edge expansion model is not even qualitatively correct and cannot be responsible for the $BiFeO_3$ rotation.

2.3.3. $BiFeO_3$ rotation caused by anisotropic defect nucleation

The disparity between the observed and predicted elastically induced rotations of the $BiFeO_3$ thin film lead us to consider other mechanisms that could be responsible for the tilting. As noted by Ayers and Gandhi, the step relaxation model assumes the film is pseudomorphic and that there is no relaxation via the introduction of misfit dislocations.[20] Elasticity theory predicts an out-of-plane lattice constant of $BiFeO_3$ in a pseudomorphic elastically strained film on $SrTiO_3$ would be 4.14 Å, assuming an in-plane lattice constant equal to $SrTiO_3$ (3.905 Å) and a Poisson ratio of 0.3. The measured value is c = 3.99 Å,

which is between the bulk and pseudomorphic constants. The epitaxial strain is thus partially relaxed. We show here that the dislocation mechanism responsible for the relaxation is what rotates the film.

We tested the hypothesis that the rotation of the $BiFeO_3$ results from preferential nucleation of dislocations in response to shear stresses. This effect was discovered in epitaxial SiGe on miscut Si (001) substrates.[21] Relaxation in SiGe occurs by nucleation of defects at the film surface which glide along the {111} planes to the film-substrate interface.[22,23] These dislocations have Burgers vectors along ½ <101> directions. The component of the dislocation parallel to the film-substrate interface reduces the strain energy stored in the film, which in this case is the [100] or [010] direction.

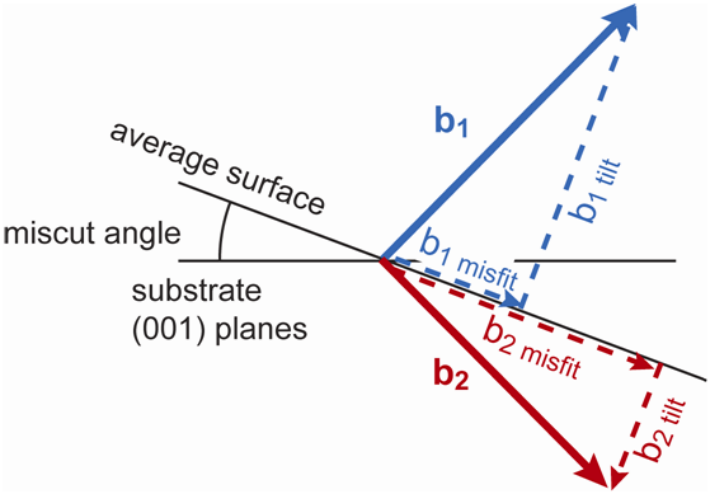

Figure 2.4 Components of dislocations relaxing an epitaxial thin film on a miscut substrate, after Mooney *et al.*, ref.21. The Burgers vectors b_1 and b_2 can be decomposed into b_{misfit} and b_{tilt}. The component b_{misfit} results from the projection of the Burgers vector onto the epitaxial stress applied to the film and is the component which relaxes the film. b_{tilt} rotates the (001) planes of the film. The misfit component of b_2 is larger than that of b_1, so that dislocations with Burgers vector b_2 are preferentially nucleated.

Two of the Burgers vectors **b** that can relax a compressively strained film are labeled $\mathbf{b_1}$ and $\mathbf{b_2}$ in Figure 2.4. Each has a misfit component $\mathbf{b}_{misfit}$, relaxing shear stress in the film, and a component $\mathbf{b}_{tilt}$ that rotates (001) planes. On a miscut substrate there is a larger resolved shear stress on one of the two slip systems because the stress lies in the plane of the average surface rather than in the (001) plane. The activation energy for nucleating dislocations decreases with stress parallel to **b**, so one of the slip systems is preferentially nucleated. Tilt components of the preferred slip system for the compressively strained $BiFeO_3$ on $SrTiO_3$ system, $\mathbf{b_2}$ in Figure 2.4, rotate $BiFeO_3$ towards the surface normal. The situation would be reversed for films under tensile stress, leading to rotations in the opposite direction.

The dislocations necessary for the relaxation mechanism of ref. 21 have been observed in epitaxial perovskite thin films. Dislocations with a $[01\bar{1}]$ Burgers vectors would simultaneously relax the misfit strain and rotate the $BiFeO_3$ layer in the observed direction. Dislocations in this family have been observed in other perovskite films on $SrTiO_3$. Oh *et al.* found misfit dislocations in $SrRuO_3$ films on $SrTiO_3$ substrates with <101> type Burgers vectors,[24] and Stemmer *et al.* observe stacking fault dislocations with **b** = ½ <101> in $PbTiO_3$ films on $SrTiO_3$ substrates.[25] We believe **b** = $[01\bar{1}]$ defects could be nucleated preferentially by the anisotropic stress and rotate the film, as in the SiGe system. Preferential nucleation on a miscut substrate leads to an overall tilt towards the surface normal in compressively strained films, in agreement with experimental observations.

The magnitude of the tilt produced by preferential nucleation of defects cannot be easily predicted. The tilt angle depends on the density of defects in the film, the dynamics of defect propagation through the film, and their rate of nucleation. The biggest challenge is quantifying the dynamics, since they depend on the energy required to nucleate a defect, the growth temperature, epitaxial strain as a function of temperature, among other factors.[26] The dynamics of defect motion are complicated, making it difficult to predict the amount of rotation of the film.

2.4. Mosaic block rotation

Probing smaller regions of the film with a focused beam gives information that a large beam cannot. The large-beam diffraction pattern is the average structure of the entire film. On the local scale, the film is broken up into mosaic blocks which each have different orientations. When the scattering volume includes many mosaic blocks, the variation in mosaic block orientations broadens x-ray reflections. This broadening makes it difficult to observe more subtle features of the diffraction pattern, such as structural differences between ferroelectric domains. Rather than averaging over many orientations, we used a focused x-ray beam to study small regions of the film to avoid the reflection-broadening problem.

Synchrotron x-ray microdiffraction was used to image mosaic blocks and measure their orientation. The (002) intensity was mapped over an area of the sample and reciprocal space maps were taken in multiple places. Figure 2.5 (a) is a real space map of the $BiFeO_3$ (002) reflection in a 10 μm × 10 μm region of the sample. The diffractometer was aligned to the maximum intensity of the $BiFeO_3$ (002) reflection at the position marked 1 and the

sample was scanned underneath the focused beam. High intensity corresponds to regions in which the (002) planes have the same interplanar spacing and orientation as at position 1. Low intensity regions have different orientations than the region at position 1.

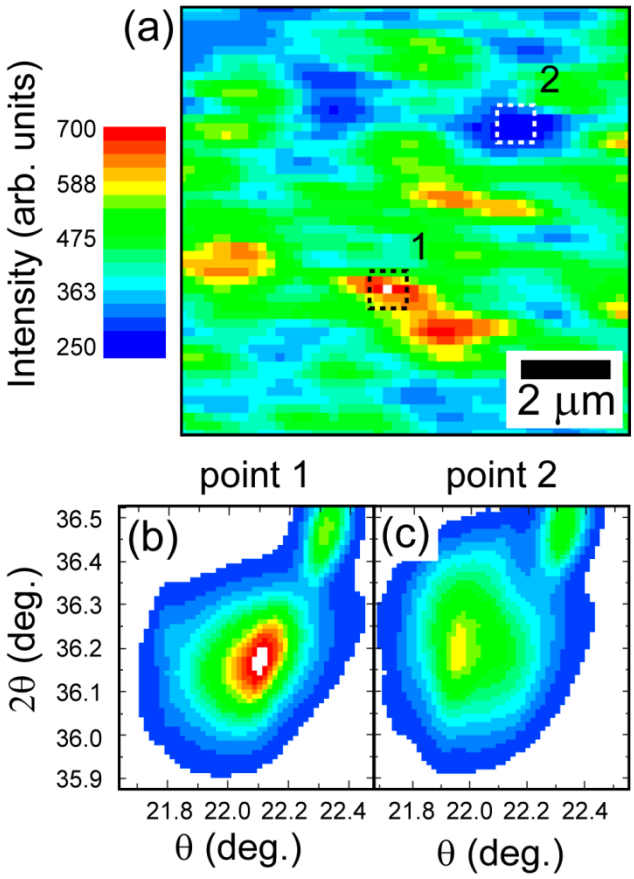

Figure 2.5 (a) X-ray microdiffraction image of mosaic blocks using the (002) reflection of $BiFeO_3$, acquired with diffractometer angles held at the maximum intensity in the area marked 1. (b), (c) Reciprocal space maps taken at positions 1 and 2 on the surface at 11.5 keV.

The orientations of two mosaic blocks were determined by acquiring reciprocal space maps of the (002) reflections. Reciprocal space maps were taken at the positions labeled 1 and 2 within the microdiffraction map and are shown in Figure 2.5 (b) and Figure 2.5 (c),

respectively. There is a 0.15° rotation between (002) planes at position 1 and 2. Although the maxima of the peaks appear at different incident angles, the total magnitude of the reciprocal space vector is the same at both positions. The d-spacing of the planes is the same, but the planes have been rotated with respect to each other. Furthermore, the reflections from regions 1 and 2 are part of the larger diffraction pattern in Figure 2.2. These are signatures of mosaic blocks. In this film the mosaic blocks are on the order of 1μm across.

These diffraction patterns indicate that the orientation of the film is inhomogeneous at the micron scale. The film as a whole is rotated on average by 0.13° with respect to the $SrRuO_3$ immediately beneath it, but there is an addition random rotation for each mosaic block. A second important observation is that, despite this inhomogeneity, we find that there is always only one (002) reflection within the scattering volume. If the focused beam were bigger, then we would observe two or more reflections from multiple mosaic blocks. Within this scattering volume there is only one orientation of the (001). Any ferroelectric domains within the scattering volume have unit cells with parallel (001) planes, which was relevant in determining domain patterns.

2.5. Strained stripe domains within mosaic blocks

Determining the domain pattern is important because of its importance to the conductivity, switching dynamics, and magnetic properties of $BiFeO_3$. X-ray diffraction patterns provide information about the ferroelectric domain structure by using the structural signatures of the polarization domains. The domain pattern can be inferred from (002) and {103} diffraction patterns obtained with the focused beam. We observed a single (002)

reflection in Figure 2.5, from which we can conclude that the domains within each mosaic block share a common basal plane formed by the **a** and **b** lattice vectors. The polarization within these domains can lie along any one of the eight members of the <111> family. There are thus four possible shapes of the unit cell, which we will call structural variants. The four variants can be considered as separate crystallites, rotated azimuthally in increments of 90° about the [001] axis, as shown below in Figure 2.6.

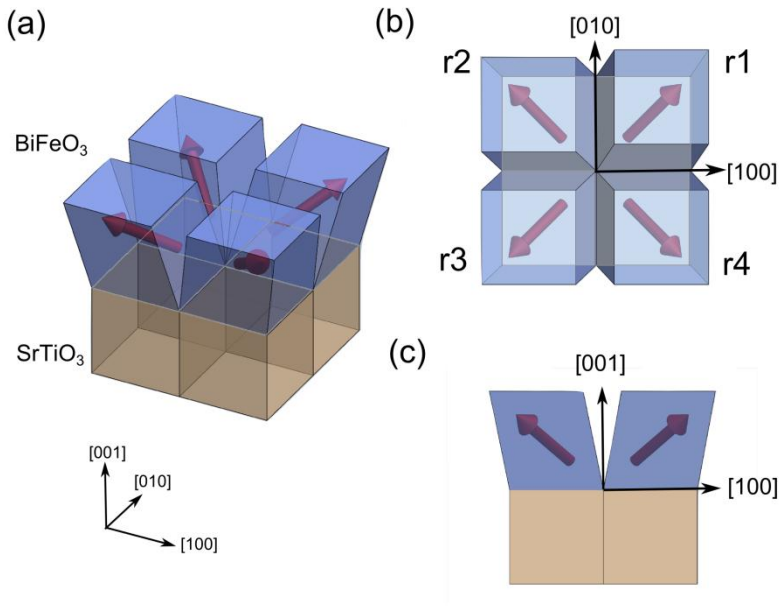

Figure 2.6 (a) Four structural variants of a rhombohedral ferroelectric film on a cubic substrate. The red arrows indicate one of two possible polarization directions for each variant. The other possible polarization is antiparallel. (b) Top down view along the $SrTiO_3$ [001] direction. Each variant is labeled r1-r4 and corresponds to an elongation parallel to a different member of the <111> family. (c) Cross sectional view along the $SrTiO_3$ [010] direction.

In a rhombohedral system, families of reflections that would have identical d-spacings for a cubic crystal are distinct. For example, in the pseudocubic notation there are two different d-spacings associated with reflections from the {103} family of planes. In

diffraction patterns, we can thus find several reflections from $BiFeO_3$ at each of the reciprocal space locations where we would have a single cubic reflection. The diffraction condition for the (103) of variant r1 is very close that of the (013) of another variant, r2, because the $BiFeO_3$ unit cell is very close to a cube. By taking a large reciprocal space map, the Bragg conditions can be met in turn for reflections from all of the variants present in the diffraction volume.

To eliminate the problem of mosaic spread obscuring multiple peaks, we used x-ray microdiffraction to probe a small area rather than the average of the entire film. In experiments with larger, millimeter-scale x-ray beams, the mosaic spread broadened the {103} reflections so much that it was not possible to distinguish between reflections from different variants. The focused x-ray beam probed a diffraction volume containing one or two mosaic blocks, compared to millions of mosaic blocks probed by a millimeter-sized beam. X-ray microdiffraction made it possible to accurately determine angles between multiple reflections.

2.5.1. $BiFeO_3$ {103} reflections

We probed the in-plane structure and determined the ferroelectric domain pattern from microdiffraction patterns of the {103} $BiFeO_3$ reflections. A real space map of the $BiFeO_3$ {103} intensity was acquired to determine the size of the ferroelectric domains. The real-space map shown in Figure 2.6(a) was obtained by holding the diffraction conditions constant while scanning the sample underneath the focused beam. The angles of the incident and outgoing beams with respect to the sample were fixed at the maximum of the strongest

$BiFeO_3$ {103} reflection at the point labeled 1 in Figure 2.7(a). Regions of high intensity have the same lattice constant and orientation as at position 1. The incident angle for the $BiFeO_3$ pseudocubic {103} reflections was approximately 44°, leading to a beam footprint of 400 nm × 275 nm.

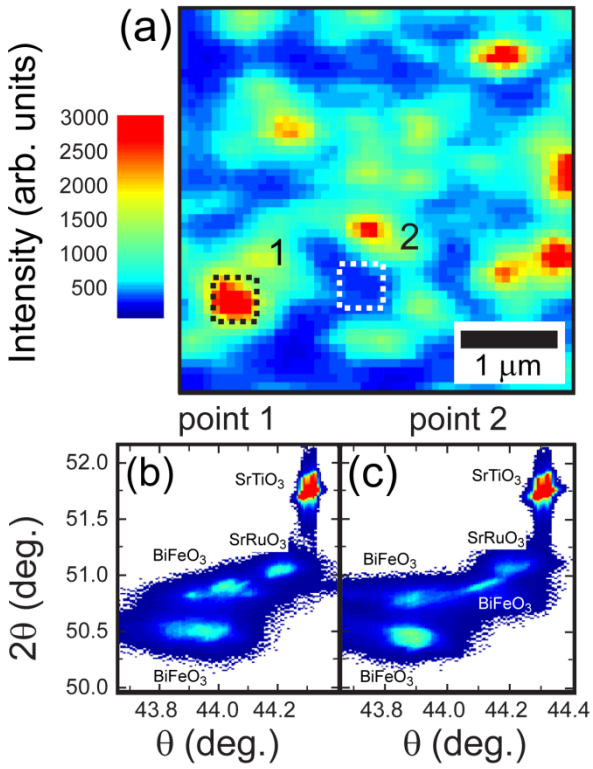

Figure 2.7 Microdiffraction image using the $BiFeO_3$ {103} reflections at 2θ = 50.73° at the area marked 1. Reciprocal space maps taken at positions 1 (b) and 2 (c) on the surface.

There are multiple ferroelectric domains in each mosaic block. There is more than one $BiFeO_3$ reflection near the $SrTiO_3$ (103), which shows that multiple structural variants were present in the scattering volume. Reciprocal space maps acquired at the points labeled 1 and 2 are shown in Figure 2.7(b) and (c). The reciprocal space maps in Figure 2.7(b) and (c)

show at least two or three $BiFeO_3$ reflections, respectively. This indicates that there are regions within the scattering volume which have different lattice spacings and orientations with respect to the substrate. The $SrRuO_3$ and $SrTiO_3$ (103) reflections are on the right side of the figures and have sharp peaks indicating uniform interplanar spacing. The width of the $BiFeO_3$ reflections is increased by the complicated strain state imposed by incomplete relaxation of epitaxy with the substrate. The presence of multiple $BiFeO_3$ {103} peaks are a signature of multiple polarization domains within a single mosaic block.

The rotations between multiple mosaic blocks within the diffraction volume could have produced a number of reflections. The diffraction pattern of each block would be rotated about the origin in reciprocal space and multiple Bragg reflections at all of the reciprocal lattice vectors. However, we have consistently observed a single (002) reflection with the focused beam. The diffraction volume in the film was smaller for the (002) than for the (103), making it more likely to observe splitting in the (002). Therefore, we do not believe that mosaic block rotation is responsible for the presence of multiple $BiFeO_3$ {103} reflections in each location.

2.5.2. Strained rhombohedral stripe domain pattern

The ferroelectric domain structure of $BiFeO_3$ was determined by comparing our microdiffraction results to predictions for domain patterns of a ferroelectric rhombohedral film on a cubic substrate. Streiffer *et al.* calculated the minimum energy configuration for a model ferroelectric rhombohedral film on a cubic substrate and found that the total strain energy was reduced by forming a striped domain pattern.[27]

Streiffer *et al.* identified all possible domain walls by determining planes for which two domains have identical electrostrictive displacement. After transforming from the high-temperature paraelectric cubic phase to the ferroelectric rhombohedral phase the domains are displaced by electrostrictive forces. By calculating the energy required to deform rhombohedral domains to epitaxially conform to the substrate, the strain energy can be obtained. The strain energy is modeled by what has been referred to as coherency defects. Coherency defects are edge dislocations which account for the misfit strain. Screw dislocations shear the unit cell to make a 90° angle between ***a*** and ***b*** lattice vectors. The electronic contributions from the polarization were considered, and domain patterns which did not have electrically neutral domain walls could be eliminated. These criteria were used to identify geometric configurations of ferroelectric domains with the lowest possible strain and electrostatic energies.

The ferroelectric domain patterns that minimize all of these energies have several characteristics. The patterns consist of alternating stripes of two polarizations. Both polarization domains are epitaxially constrained by the substrate. There is a 71° angle between polarization vectors of neighboring domains in four of the patterns. 71° stripe domain patterns have been observed in similar $BiFeO_3$ (001) films using PFM.[28,29] In these particular patterns, the domains share a common (001) plane. This is consistent with the (002) diffraction pattern observed in Figure 2.5.

The rhombohedral stripe domain model was used to predict which reflections could be observed at the reciprocal space locations of the $BiFeO_3$ {103} reflections. In the model domain pattern we propose, the r1, r2, r3, and r4 structural variants have a shared set of (001)

planes. To predict the diffraction pattern of this configuration, we calculated the wavevectors $\boldsymbol{q}$ corresponding to x-ray reflections from each variant. This was done for two models; a monoclinic state as would occur in a pseudomorphic, unrelaxed film and a strained rhombohedral state found in partially relaxed film. Neither model proposes new phases of $BiFeO_3$. Instead these model test different strained non-equilibrium states of the rhombohedral phase.

First, we tested the monoclinic model described by Streiffer *et al*.[27] This model assumes that the film is strained into a metastable monoclinic structure. We calculated the reciprocal lattice vectors for all four variants of a fully coherent film within one mosaic block and compared the predicted values to the three dimensional reciprocal space map of the {103} reflections shown in Figure 2.8. We used a monoclinic M_C structure (in which the $\boldsymbol{c}$ lattice vector is rotated in the (110) plane) with lattice constants $a = b = 3.905$Å, $c = 3.99$Å, and monoclinic tilt angle 0.6° to calculate the reciprocal lattice vectors. Two sets of variants produced reflections at the same reciprocal space vectors so the r1 (103) and r4 (013) have $\boldsymbol{q}_{\{103\}} = (1.609, 0, 4.712)$, while the r2 (0-13) and r3 (-103) have $\boldsymbol{q}_{\{103\}} = (1.609, 0, 4.736)$. The in-plane components of the predicted reflections do not match those observed in a three dimensional reciprocal space map of the (103) reflection. Moreover, there is no way for two variants with monoclinic symmetry in a coherent block to be split in $\boldsymbol{q}_y$ as found experimentally in Figure 2.8 (b). The monoclinic model is incorrect because the film is not coherent.

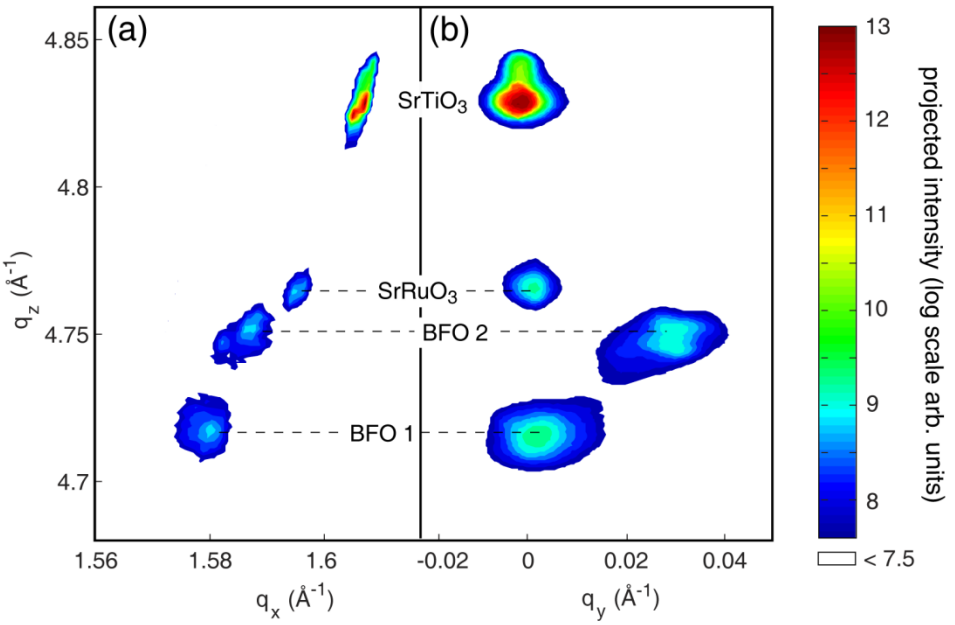

Figure 2.8. Three dimensional reciprocal space map of the $SrTiO_3$, $SrRuO_3$, and $BiFeO_3$ {103} reflections projected onto the (a) q_x-q_z plane and (b) the q_y-q_z plane.

A relaxed rhombohedral stripe domain model gave insight into the domain pattern. The peak splitting observed in Figure 2.8 is consistent with relaxed stripe domains. Models in which the angle between the pseudocubic ***a*** and ***b*** lattice vectors is less than 90° fit the splitting of the {103} quite well. After lifting this constraint there were too many variables to uniquely solve the structure and identify the exact structural variant based solely on the {103} reciprocal space map. Only triclinic models were able to match the observed pattern exactly.

. We examined a series of rhombohedral and triclinic models with different lattice constants and discovered they shared an important trend. For all tested structures, the reciprocal lattice vectors for the r1 (103) and r4 (013) reflections always have a larger magnitude than those of the r2 ($0\bar{1}3$) and r3 ($\bar{1}03$) reflections. The peak labeled BFO 2 can be assigned to either r1 or r4, and r2 or r3 to BFO 1. All of the four possible variant

combinations are consistent with the 71° stripe domain pattern discussed above. Therefore we conclude that these films contain the stripe domains in Streiffer *et al.* which have been anisotropically strained into a triclinic state.

2.6. Conclusions

Epitaxial $BiFeO_3$ (001) films grown on miscut substrates undergo anisotropic relaxation. The anisotropy in stress applied to the film causes anisotropic nucleation of defects, destroying the in-plane symmetry as well as resulting in a net rotation of the entire film. X-ray microdiffraction further shows the presence of multiple structural domains within individual mosaic blocks. The splitting of off-specular reflections were compared with predicted scattering from 71° rhombohedral stripe domains which share {101} type domain walls.

These results are consistent with *strained* rhombohedral stripe domains. As the epitaxial strain is relaxed via the introduction of defects, $BiFeO_3$ films return to the equilibrium rhombohedral symmetry. Unrelaxed (001) $BiFeO_3$ films are strained into monoclinic symmetry by the epitaxial stress of the substrate.[6] Partially relaxed films like the ones studied here have triclinic symmetries somewhere between monoclinic and rhombohedral. $BiFeO_3$ films with different symmetries are not new thermodynamic phases, just variations in the degree of epitaxial strain.

2.7. Chapter 2 references

[1] J. Wang, J. B. Neaton, H. Zheng, V. Nagarajan, S. B. Ogale, B. Liu, D. Viehland, V. Vaithyanathan, D. G. Schlom, U. V. Waghmare, N. A. Spaldin, K. M. Rabe, M. Wuttig, and R. Ramesh, "*Epitaxial $BiFeO_3$ multiferroic thin film heterostructures*," Science **299**, 1719 (2003).

[2] G. Xu, J. Li, and D. Viehland, *"Ground state monoclinic (M-b) phase in (110)(c) $BiFeO_3$ epitaxial thin films,"* Appl. Phys. Lett. **89**, 222901 (2006).

[3] S. Geprägs, M. Opel, S. T. B. Goennenwein, and R. Gross, "*Multiferroic materials based on artificial thin film heterostructures,"* Philos. Mag. Lett. **87**, 141 (2007).

[4] K. Saito, A. Ulyanenkov, V. Grossmann, H. Ress, L. Bruegemann, H. Ohta, T. Kurosawa, S. Ueki, and H. Funakubo, *"Structural Characterization of $BiFeO_3$ Thin Films by Reciprocal Space Mapping,"* Jpn. J. Appl. Phys. Part 1 **45**, 7311 (2006).

[5] R. J. Zeches, M. D. Rossell, J. X. Zhang, A. J. Hatt, Q. He, C. H. Yang, A. Kumar, C. H. Wang, A. Melville, C. Adamo, G. Sheng, Y.–H. Chu, J. F. Ihlefeld, R. Erni, C. Ederer, V. Gopalan, L. Q. Chen, D. G. Schlom, N. A. Spaldin, L. W. Martin, and R. Ramesh, *"Ground state monoclinic (M-b) phase in (110)(c) $BiFeO_3$ epitaxial thin films,"* Science **326,** 977 (2009).

[6] G. Xu, H. Hiraka, G. Shirane, J. Li, J. Wang, and D. Viehland, *"Low symmetry phase in (001) $BiFeO_3$ epitaxial constrained thin films,"* Appl. Phys. Lett. **86**, 182905 (2005).

[7] M. D. Biegalski, K. Dörr, D. H. Kim, and H. M. Christen, "*Applying uniform reversible strain to epitaxial oxide films,"* Appl. Phys. Lett. **96**, 151905 (2010).

[8] H. Liu, P. Yang, K. Yao, and J. Wang, *"Twinning rotation and ferroelectric behavior of epitaxial $BiFeO_3$ (001) thin film,"* Appl. Phys. Lett. **96,** 012901 (2010).

[9] Q. Gan, R. A. Rao, and C. B. Eom, "*Control of the growth and domain structure of epitaxial $SrRuO_3$ thin films by vicinal (001) $SrTiO_3$ substrates*," Appl. Phys. Lett. **70,** 1962 (1997).

[10] R. A. Rao, Q, Gan, and C. B. Eom, "*Growth mechanisms of epitaxial metallic oxide $SrRuO_3$ thin films studied by scanning tunneling microscopy,"* Appl Phys. Lett. **71**, 1171 (1997).

[11] H. W. Jang, D. Ortiz, S. H. Baek, C. M. Folkman, R. R. Das, P. Shafer, Y. Chen, C. T. Nelson, X. Pan, R. Ramesh, and C. B. Eom, "*Domain engineering for enhanced ferroelectric properties of epitaxial (001) $BiFeO_3$ thin films*," Adv. Mater. **21**, 817 (2009).

[12] R. R. Das, D. M. Kim, S. H. Baek,, C. B. Eom, F. Zavaliche, S. Y. Yang, R. Ramesh, Y. B. Chen, X. Q. Pan, X. Ke, M. S. Rzchowski, and S. K. Streiffer, "*Synthesis and ferroelectric properties of epitaxial $BiFeO_3$ thin films grown by sputtering*," Appl. Phys. Lett. **88**, 242904 (2008).

[13] Seidel, J. *et al*. *"Conduction at domain walls in oxide multiferroics,"* Nature Mater. **8**, 229 (2009).

[14] Y. B. Chen, M. B. Katz, X. Q. Pan, R. R. Das, D. M. Kim, S. H. Baek, and C. B. Eom,*"Ferroelectric domain structures of epitaxial (001) $BiFeO_3$ thin films,"* Appl. Phys. Lett. **90**, 072907 (2007)

[15] L. W. Martin, *et al*. "*Nanoscale control of exchange bias with $BiFeO_3$ thin films,"* Nano Lett. **8**, 2050 (2008).

[16] S. F. Liu, S. E. Park, H. Lei, L. E. Cross, T. R. Shrout,*"E-field dependence of piezoelectric properties of rhombohedral PZN-PT single crystal,"* Ferroelectrics **221,** 169 (1999).

[17] B. E. Warren, *X-ray Diffraction*, (Dover Publications, New York, 1990).

[18] H. Nagai, "*Structure of vapor deposited $Ga_xIn_{1-x}As$ crystals*," J. Appl. Phys. **45**, 3789 (1974).

[19] C. Ederer and N. A. Spaldin,*"Effect of epitaxial strain on the spontaneous polarization of thin film ferroelectrics,"* Phys. Rev. Lett. **95**, 257601 (2005).

[20] J. E. Ayers and S. K. Ghandhi, "*Crystallographic tilting of heteroepitaxial layers*," J. Cryst. Growth **113**, 430 (1991).

[21] P. Mooney, F. K. LeGoues, J. Tersoff, and J. O. Chu, *"Nucleation of dislocations in SiGe layers grown on (001),"* J. Appl. Phys. **75**, 3968 (1994).

[22] M. A. Capano, *"Multiplication of dislocations in $Si_{1-x}Ge_x$ layers on Si(001),"* Phys. Rev. B **45**, 768 (1992).

[23] C. J. Gibbings, C. G. Tuppen, and M. Hockly, *"Dislocation nucleation and propagation in $Si_{0.95}Ge_{0.05}$ layers on silicon,"* Appl. Phys. Lett. **54**, 148 (1989).

[24] T. Suzuki, Y. Nishi, and M. Fujimoto, *"Analysis of misfit relaxation in heteroepitaxial $BaTiO_3$ thin films,"* Phil. Mag. A **79,** 2461 (1999).

[25] S. Stemmer, S. K. Streiffer, F. Ernst, and M. Rühle, *"Dislocations in $PbTiO_3$ thin-films,"* Phys. Stat. Sol. A **147**, 135 (1995).

[26] E.P. Popov, *Introduction to Mechanics of Solids* (Prentice-Hall, 1968)

[27] S. K. Streiffer and C. B. Parker, "*Domain patterns in epitaxial rhombohedral ferroelectric films. I. Geometry and experiments"* J. Appl. Phys. **83**, 2744 (1998).

[28] F. Zavaliche, R. R. Das, D. M. Kim, C. B. Eom, S. Y. Yang, P. Shafer and R. Ramesh, *"Ferroelectric domain structure in epitaxial $BiFeO_3$ films,"* Appl. Phys. Lett. **87**, 182912 (2005)

[29] Y. -H. Chu, M. P. Cruz, C. -H. Yang, L. W. Martin, P .-L. Yang, J. -X. Zhang, K. Lee, P. Yu, L. -Q. Chen, and R. Ramesh, "*Domain control in multiferroic $BiFeO_3$ through substrate vicinality,"* Adv. Mater. **19,** 2662 (2007).

Chapter 3. X-ray Diffraction Signatures of Ferroelectric Polarization

The intensity of x-ray diffraction reflections in ferroelectric materials depends on the polarization direction. In fact, this change in intensity can be used to image ferroelectric domains.[1] In order to exploit this phenomenon, however, it is necessary to understand the origin of the intensity change. Kinematic scattering models predict changes in diffracted intensity originating from the change in atomic positions when the ferroelectric polarization is switched. For perovskite materials which are ferroelectric, the change is predicted to be several percent of the Bragg reflection intensity. Previous studies in other groups have observed intensity changes up to a few percent of the intensity in $BaTiO_3$ thin films, which fit the kinematic models quite well.[2] Do *et al*., in previous work within our research group, have previously observed large changes of up to 30% in the intensity of the (002) reflection of $Pb(Zr,Ti)O_3$ (PZT) thin films when the direction of the polarization is changed. [3,4] Calculating the structure factor for $PbTiO_3$, a ferroelectric with a structure similar to PZT, gives an intensity contrast of 5 to 10%, far less than the experimental observation.4 Based on the success of the kinematic scattering model with $BaTiO_3$, we theorized that with slight modifications the model could accurately predict the scattering from PZT films as well. Discrepancies between the predicted and experimental intensities were used to refine the kinematic scattering model. In the process, we improved our understanding of the structure of PZT films.

Refining the kinematic scattering model for PZT is also relevant to $BiFeO_3$. We observe intensity changes of 20% to 30% upon polarization switching in $BiFeO^3$ films, similar to PZT (001) films. Unlike PZT, $BiFeO_3$ (001) films have a complex structure as seen in Chapter 2, making it difficult to determine atomic positions accurately. Furthermore, when an electric field is applied along the $[001]_{pc}$ direction, the ferroelectric polarization switches to one of four possible directions. The uncertainty in atomic positions and multiple switching paths makes it extremely difficult to accurately predict the change in intensity of $BiFeO_3$ reflections after polarization switching.

Compared to $BiFeO_3$, PZT has a simple structure. At compositions far from the morphotropic phase boundary near x=0.5 PZT has a well-defined rhombohedral or tetragonal structural state at room temperature.[5] Tetragonal PZT, which occurs for compositions with x < 0.50, has a polarization parallel to the ***c*** axis of the unit cell. It is possible to deposit epitaxial films of tetragonal PZT on (001) $SrTiO_3$ substrates which have the *c* axis of the unit cell along the surface normal. The polarization in tetragonal PZT thin films of this type is constrained to be along one of only two polarization directions; it can be either parallel or antiparallel to the surface normal. When an electric field above the coercive field E_c is applied, there is only one stable polarization direction, making comparisons to intensity calculations for a single (*hkl*) reflection straightforward.

We hypothesize that the polarization-dependent intensity contrast is caused by similar phenomena for PZT and $BiFeO_3$. Both materials are perovskite ferroelectrics. Both are compressively strained epitaxial thin films. The Bi^{3+} or Pb^{2+}cations in $BiFeO_3$ and PZT have

similar ionic radii and unbonded lone pairs.[6] The structural similarities between $BiFeO_3$ and PZT lead us to believe that the intensity change upon polarization switching is likely to have similar origins in both materials. Thus, in order to determine the origin of the large intensity contrast in $BiFeO_3$ and simultaneously solve an open question about previous work, we studied the polarization-dependent intensity of the structurally simpler material, PZT.

Our hypothesis was that the atomic positions, scattering factors, or long range ordering assumed in the kinematic scattering model were incorrect, making the predicted intensities inaccurate. The key issue involved in simulating the diffraction patterns accurately is to account for these phenomena quantitatively. We tested several variations of the structure which could in principle lead to the large intensity contrast observed experimentally. One possible origin of this difference is inaccurate knowledge of the atomic positions within the PZT unit cell. The intensity contrast is sensitive to the distance between atoms, especially those with large atomic scattering factors. Even small displacements of the Pb^{2+} or Zr^{4+}/Ti^{4+} ions change the intensity contrast. A second possibility is that the atomic scattering factors of the atoms in PZT films differ from those used in the calculation. Because the intensity of a Bragg reflection depends on the imaginary part of the atomic scattering factor, uncertainties in these scattering factors can have a large impact on the results. The final possibility we considered is that the Zr and Ti atoms have a structure with sufficient long-range order to make the prediction inaccurate.

In order to determine the cause of the increased contrast between polarization domains in PZT, we measured the intensity contrast as a function of energy for several different x-ray reflections. Experimental results were compared to predictions from several kinematic

scattering models. First, the kinematic scattering from $PbTiO_3$ was calculated to qualitatively predict the intensity change for several reflections. The $PbTiO_3$ model predicts a sharp increase of the intensity contrast at absorption edges, so we focused on energies near the Pb L_3 edge at 13.035 keV. The intensities of several reflections were measured as a function of polarization direction and photon energy. We observed an increased intensity contrast at the Pb L_3 edge as predicted. Comparison between experimental and predicted intensities showed that the contrast depends on the distance between the Pb and Zr/Ti atoms and the imaginary part of the atomic scattering factor.

3.1. Kinematic scattering from $PbTiO_3$: A qualitative prediction for PZT intensity contrast

We hypothesized that the intensity contrast arises from the location of ions within the $Pb(Zr,Ti)O_3$ unit cell. These ions do not occupy centrosymmetric positions, and thus there can be a difference between the intensities of reflections with opposite indices. This effect has been used to determine the orientation of a non-centrosymmetric crystal using the difference in intensities of (111) and (-1-1-1) reflections in a ZnS crystal.[7] In these early x-ray scattering experiments, the experimenters measured the intensity of reflections with indices (111), rotated the crystal, and then measured the intensity of the (-1-1-1) reflection. In terms of atomic positions, rotating the ZnS crystal is similar to switching the polarization direction in a perovskite.

The same phenomenon can be used to determine the direction of the remnant polarization in ferroelectric perovskites. We model the crystallographic effect of reversing the direction of the polarization as being equivalent to inverting the crystal, so that the (*hkl*) planes *after* polarization switching are equivalent to the (*-h-k-l*) planes *before* switching. In order to predict the intensity contrast between polarization directions, we calculate the difference in structure factors of the (*hkl*) and (*-h-k-l*) reflections as a function of energy for several different planes.

3.1.1. Analytical expression for polarization-dependent intensity

The difference between the intensities of the (*hkl*) and (*-h-k-l*) reflections is predicted by calculating their structure factors. The structure factor *F* depends on the scattering wavevector $\boldsymbol{q}$, the atomic positions within the unit cell $\boldsymbol{r_n}$, the wavevector dependent part of the scattering factor f^0, and the energy dependent dispersion corrections to the real and imaginary parts, f' and f'', respectively. When $\boldsymbol{q}$ is equal to a reciprocal lattice vector $\boldsymbol{g_{hkl}}$, the structure factor reduces to:

$$F(hkl) = \sum_n (f_n^0 + f_n' - i f_n'')\, e^{2\pi i\,(hu_n + kv_n + lw_n)}$$

where *u*, *v*, and *w* are the fractional indices of the atomic positions, such that $\mathrm{r_n} = \mathrm{au_n} + \mathrm{bv_n} + \mathrm{cw_n}$. In tetragonal materials with a 4-fold rotation about the $\boldsymbol{c}$ axis, *h* and *k* are degenerate so there is no difference between the structure factors for the (*hk-l*) and (*-h-k-l*) planes. The analytical expression for the difference in intensities can be found by subtracting the structure factors for (*hkl*) and (*-h-k-l*) and simplifying the expression. For a unit cell with

n atoms, the difference in intensities is given by:

$$FF^*(hkl) - FF^*(\overline{hkl}) = 4\sum_{\alpha=1}^{n-1}\sum_{\beta=\alpha+1}^{n} \mathrm{Im}\left[f_\alpha^* f_\beta\right] \sin 2\pi\left[h(u_\alpha - u_\beta) + k(v_\alpha - v_\beta) + l(w_\alpha - w_\beta)\right]$$

The difference in intensity depends on the imaginary parts of the atomic scattering factors, the Miller indices of the particular reflection, and the atomic positions. The argument of the sine function above is the phase difference between x-rays scattered from atoms *j* and *k*. The difference in phase is caused by the difference in path lengths taken by x-rays scattering from the two atoms.

There would be no difference between the (*hkl*) and (*-h-k-l*) intensities if the imaginary part of the scattering factor were zero. There were two simple ways to test this theory - altering *h*, *k*, and *l* by diffracting from several different planes, and varying f'' by changing photon energy.

3.1.2. $PbTiO_3$ structure factor and definition of intensity contrast ratio

A framework for understanding energy dependence and sign of the intensity contrast was given in section 3.1.1. We can apply this model first to $PbTiO_3$ which has the same symmetry as the PZT crystal we have studied extensively. $PbTiO_3$ also has a simpler structure than PZT because it includes only one type of central atom and it thus can be described using a structure with a small unit cell that includes only single Pb and Ti atoms.

The $PbTiO_3$ structure factor is calculated for two polarization states to predict the intensity contrast ratio. The arrangements of atoms and the directions of the polarizations in the two states are shown in Figure 3.1. The *down* polarization state (P_{down}) has the

polarization pointing antiparallel to the ***c*** axis, towards the interface between the film and the substrate. This state can be produced by applying a positive voltage to the top electrode of a capacitor with the bottom electrode grounded. In a thin film diffraction experiment in which the x-ray beam enters and exits through the surface of the thin film, the P_{down} domain state produces x-ray reflections with indices (*hkl*) in which *l* is positive. In the *up* polarization state, P_{up}, the same x-ray scattering geometry produces reflections with negative values of *l*. The P_{up} state can be reached with by applying a negative voltage to the top electrode.

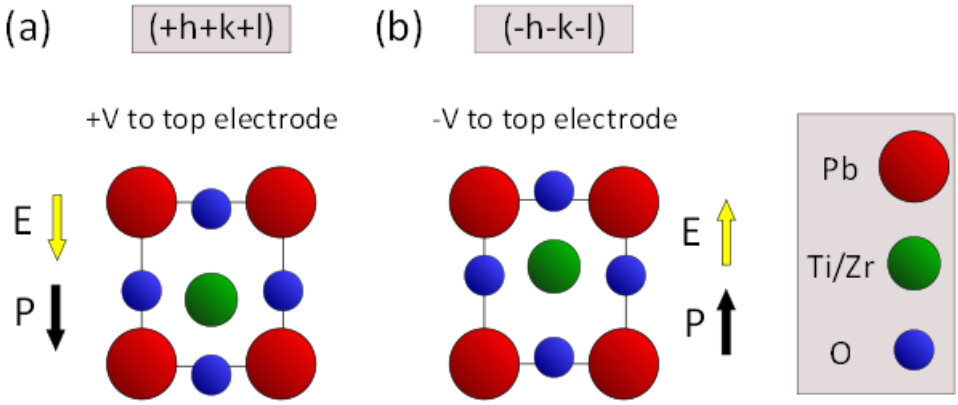

Figure 3.1. PZT unit cell in the (a) polarization down and (b) polarization up states. The central Ti/Zr atom and oxygen atoms change their positions along the c axis when the polarization is switched.

Structure factor calculations for $PbTiO_3$ were performed using atomic scattering factors and atomic positions found in the literature. Atomic scattering factors f_{Pb}, f_{Ti}, and f_O were taken from Henke *et al*. and calculated using the XOP computer program.[8,11] Atomic positions for $PbTiO_3$ were taken from Wyckoff.[9] In order to quantify the contrast in intensity between the P_{up} and P_{down} states, we defined a ratio of intensities:

$$ratio = \frac{I(hkl) - I(\overline{hkl})}{I(hkl)} = \frac{F(hkl)F^*(hkl) - F(\overline{hkl})F^*(\overline{hkl})}{F(hkl)F^*(hkl)}$$

This parameter is used to compare calculated and experimental values of the polarization dependent intensity. The intensity ratio for several reflections was calculated as functions of energy for comparison with experimental results.

3.1.3. Intensity ratio predictions

When there is no absorption of the x-ray photons by a crystal the scattering factors are completely real and *f'* is zero. In this hypothetical case, the scattering factor *F*(*hkl*) is equal to the complex conjugate of *F(-h-k-l)* and as a result the intensity given by FF^* does not change when all of the indices of the reflection change sign. This effect is known as Friedel's Law, and it provides a useful rule of thumb. As a result of Friedel's Law reflections with opposite indices have equal intensities even non-centrosymmetric crystals, as long as absorption can be neglected. This premise breaks down as soon as *f* '' becomes significant, most noticeably near absorption edges.

The magnitude of the intensity contrast depends on the energy of the x-ray photons. In a general sense, the intensities of Bragg reflections depend on the energy of the x-ray photons because the dispersion corrections to the atomic scattering factor, *f* ' and *f* '', have strong energy dependences. The imaginary part of the scattering factor, *f* '', is proportional to the absorption cross section σ_a:

$$f'' = \frac{|\boldsymbol{k}|}{4\pi r_0}\sigma_a$$

As a result, *f* '' increases sharply at the absorption edges. The relationship between *f* ' and *f* '' can be described via the Kramers-Kronig relation:[10]

$$f'(\omega) = \frac{2}{\pi}\int_0^{\infty} \frac{\omega' f''(\omega')}{\left(\omega'^2 - \omega^2\right)} d\omega'$$

In practice, we can use tabulated values of the dispersion corrections to predict the atomic scattering factors. Henke *et al*. provide tables of *f '* and *f ''* for elements with atomic numbers 1 to 92. [11]

The increase in *f ''* at absorption edges makes the intensity ratio largest at these photon energies. We carefully studied the intensity ratio at energies near the Pb L_3 absorption edge for two reasons. First, the predicted rapid variation in ratio predicted by the model would be easy to observe experimentally. Furthermore, the photon energies of absorption edges for the other constituents of PZT have wavelengths that are either too large or too small for microdiffraction experiments. The predicted intensity ratio is plotted as a function of energy near the Pb L_3 absorption edge is plotted Figure 3.2 for several reflections.

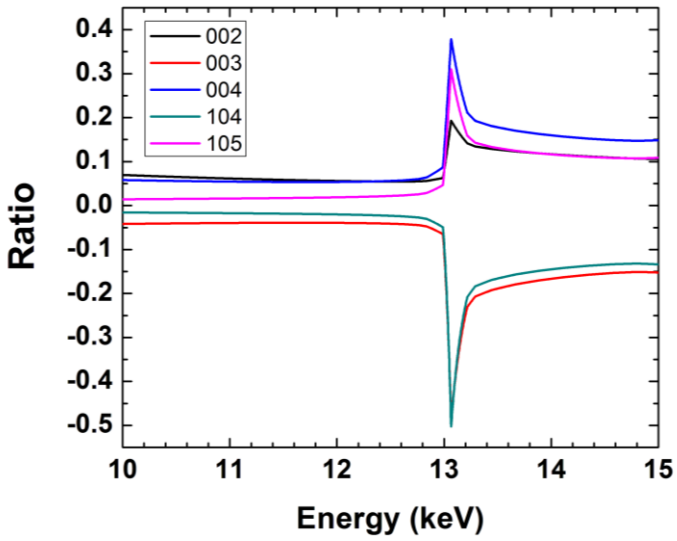

Figure 3.2. Qualitative prediction for intensity contrast ratio based on calculated values of the energy dependent $PbTiO_3$ structure factor.

The large jump in the magnitude of the ratio near 13 keV is caused by the increase in the imaginary part of the scattering factor of Pb at the L_3 absorption edge near 13.035 keV. The intensity ratio is also strongly dependent on the distance between the Pb and Ti ions, which affects the phase factor. This factor also depends on the difference in the imaginary components of the Pb and Ti scattering factors.

In Figure 3.2, a positive ratio indicates that the diffracted intensity for the P_{down} state is more intense than in the P_{up} state. The sign of the ratio at these energies is determined by the sum of Miller indices *h*, *k*, and *l*. When $h+k+l$ is even, the reflection is more intense in the P_{down} state; when $h+k+l$ is odd, the reflection is more intense in the P_{up} state. These sign rules only apply for $PbTiO_3$ at photon energies within several keV of the Pb L_3 edge because at photon energies near the Pb L_3 edge the intensity ratio is dominated by the lead and titanium f''.

3.2. Intensity contrast measurements

A series of measurements were designed to test the hypothesis that the polarization-dependent variation in the intensity of x-ray reflections is solely the crystallographic location of ions away from centrosymmetric positions. On the basis of the quantitative description developed in the previous section, we could test that hypothesis with the following specific predictions:

1) The P_{down} has higher intensity than P_{up} for reflections with $h+k+l=2n$.

2) The P_{up} state has higher intensity than P_{down} for reflections with $h+k+l=2n+1$

3) The magnitude of the intensity ratio will be maximized at photon energies near the Pb L_3 edge, 13.035 keV.

Based on these criteria, we measured the polarization dependent intensity for several reflections as a function of the photon energy, for a range of energies near the Pb L_3 edge.

The sample used in this study is an epitaxial thin film of (001) oriented $Pb(Zr_{0.45}Ti_{0.55})O_3$ on an $SrTiO_3$ substrate. This composition of PZT is tetragonal at room temperature and has a large remnant polarization.[12] A 100 nm-thick conducting $SrRuO_3$ layer between the PZT and the substrate acted as a bottom electrode. The PZT and $SrRuO_3$ thin films were deposited on a (001) $SrTiO_3$ substrate using off-axis radio-frequency sputtering by our collaborators in Prof. Chang-Beom Eom's group.[13] Circular top electrodes with various diameters from 25 μm to 200 μm were patterned by sputtering 20 nm of platinum on top of the PZT through a shadow mask. We used capacitors with 100 μm diameter top electrodes for these experiments. The out-of-plane lattice constants of the thin films were measured with a θ-2θ scan along the substrate surface normal direction of reciprocal space, including the $SrTiO_3$ (002), PZT (002), and $SrRuO_3$ (220) reflections.

We applied electric fields to capacitors to switch the ferroelectric polarization so we could measure the x-ray scattering from a region with a known, uniform polarization. Top electrodes were contacted with a high bandwidth 5μm tungsten probe tip (Cascade Microtech, 107-158). The $SrRuO_3$ bottom electrode was contacted by soldering a thin platinum wire to

an area at the corner of the sample where the film had been removed to expose the $SrRuO_3$ bottom electrode. This wire was connected to the outer coaxial connection of the probe tip. Electric fields were applied to the region underneath the top electrode by applying a voltage across the film thickness using a function generator (Agilent 33120A).

3.2.1. Microdiffraction experiments

The variation in the intensity of x-ray reflections of the PZT thin film was measured using synchrotron microdiffraction. The focused beam was used to probe regions under electrodes, each of which were uniformly poled. The intensity of each reflection was measured after poling the capacitor by applying positive voltages to the top electrode, which produced the P_{down} state, and negative voltages, which lead to the P_{up} state. The ratio of these intensities was computed from the data in order to compare with predictions from a $PbTiO_3$ kinematic scattering model.

A focused, monochromatic x-ray beam was used for the microdiffraction experiments. The x-ray beam was produced by a minigap undulator insertion device[14] at beamline X13b of the National Synchrotron Light Source (NSLS). The undulator had a gap of 3.3 mm and a corresponding maximum intensity at 11.46 keV. A Si (111) monochromator was used to select a monochromatic beam at various energies. The photon energy was calibrated at 11.103 keV using the Ge K edge absorption by measuring the drop in intensity with an ionization chamber after the beam had passed through a Ge foil. During the course of the experiment, the energy calibration was checked by measuring the x-ray fluorescence from lead tape at the Pb L_3 edge. The beam was focused using Kirkpatrick-Baez (K-B) mirrors to

a spot size of 10-20 μm.[15] K-B mirrors were used because they are achromatic, and thus their focal length does not change when the energy of the x-rays is varied.

Normalizing the diffracted signal to intensity variations in the incident beam was an essential step in accurately comparing multiple intensity measurements. The main source of variation in the incident beam came from the decay of the current inside the storage ring of the synchrotron. Electrons in a storage ring are continuously lost from the stored beam, leading effectively to a finite lifetime on the order of hours. This means that the current in the ring (and therefore the intensity of x-rays being produced) is constantly decreasing unless more electrons are injected into the ring. The current in the synchrotron storage ring at NSLS was injected once every twelve hours after dumping the residual stored electron beam. The beam current decreases significantly even over the course of an hour, so it is necessary to monitor intensity of the incident beam in order to avoid artifacts in the experimental results. This is commonly done by installing an ion chamber upstream of the diffractometer. In this experiment, diffracted intensities were normalized to the readout from an ion chamber that was placed in the hutch upstream from the sample, between the K-B mirrors.

The sample was mounted on a diffractometer in a vertical scattering geometry. The K-B mirrors focused the x-ray beam at the center of rotation of the diffractometer. The electrical probe tip was mounted on the diffractometer such that the tip could make contact with the top electrodes of capacitors on the sample. The tip, sample, and bottom electrode were set up to enable poling and hysteresis loop measurements of capacitors.

The diffracted beam was detected using a scintillation detector (Saint-Gobain, Bicron). The scintillation detector produces a single voltage pulse for each detected photon,

with a pulse height pulse proportional to the photon energy. The detector output was amplified and filtered using a single channel analyzer (SCA). We chose the SCA limits so only photons that were elastically scattered were counted. High energy photons from higher order harmonics of the undulator and low energy fluorescent photons were filtered out. The particular scintillation detector we used produces pulses with poorly defined heights, with a pulse-to-pulse variation of approximately 50% even for monochromatic photons. The SCA thus provided efficient discrimination against higher harmonics, but did not efficiently reduce the fluorescent noise from elements with edges just below the incident energy.

The angular resolution of the detector was set using slits placed directly in front of the detector. The 10mm × 6 mm slits were 36.8 cm from the sample and had an angular acceptance of 0.93° in 2θ and 1.55° in the horizontal direction, which was perpendicular to the scattering plane. This large acceptance allowed the integrated intensity of the reflection to be measured.

3.2.2. X-ray fluorescence

X-ray fluorescence provided a way to determine where the x-ray beam was on the sample. The fluorescent x-rays emitted from the sample were analyzed using a Si p-i-n diode fluorescence detector (AMPTEK XR-100CR) and a multichannel analyzer (Amptek MCA8000A). The presence or absence of fluorescent x-rays at energies corresponding to W, Pt, and Pb determined whether the focused beam was striking the tungsten probe tip, a platinum electrode, or the $Pb(Zr,Ti)O_3$ film, respectively.

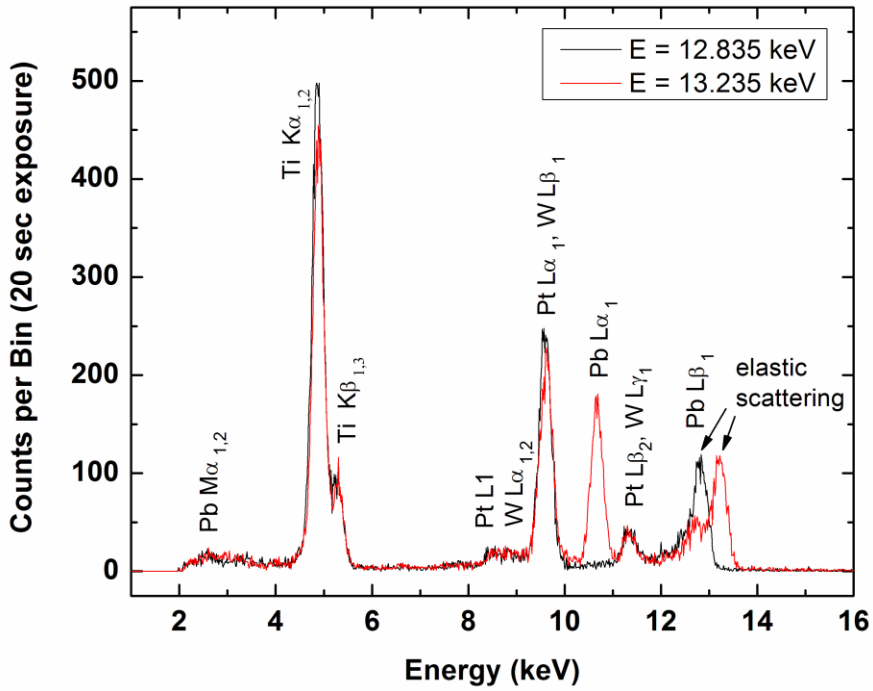

Figure 3.3. X-ray fluorescence spectrum from the PZT thin film at 12.835 and 13.235 keV.

Spectra with incident photon energies above and below the Pb L_3 edge were recorded to calibrate the fluorescence detector and identify the fluorescent signal from each element (Figure 3.3). The difference in peak position of the two elastic peaks was used to calibrate the energy range per bin in the MCA output. The peaks labeled elastic scattering include the truly elastic scattering as well as inelastically scattered x-rays that have been shifted to lower energies from Compton scattering. Peaks were identified by comparing to known emission spectra of Pb, Pt, Ti, and W.[16] The Pb $L\alpha_1$ edge fluorescent peak at 10.7 keV appears only when the incident energy is above the Pb L_3 edge at 13.035 keV.

The fluorescent signal was used to map the position of the focused beam on the sample. In order to measure the fluorescence signal arising from the Pb L_3 transition, we

integrated the photons with energies arriving in a region of interest (ROI) between 10 keV and 10.5 keV. The increase in Pb $L\alpha_1$ fluorescence at the Pb L edge was used to recalibrate the monochromator energy during the course of the experiment. The Pt L_α and W L_β transitions occur at nearly the same energies, so we defined an ROI which measured the sum of Pt and W signal. The Pt and W fluorescence proved to be useful in finding the electrical probe tip and capacitor top electrodes with the focused beam. Figure 3.4 shows the diffracted intensity from the PZT (004) and the Pt/W fluorescent signal that were recorded simultaneously as the sample was scanned underneath the beam.

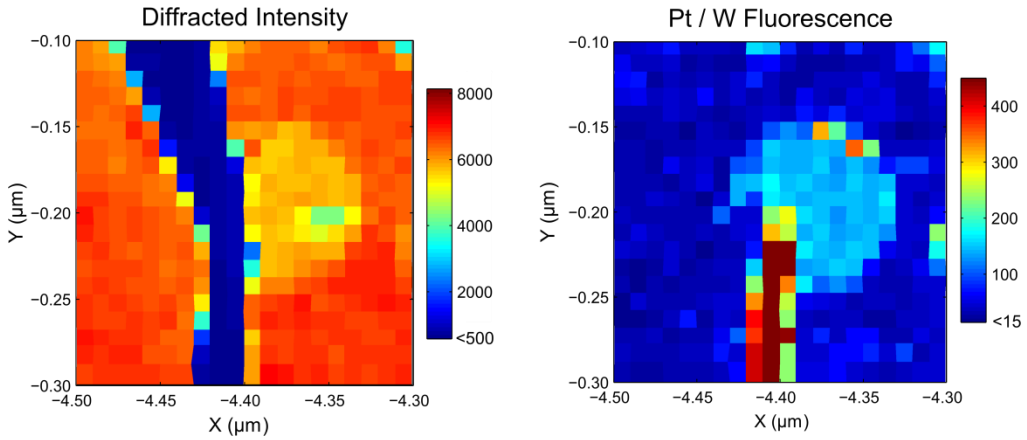

Figure 3.4. PZT (004) diffracted intensity and Pb / W x-ray fluorescence map of a 100 µm capacitor and the probe tip.

The diffracted intensity and fluorescence provided complimentary information during sample maps; the diffracted beam was attenuated by the probe tip and its shadow while the fluorescence clearly showed the presence of the electrode. The Pt top electrode absorbed some of the diffracted beam, but the intensity dependence on polarization direction and photon energy was larger than the absorption decrease. The Pt fluorescence did not vary with

photon energy or polarization direction, making it a reliable indication of whether the beam was on a capacitor.

3.2.3. Ferroelectric polarization switching

In order to measure the diffracted intensity from a well-defined polarization domain configuration, the capacitors were poled by applying an electric field. We measured ferroelectric hysteresis loops and used them to determine the coercive fields for this PZT film to ensure the polarization was completely switched, as described in Section 1.7.2. Three periods of a triangle waveform with an amplitude of 7 V and a frequency of 10 kHz were applied to top electrodes with a diameters of 100μm. The coercive fields were +350 kV/cm and -150 kV/cm. The apparent difference in coercive field is an effect of different materials in the top and bottom electrodes.[17]

The remnant polarization measured from the hysteresis loops was used to estimate the damage to the device. Exposure to intense x-rays can introduce electrical and structural defects in ferroelectric thin films. The remnant polarization $2P_r$ = 93 μC/cm^2 measured in Figure 1.6 was used as a baseline. Typical values of P_r for an as-grown capacitor in this film were around 40-45 μC/cm^2, which closely matches literature values in films of similar compositions ($0.4 > x > 0.52$) which range from 35μC/cm^2 to 45μC/cm^2.[18,19] P_r decreased with the number of switching cycles and exposure to x-rays. We used the decrease in P_r as a gauge for fatigue and beam damage during the course of the experiment.

The capacitors were poled immediately before measuring the x-ray reflection intensity. The series of voltages in Figure 1.5 was used to measure P_r and to pole the capacitor. Because the last triangular voltage pulse is negative this sequence leaves the capacitor in the P_{up} state. Pulse trains with the same frequency and opposite polarity were used to switch the polarization to the P_{down} state. These pulses produced maximum amplitudes of ±875 kV/cm, well above the coercive field, which was at most +350 kV/cm for the positive direction.

3.2.4. Spatial average of intensity contrast

The intensities of several Bragg reflections were measured before and after polarization reversal at several photon energies in order to test the predictions of our kinematic scattering model. First, we scanned the incident angle and detector to find the Bragg angle of each reflection. Next, we chose a particular capacitor and put the electrical probe tip on the top electrode. A hysteresis loop was measured to determine if the particular device was functional and had a remnant polarization around $2P_r > 80$ μC/cm^2. The position of the beam on the sample relative to the probe tip and capacitor was determined by rastering the sample underneath the beam and recording the Pb and Pt fluorescence at each position as in Figure 3.4 to image the film, probe tip, and platinum top electrodes. Once the focused beam was on the top electrode, the capacitor was poled and intensity of the reflection was recorded.

Rotations of the atomic planes between mosaic blocks affected the measurement of intensity ratio. The variation of the intensity associated with the position of the beam on the

sample made it difficult to obtain an accurate measurement from a single point on the film. The PZT thin film had a significant mosaic spread of 0.3° in the (002) reflection. The atomic planes within each mosaic block have a slightly different orientation with respect to the substrate atomic planes, meaning the incident angle to satisfy the Bragg condition is slightly different for each mosaic block. To eliminate variations in the intensity from different mosaic blocks, the sample was poled as described in Section 3.2.3 and the intensity was measured at several points in a line. The sample was poled in the opposite direction and the scan was repeated across the sample. An example of this method is shown in Figure 3.5.

The ratio is calculated at each point in the scan so that variations in the orientation or absorption will be canceled out. A region within the scan that was underneath the top electrode and did not contain defects or scratches was defined as the responsive region, shown as the shaded region in Figure 3.5. The final value for the ratio is the average over the responsive portion of the capacitor. We used the standard deviation from the average value to estimate the uncertainty in the measurement.

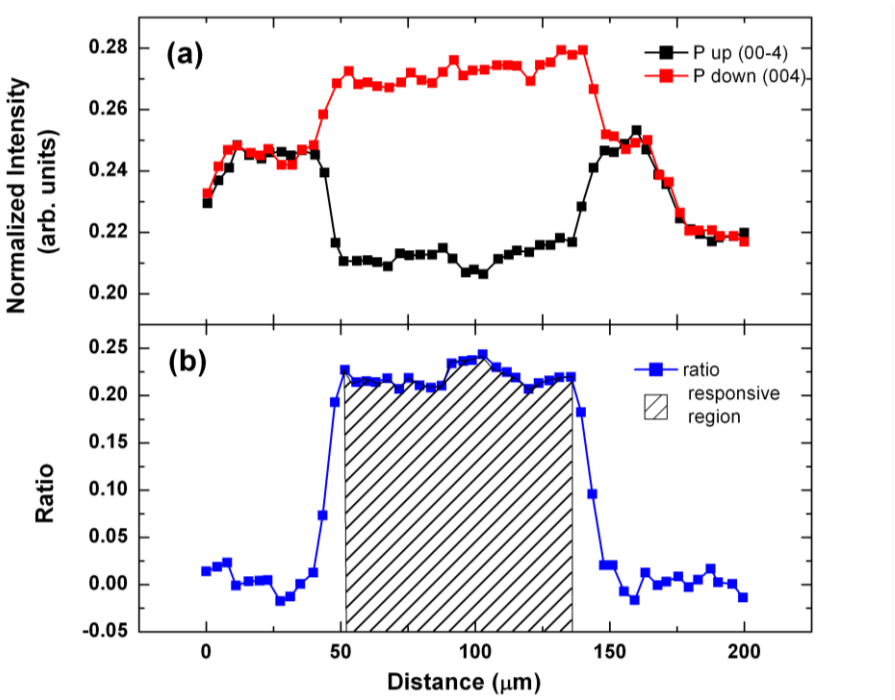

Figure 3.5. Intensity as a function of position across a 100 μm-diameter capacitor in P_{up} (black) or P_{down} (red) states. (b) Intensity ratio as a function of position. The responsive region is shaded.

Although the use of these spatial averages eliminates error from slight changes in orientation with respect to the substrate atomic planes, it does not take other factors into account. We observed that beam damage reduces the intensity of the P_{up} state faster than the P_{down} state. This caused the measured value of the intensity ratio to decrease artificially. Reducing the time per point while scanning the sample and closing the shutter between scans helped to reduce exposure time and total dose in a given area on the sample surface.

3.3. Intensity contrast at 14 keV

The $PbTiO_3$ model predicts changes in the sign of intensity contrast for different (*hkl*) reflections. We tested the $PbTiO_3$ model by measuring the intensity contrast ratio for several

reflections at 14 keV. Line scans across the capacitor for each polarization direction were compared to give the intensity ratio, as in Section 3.2.4. The experimental values for each reflection in Table 3.1 are the average of two to three separate sets of line scans with the standard deviation taken as an estimate of the error.

Reflection	Experimental Ratio	$PbTiO_3$ model
(003)	-0.237 ± 0.022	-0.167
(004)	0.205 ± 0.027	0.160
(104)	-0.345 ± 0.017	-0.145
(105)	0.150 ± 0.024	0.117

Table 3.1. Comparison between predicted and experimental values of the intensity contrast ratio at 14 keV.

The $PbTiO_3$ scattering model predicts the correct sign for the ratio at 14 keV, but it does not accurately predict the amplitude. This suggests that the atomic displacements after polarization reversal can accounted for by the (*-h-k-l*) structure factor, but that the scattering factors and atomic positions in the PZT solid solution need to be taken into account to accurately predict the magnitude of intensity contrast.

3.4. Resonant enhancement of intensity contrast

We measured the energy dependence of the intensity contrast ratio for the {004} reflections above and below the Pb $L\alpha_1$ edge in order to test the energy dependence of the $PbTiO_3$ model. In our $PbTiO_3$ model, the increase in f' and f'' at the absorption edges causes a similar increase in the contrast ratio at absorption edges. At energies below the absorption

edge, our $PbTiO_3$ model predicted that the ratio would be small (less than 0.05) and constant. Above the edge, the $PbTiO_3$ ratio model predicts a larger value of the contrast, up to 0.4 or 0.5, and that this value will gradually decrease for higher x-ray energies.

Measurements were conducted quickly to minimize beam damage to the sample. The remnant polarization and the intensity of Bragg reflections decreased when the beam was left in one spot for an hour or two. Hysteresis loops were taken periodically to measure P_r and avoid taking data from damaged capacitors. For the {004} intensity ratio measurements, we arbitrarily chose a value of the remnant polarization at which we would no longer use the devices. When $2P_r$ dropped below 60 $\mu C/cm^2$ for a particular capacitor, we stopped using it and moved to a new device to continue the measurement. The ratios of the {003} and {004} reflections were measured at energies from 12.4 keV to 14.0 keV are shown in Figure 3.6.

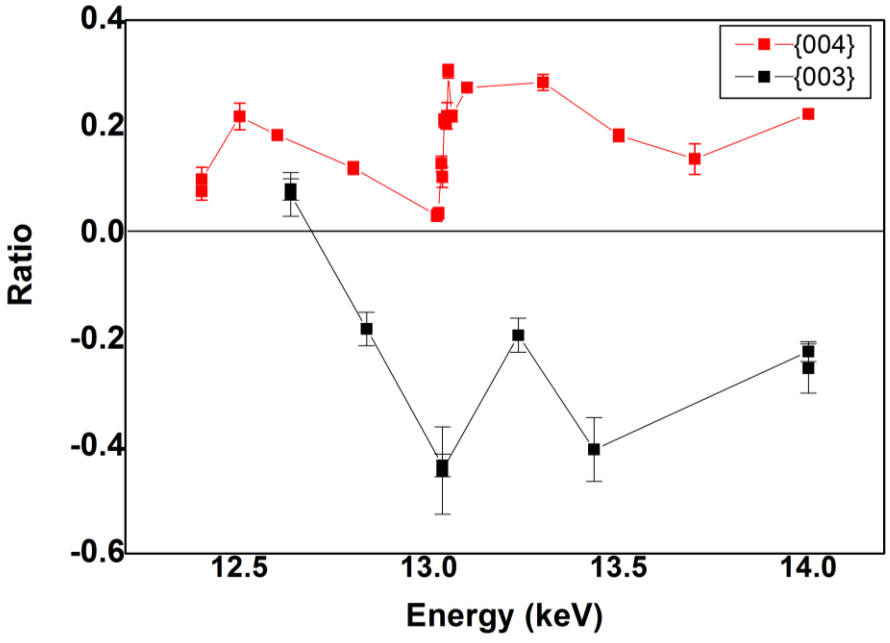

Figure 3.6. Intensity ratio of {003} and {004} PZT reflections versus incident x-ray energy. The sharp increase in the {004} ratio is at the Pb L_3 edge at 13.035 keV.

The sharp increase in the intensity ratio of the {004} reflection at the Pb L_3 edge near 13.035 keV is exactly what we expected, based on the increase in *f "* at the absorption edge. Small oscillations slightly above the edge may be due to the fine structure of the orbitals in the coordinated PZT molecules, as opposed to the elemental Pb atoms considered in the qualitative predictions of Section 3.1.2.

The large fluctuations far from the absorption edge cannot be explained in the same way. For example, the ratio is predicted to be less than ± 0.05 for all reflections between 12.4 and 13.0 keV. There are no absorption edges in any of the other constituent elements (Zr, Ti, and O) anywhere near these energies.

The maximum value of the {003} ratio versus energy was observed at 13.035 keV. However, the rest of the data do not match our qualitative predictions. We know that the error bars do not accurately represent the variation between measurements at the same energy, so that may account for some of the deviation. The qualitative model does not account for the sign of the positive ratio at 12.7 keV. This point was measured twice to confirm the sign of the intensity change at this energy.

Several potential sources of error were eliminated. The mosaic block rotations were averaged out by taking line scans. We do not believe that fatigue is a major cause for uncertainty in the ratio measurements, since the capacitors were switched less than 1,000 times before noticing a decrease in intensity ratio at the same energy. Fatigue typically sets in after 10^5-10^7 switching cycles in similar devices. [17] Artifacts from beam damage were avoided as well. We found that the degradation in P_r occurred before the diffracted intensity

was affected. For example, over the course of three ratio measurements, P_r decreased from 0.93 μC/cm^2 to 0.77 μC/cm^2 while ratio measurements remained the same.

3.5. Refinement of the kinematic scattering model

Structure factor calculations using a $PbTiO_3$ unit cell do not account for some features in the experimental measurements of the intensity contrast ratio. Several models were tested to determine why the observed intensity ratio is larger than the predicted one. In each model, the structure factor for the (*hkl*) and (-*h*-*k*-*l*) reflections is derived and the intensity ratio is calculated.

We carefully selected values of the atomic scattering factors to be sure that they were as accurate as possible. Values of f_0 were taken from a parameterization derived by Waasmaier and Kirfel.[20] The Waasmaier-Kirfel ionic scattering factors are available for a wide variety of ions for values of $\boldsymbol{q}$ = 0-6 Å^{-1}, where $\boldsymbol{q}$ is in units of $\sin(\theta)/\lambda$. Calculated values of $f_0(q)$ were exported from the DABAX function in XOP 2.1[8] in 0.02 Å^{-1} steps for Pb^{2+}, Zr^{4+}, Ti^{4+}, and O^{2-}. They were then imported into Mathematica and linearly interpolated for use in the structure factor calculations.

We used the most accurate values available for the dispersion corrections. Values of f' and f'' were taken from tabulations in Henke *et al.*[11] which are the default values in XOP. They are for the elemental, not the ionized form of the atoms. There are data points 0.1 eV above and below the absorption edge and 500 more data points on a logarithmic scale from 10 to 30,000 eV. Note that XOP outputs *f1* in units of $f' + f_0$ (q = 0).

3.5.1. Model 1: a perfectly disordered alloy

The $PbTiO_3$ model is not accurate enough to describe the scattering from the PZT thin film. An important difference between the $PbTiO_3$ model and the PZT thin films used in the experiment is that the Ti central atom of $PbTiO_3$ is replaced by either a Ti or Zr atom. $Pb(Zr,Ti)O_3$ is a substitutional alloy, so we assumed that PZT is a perfectly disordered alloy and that there is no correlation in the identity of central atoms in neighboring unit cells. The chance of a Zr atom occupying the site is equal to atomic fraction of Zr atoms, 45%; for Ti, 55%.

The structure factors for a PZT random alloy were calculated. In a perfectly disordered alloy, the atomic scattering factor of the central atom can be replaced by the occupancy-weighted average of the scattering factors of the two alloy atoms.[8] With compositions of Zr and Ti given by c_{Zr} and c_{Ti}, respectively, the average scattering factor for the central atom is thus:

$$f_{average} = c_{Zr}f_{Zr} + c_{Ti}f_{Ti} = 0.45f_{Zr} + 0.55f_{Ti}$$

Inserting the $f_{average}$ into a single unit cell of PZT and gives the following expression for structure factor:

$$F(hkl) = f_{Pb} + f_O\left(e^{-2\pi i\,\boldsymbol{q}_{hkl}\cdot\boldsymbol{r}_{O1}} + e^{-2\pi i\,\boldsymbol{q}_{hkl}\cdot\boldsymbol{r}_{O2}} + e^{-2\pi i\,\boldsymbol{q}_{hkl}\cdot\boldsymbol{r}_{O3}}\right) + f_{average}\,e^{-2\pi i\boldsymbol{q}_{hkl}\cdot\boldsymbol{r}_{Zr/Ti}}$$

Atomic positions $\boldsymbol{r_{Pb}}$, $\boldsymbol{r_{O1}}$, $\boldsymbol{r_{O2}}$, $\boldsymbol{r_{O3}}$, and $\boldsymbol{r_{Zr/Ti}}$ were taken from the Reitveld refinement of neutron powder diffraction data from a tetragonal $Pb(Zr_{.48}, Ti_{.52})O_3$ sample in a study conducted by Noheda et *al.*[21] The intensity ratio was calculated using the same expression as

in Section 3.1.2. The ratio for the {003} and {004} reflections as a function of energy is shown below Figure 3.7

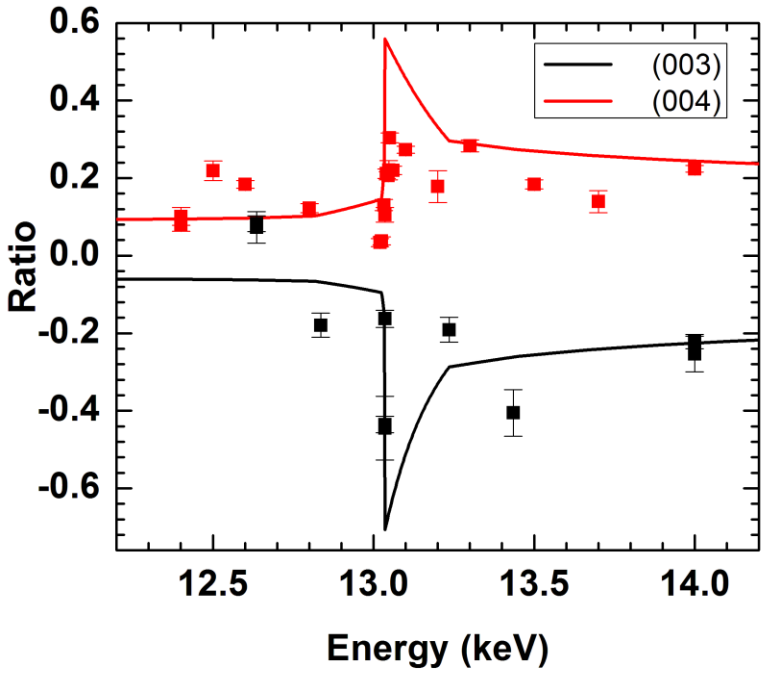

Figure 3.7. Ratio predicted by perfectly disordered alloy model compared with experimental data.

The random alloy model predicts the sign and magnitude better than the $PbTiO_3$ model. Better estimates of f'' were the most significant improvement. However, this model does not explain the positive {003} ratio at 12.7 keV or the large ratios of the {004} below the Pb edge.

3.5.2. Model 2: supercell approximation of a random alloy

Structural refinements of neutron diffraction from PZT powders indicate that Zr and Ti have slightly different positions within the unit cell.[22] The Ti^{4+} ions shift further from the

centrosymmetric position as a function of composition – the closer to the morphotropic phase boundary, the larger the displacement from the center of the unit cell. They list the atomic positions for several compositions of PZT, and chose to use the positions for the $PbZr_{0.4}Ti_{0.6}O_3$ composition.

To model the difference in atomic positions between two atoms, it was no longer possible to use only one unit cell for the structure factor calculations. A supercell consisting of 100 perovskite unit cells was generated to calculate the structure factor. The central atom in each unit cell was randomly chosen such that there was a total of 45 Zr^{4+} and 55 Ti^{4+} ions in the entire supercell. The matching ionic scattering factor (either f_{Zr} or f_{Ti}) was used for the central atom of each unit cell. f_0 was taken from the DABAX tabulations of calculated values from Waasmaier and Kirfel[20] and the dispersion corrections were taken from DABAX tabulations of calculations in Henke *et al.*[11]

The ratio from this Zr/Ti position difference model is not significantly different from the results of the disordered alloy model. Both models share the same trends – low values for the ratio between 10 – 13 keV, a sharp increase at the Pb $L\alpha_1$ absorption edge, and large values which decrease slowly at higher energies. The maximum difference between the two calculated values was at the absorption edge; 0.04 for the {003} and 0.03 for the {004}. Average values for Zr/Ti difference model were 0.02 higher than those calculated by the disordered alloy model. This is around a 1-2% difference between the two models. We conclude that the difference in the Zr and Ti atom's positions within the unit cell is not a significant source of intensity contrast between the two polarization directions. .

3.5.3. Potential future refinements of these models

The models proposed so far provide a reasonable fit for energies at and above the absorption edge. However, neither model can explain the large contrast ratio at energies far from the absorption edge.

One possibility is that the atomic positions of this thin film sample could be drastically different than those in the powder samples used in the structure determination studies cited above. This theory was tested by varying the atomic positions and calculating the contrast ratio. The (002) reflection was selected because the intensity contrast of (00*l*) reflections depends only on f'' and the fractional coordinate w for each atom. I calculated the contrast ratio of the {002} reflection at 10 keV as a function of w for the central atom. This was repeated for the Pb atom as well. Moving the Pb or the Ti/Zr atom along the z axis produces a maximum contrast ratio of 0.15 for the {002} reflections at 10 keV, compared to the experimental value of 0.2 – 0.3. It should be noted that this value for the ratio occurs when the Pb atom is moved 0.726 Å below the basal plane of the unit cell (away from the central atom). A displacement this large seems to be impossible, so we believe that the ratio at low energies is not caused by a change in atomic positions in thin films.

Another possibility is that the dispersion corrections are different for these ions than for non-ionized atoms. It is known that ionization changes the dispersion corrections near absorption edges, but there may be some modifications far from the edge as well. Or there

may be some systematic experimental factor that is more prevalent at lower energies that was not accounted for.

The biggest improvement to the kinematic scattering model was adding the correct atomic scattering factors. The perfectly disordered alloy model with dispersion corrections for Pb^{2+}, Zr^{4+}, Ti^{4+}, and O^{2-} accurately predicted the intensity ratio near the Pb L_3 edge. The differences in atomic positions in $PbTiO_3$ and PZT played a more subtle role. We learned that the differences between the PZT structural refinement in Noheda *et al.* and that in Frantti *et al.* did not have a large effect on the intensity ratio.[5,22] In fact, even impractically large displacements of Pb and Zr/Ti ions were not sufficient to explain the observed ratios of the {002} or {004} at energies below the Pb edge.

3.6. Conclusion

In ferroelectric materials, the intensity of a Bragg reflection depends on the polarization direction. The atomic displacement associated with the polarization changes the structure factor. The change in intensity upon switching the polarization was calculated by computing the structure factor for the (*hkl*) and (-*h*-*k*-*l*) reflections. The intensity contrast induced by polarization switching was measured experimentally using x-ray microdiffraction for several reflections as a function of energy. Predicted values were compared to the experimental measurements in order to refine the kinematic scattering model.

The precise atomic positions within the PZT unit cell were less important in predicting the intensity contrast accurately than using the correct atomic scattering factors. The biggest

improvement from the $PbTiO_3$ model was achieved by approximating the scattering factor of the central Zr/Ti atom as a compositionally weighted average of the Zr and Ti scattering factors. This approach was most accurate near absorption edges, where the imaginary component of the dispersion correction is largest and the change in intensity is most noticeable. However, at energies far from an absorption edge other sources of contrast become more prevalent in PZT. Artificially displacing the Pb and Zr/Ti atoms could not account for the large intensity contrast at energies well below the Pb L_3 edge. We suggest that the dispersion corrections of the cations in PZT are different than those tabulated in Waasmaier and Kirfel.[20]

3.7. Chapter 3 references

[1] J.Y. Jo, P. Chen, R.J. Sichel, S.-H. Baek, R.T. Smith, N. Balke, S.V. Kalinin, M.V. Holt, J. Maser, K. Evans-Lutterodt, C.-B. Eom, and P.G. Evans, *"Structural Consequences of Ferroelectric Nanolithography," Nano Lett.*, Article ASAP, (2011). doi**:** 10.1021/nl2009873

[2] S. J. van Reeuwijk, K. Karakaya, H. Graafsma and S. Harkema, *"Polarization switching in $BaTiO_3$ thin films measured by X-ray diffraction exploiting anomalous dispersion"* J. Appl. Cryst. 37, 193 (2004).

[3] D.-H. Do, "*Investigation Of Ferroelectricity And Piezoelectricity In Ferroelectric Thin Film Capacitors Using Synchrotron X-Ray Microdiffraction,"* PhD thesis, University of Wisconsin-Madison (2006).

[4] D.-H. Do, P. G. Evans, E. D. Isaacs, D. M. Kim, C.-B. Eom and E. M. Dufresne, "*Structural visualization of polarization fatigue in epitaxial ferroelectric oxide devices*," Nature Mater. **3**, 365 (2004).

[5] B. Noheda, D. E. Cox, G. Shirane, J. A. Gonzalo, L. E. Cross, and S. E. Park, *"A monoclinic ferroelectric phase in the $Pb(Zr_{1-x}Ti_x)O_3$ solid solution,"* Appl. Phys. Lett. **74,** 2059 (1999).

[6] R. D. Shannon, "*Revised effective ionic radii and systematic studies of interatomic distances in halides and chalcogenides*", Acta Cryst. A **32**, 751 (1976).

[7] S. Nishikawa and K. Matsukawa, *"Hemihedry of Zincblende and X-ray Reflexion,"* Proc. Imp. Acad. Japan, **4**, 96 (1928).

[8] M. Sanchez del Rio and R. J. Dejus, *"Status of XOP: an x-ray optics software toolkit"* SPIE Proceedings **3448**, 340 (1998).

[9] R. W. G. Wyckoff, *Crystal Structures*. Vol. 2, p. 401, (John Wiley & Sons, New York, 1963).

[10] J. Als-Nielsen and D. McMorrow, *Elements of Modern X-ray Physics*, (John Wiley & Sons, West Sussex, England, 2001).

[11] B.L. Henke, E.M. Gullikson, and J.C. Davis, "*X-ray interactions: photoabsorption, scattering, transmission, and reflection at E=50-30000 eV, Z=1-92*," Atomic Data and Nuclear Data Tables **54,** 181 (1993).

[12] B. Jaffe, W. R. Cook, and H. Jaffe, *Piezoelectric Ceramics*, (Academic Press, London and New York, 1971).

[13] C. B. Eom, R. B. Van Dover, J. M. Phillips, D. J. Werder, J. H. Marshall, C. H. Chen, R. J. Cava, and R. M. Fleming, and D. K. Fork, *"Fabrication and properties of epitaxial ferroelectric heterostructures with ($SrRuO_3$) isotropic metallic oxide electrodes,"* Appl. Phys. Lett. **63**, 2570 (1993).

[14] J. M. Ablett, L. Berman, C. Kao, G. Rakowsky, D. Lynch. *"Small-Gap Insertion-Device Development at the National Synchrotron Light Source - Performance of the New X13 Mini-Gap Undulator,"* J. Synch. Radiation **11**, 129 (2004).

[15] J. M. Ablett, C. C. Kao and A. Lunt, *"The design and performance of an x-ray micro-focusing system using differentially deposited elliptical mirrors at the National Synchrotron Light Source,"* Review of Scientific Instruments **73**, 3464 (2002).

[16] J. A. Bearden, "*X-Ray Wavelengths*", Rev. Mod. Phys. **39**, 78 (1967). Information from the X-ray Data Booklet can be found online at http://xdb.lbl.gov/ .

[17] K. Rabe, C. H. Ahn, J.-M. Triscone (Eds.), *Physics of Ferroelectrics*, (Springer-Verlag, Berlin, Germany, 2007).

[18]C. M. Foster, G.-R. Bai, R. Csencsits, J. Vetrone, R. Jammy, L. A. Wills, E. Carr, and J. Amano,*"Single-crystal $Pb(Zr_xTi_{1-x})O_3$ thin films prepared by metal-organic chemical vapor deposition: Systematic compositional variation of electronic and optical properties,"* J. Appl. Phys. **81,** 2349 (1997).

[19] T. J. Zhua, L. Lub, X. B. Zhao, Z. G. Jia, J. Mac, *"Epitaxial growth and ferroelectric properties of $Pb(Zr_{0.52}Ti_{0.48})O_3/SrRuO_3$ heterostructures on exact $SrTiO_3$ (001) substrates,"* J. Cryst. Growth **291**, 385 (2006).

[20] Waasmaier and Kirfel, "*New Analytical Scattering-Factor Functions for Free Atoms and Ions*,"Acta. Cryst. A **51,** 416 (1995).

[21] B. Noheda, J. A. Gonzalo, L. E. Cross, S. E. Park, D. E. Cox, and G. Shirane, "*Tetragonal-to-monoclinic phase transition in a ferroelectric perovskite: The structure of $PbZr_{0.52}Ti_{0.48}O_3$*" Phys. Rev. B **61**, 8687 (2000).

[22] J. Frantti, S. Ivanov, S. Eriksson, H. Rundlof, V. Lantto, J. Lappalainen, and M. Kakihana, "*Neutron diffraction and bond-valence calculation studies of $Pb(Zr_xTi_{1-x})O_3$ ceramics,"* Phys. Rev. B **66,** 064108 (2002).

Chapter 4. Piezoelectric Response of $BiFeO_3$ (001) Thin Films

4.1. Introduction

All ferroelectric materials are piezoelectric, including $BiFeO_3$. Piezoelectric materials change size and shape when an electric field is applied. Conversely, when a piezoelectric material is compressed or stretched it develops a polarization proportional to the stress. Since materials may expand in one direction and contract in another, the piezoelectric coefficients are described using tensor notation. The piezoelectric response of $BiFeO_3$ is important for both electromechanical applications and for the potential control of its magnetism using electric fields.

There are several reasons why $BiFeO_3$ has attracted so much attention in recent years. For one, the piezoelectric properties of $BiFeO_3$ could be used in electromechanical actuators and transducers. Also, physicists have taken an interest in $BiFeO_3$ thin films because they provide an attractive system for examining several effects of electromechanical coupling. Evidence for strain-driven morphotropic phase transformations have been found in highly strained films of $BiFeO_3$.[1, 2] Studies of $BiFeO_3$ and other materials have also revealed subtle ferroelectric effects such as bond lengthening under electric field and rotations of the material's polarization vector.[3,4] Additionally, epitaxial strain has been shown to change the piezoelectric response and ferroelectric polarization.[5]

In addition to its usefulness in the development of materials for purely mechanical applications, determining the piezoelectric response of $BiFeO_3$ is crucial to its eventual use in

magnetoelectric devices. When the ferroelectric polarization state and antiferromagnetic ordering are dependent on one another in a material, the link between order parameters is known as multiferroic coupling.[6] It is important to understand the multiferroic coupling in $BiFeO_3$ because the Fe-O-Fe bonds which modify magnetic ordering are affected by changes in the lattice constants.[7] The electromechanical coupling is of particular interest for $BiFeO_3$ because it is related to the multiferroic properties. Magnetic ordering in transition metal perovskites is mediated by the superexchange interaction between transition metal ions via a polarization of the atomic orbitals of the oxygen ions.[8] In $BiFeO_3$, calculations using density functional theory suggest that the magnetic interaction is sensitive to the tilt and rotation of the FeO_6 oxygen octahedra.[9] When $BiFeO_3$ is subjected to an electric field, piezoelectric strain can modify the magnetic ordering by distorting the oxygen octahedra. The details of the structural changes induced by applied electric fields must be studied before we can fully understand and manipulate the magnetism.

Time-resolved synchrotron x-ray microdiffraction was used to determine the piezoelectric coefficients by measuring the strain developed when an electric field is applied to the sample. These thin films have multiple structural variants with differing crystallographic orientations (see Chapter 2). Since the piezoelectric response is largest along the pseudocubic [111] direction, the structural variants could each have different strains under the same electric field. We find that the strain along the out-of-plane direction is the same for all variants. The in-plane piezoelectric coefficients vary unpredictably and are not correlated with the crystallographic orientation of $BiFeO_3$.

4.1.1. Piezoelectric tensor

Piezoelectricity results in two important effects. In the direct piezoelectric effect, a stress applied to the material results in an internal electric field. The resulting voltage can be measured and used to determine the electric field. The direct piezoelectric coefficient *e* is the constant of proportionality between the magnitude of the strain generated in the material by the applied stress and the electric field. In the converse piezoelectric effect, an applied electric field results in strain. The converse piezoelectric coefficient *d* relates the applied electric field and the strain. These experiments focused on the converse piezoelectric effect in order to determine the effects of electric field on the structure and bond angles.

In the limit in which the piezoelectric strain is exactly proportional applied electric field, the strain tensor and electric field are related by $\varepsilon_{jk} = d_{ijk} \cdot E_i$, where ε is the strain, d is the piezoelectric coefficient, and E is the applied electric field.[10] Piezoelectricity is a tensor property so that applying an electric field along one direction can produce strains and shears along orthogonal directions as well. The units of the converse piezoelectric coefficient are distance divided by potential difference. Values of the piezoelectric coefficient are often given in pm/V. The three-index notation in the equation above can be condensed to a two-index notation, d_{ij}. The first index i refers to the electric field direction in the conventional manner where 1,2, and 3 refer to the x, y, and z directions, respectively. The second index j refers to elements in the strain tensor using Voigt notation.[10] The tensor of converse piezoelectric coefficients d_{ij} relates the piezoelectric strain ε_j to the electric field E_i:

$$\begin{bmatrix} \varepsilon_1 & \varepsilon_6 & \varepsilon_5 \\ \varepsilon_6 & \varepsilon_2 & \varepsilon_4 \\ \varepsilon_5 & \varepsilon_4 & \varepsilon_3 \end{bmatrix} = \begin{bmatrix} d_{11} & d_{12} & d_{13} & d_{14} & d_{15} & d_{16} \\ d_{21} & d_{22} & d_{23} & d_{24} & d_{25} & d_{26} \\ d_{31} & d_{32} & d_{33} & d_{34} & d_{35} & d_{36} \end{bmatrix} \begin{bmatrix} E_1 \\ E_2 \\ E_3 \end{bmatrix}.$$

We use the pseudocubic notation for the $BiFeO_3$ piezoelectric tensor and x-ray reflections in order to emphasize the epitaxial relationship between film and substrate. The rhombohedral symmetry of $BiFeO_3$ is not apparent from this notation, which has the side effect of complicating the expression for the piezoelectric tensor. When the piezoelectric tensor is projected onto a basis parallel to high symmetry directions such as the [100], [010], and [001] directions of a tetragonal material, most of the terms are equal to zero while many of the remaining coefficients are identical.[10] However, simplifications that can be made to the piezoelectric tensor d_{ij} based on symmetry relationships a tetragonal system are not possible in $BiFeO_3$ thin films, for two reasons. First the axes of the rhombohedral coordinate system are not parallel to the pseudocubic axes used to define the piezoelectric tensor coordinate system. More importantly, the film is under anisotropic epitaxial strain, reducing the symmetry in the plane of the film. In this chapter we use the pseudocubic notation and the pseudocubic coordinate system to define strain, electric field direction, and the piezoelectric coefficient tensor and we make no symmetry-based simplifications to the piezoelectric tensor.

A second definition of the piezoelectric coefficients is widely used in conjunction with polycrystalline piezoelectric ceramics. The notation and units are identical to the ones described above, often leading to confusion. In this so-called engineering notation, the piezoelectric coefficients are defined so that the *z* direction corresponding to subscript 3, is

defined to be in the direction of the applied electric field. The expansion along the field direction is thus determined by the piezoelectric coefficient d_{33} in the engineering notation. The symmetry of the piezoelectric tensor is also different between the two definitions. In the crystallographic definition the piezoelectric tensor has the symmetry of the crystallographic unit cell. In the engineering definition, the tensor has the same symmetry as the overall shape of the piezoelectric solid, which can be quite different from the crystallographic symmetry.

We chose a coordinate system with z parallel to the out-of-plane direction. We chose this system in order to make z parallel to the electric field applied across the electrodes above and beneath the film. For (001)-oriented thin films the electric field nearly parallel to the pseudocubic **c** axis of the film. In this case E_1 and E_2 are zero and only E_3 is non-zero. The piezoelectric coefficients which determine the tensile or compressive strain are d_{31}, d_{32}, and d_{33}, and changes in shape of the unit cell (shear strains) are determined by d_{34}, d_{35}, and d_{36}.

Measuring piezoelectric strain in thin films can be difficult. In bulk materials the piezoelectricity can be measured using interferometry, in resonators, or by observing the mechanical distortion using a profilometer. In thin films, piezoelectricity must be observed using a different set of techniques. In wafer-bending measurements of piezoelectricity, the change in the electrical polarization of the film is measured when the substrate is bent using a pressure cell, providing the direct piezoelectric coefficient.[11] The drawback of the wafer-bending approach is that it requires knowledge of precise values of the Young's modulus and the Poisson ratios to give accurate results. These values are note always available, especially for new materials. Another approach is to use focused ion beam milling or selective etching to create a bridge structure or cantilever into the film by removing a section of the underlying

substrate.[12] A DC voltage is applied and the deflection of the bridge or elongation of the cantilever is measured optically, enabling the experimenter to calculate d_{31}. Potential problems with this method are that the film can be damaged during the substrate removal process and that DC electric fields must be applied, so the field magnitude must be kept small to avoid dielectric breakdown.

Time-resolved microdiffraction probes both the out of plane and the in-plane piezoelectric response while avoiding the difficulties of other techniques. The strains ε_1, ε_2, and ε_3, can be determined from changes in the pseudocubic *a*, *b*, and *c* lattice constants, respectively. The experiments in this chapter measure piezoelectric strain in $BiFeO_3$ thin films by detecting changes in the lattice constants while an electric field is applied. We find that d_{33} is constant for the entire film, but the in-plane piezoelectric response varies from place to place in the sample.

4.2. Experimental methods

4.2.1. Experimental setup

The sample used for these measurements was the same as for the experiments described in Chapter 2. The layer structure consisted of a 400 nm $BiFeO_3$ thin film on a $SrRuO_3$ thin film bottom electrode grown on a (001) $SrTiO_3$ substrate miscut by 3.1° along the [010] direction. The sample had Pt top electrodes of varying diameters grown by sputter deposition through a shadow mask on top of the $BiFeO_3$ surface. The top electrodes defined

capacitor structures, which allowed an electric field to be applied across the thickness of the film.

The x-ray diffraction experiments were conducted at the Advanced Photon Source. X-rays at photon energies of either 11.5 or 10 keV were selected by a Si (111) double-crystal monochromator. The incident x-ray beam was focused using a Fresnel zone plate as described in Section 1.7.3.2. The diffraction volume probes only material that is subjected to the electric field and does not include any signal from the regions outside the electrodes. The experiments were done in two segments. Measurements of the piezoelectricity along the out-of-plane direction in high electric fields were done at Sector 7-ID-C using the nanosecond-scale time resolved technique explained in Section 1.7.4.2. For these high-field piezoelectric measurements, the incident beam had a photon energy of 10 keV, a spot size of 130 nm at full width half maximum, and the sample-to-detector distance was 285 mm. Measurements of the in-plane piezoelectricity were conducted at Sector 2-ID-D using the millisecond-scale time resolved technique in Section 1.7.4.1 with a photon energy of 11.5 keV, x-ray spot size of 275 nm, and sample to detector distance of 310 mm. Both experiments used an APD to detect scattered x-rays. The detector angular resolution was determined by the size of slits placed directly in front of the detector.

The experimental procedure was similar for both measurements. In both cases, we first found the Bragg reflections for each component of the sample near the $SrTiO_3$ (002) reflection to determine the out-of-plane lattice constant of the $BiFeO_3$. To do this, the sample and detector were rotated to the angles predicted for the (002) Bragg reflections. The incident angle, θ, diffracted angle, 2θ, and sample tilt angle, χ, were varied to find the maximum of the

$BiFeO_3$ (002) reflection. These angles are shown schematically in Figure 1.7. A θ-2θ scan through the series of reflections near the $SrTiO_3$ (002) reflections is shown in Figure 4.1. The $SrTiO_3$ (002) reflection was used to calibrate the observed values of θ and 2θ, based on its reported bulk lattice constant of 3.905 Å.

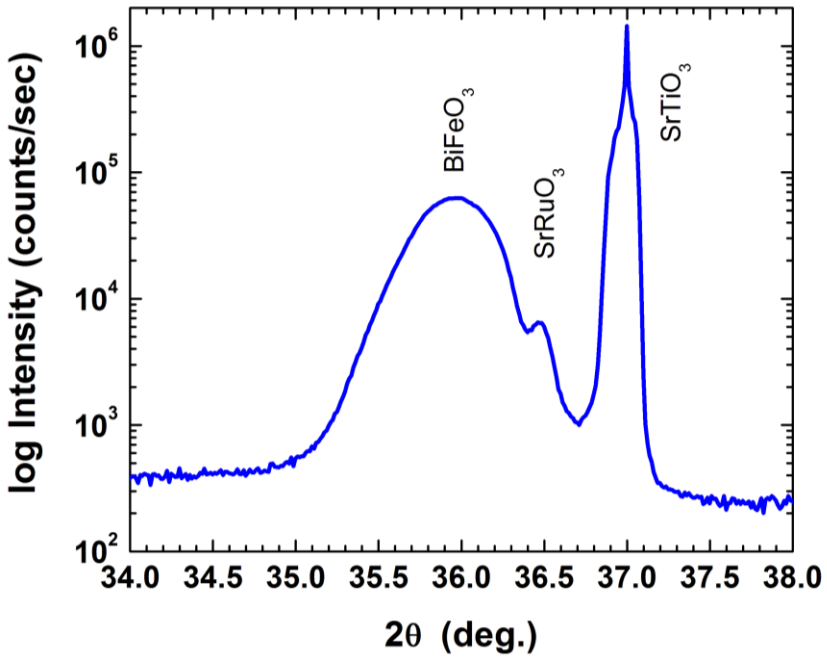

Figure 4.1. θ-2θ scan of the $SrRuO_3$ (220), $BiFeO_3$ (002), and $SrTiO_3$ (002) reflections with a photon energy of 10 keV.

The lattice constants of the films were determined using the angular positions of the Bragg reflections in Figure 4.1. From these measurements we found that $BiFeO_3$ had a lattice constant c_{BFO} = 4.01 Å. This is slightly larger than the bulk pseudocubic lattice constant of $BiFeO_3$, 3.96 Å.[13] The $SrRuO_3$ has a pseudocubic lattice constant c_{SRO} = 3.96 Å. The width of the $BiFeO_3$ peak is caused by the range of strain states and orientations within the film due to partial relaxation described in Chapter 2.

4.2.2. Time resolved x-ray diffraction

The piezoelectric strain was measured by simultaneously applying an electric field and measuring the time resolved x-ray diffraction. An electrical probe tip contacted the top electrode of a capacitor structure. During the x-ray experiments we acquired a polarization-electric field hysteresis loop to be sure that the particular device was switchable and that it had a remnant polarization similar to the expected value. Maps of diffracted intensity over the sample surface were used to place the focused beam and probe tip on the same capacitor. A similar procedure for bringing the beam and the tip to the same position is described in Section 3.2. In order to minimize structural artifacts arising from beam damage the sample was occasionally moved in steps of several microns to bring the x-ray spot to a region of the $BiFeO_3$ film that had not yet been exposed to the beam.

The time-resolved diffraction pattern was recorded while an electric field was applied to the film. The electric field was applied while the diffracted intensity as a function of time was recorded at each point in a scan across a Bragg reflection. During the high-electric-field scans, the sample and detector were rotated to the first point in the scan. The voltage on the probe tip was provided by a fast-risetime pulse generator (Picosecond Pulse Generator 2600C). Square-wave pulses with a duration of 25 ns width and voltage amplitudes ranging between +45 V and -45 V were applied to the sample. Prior to time-resolved diffraction measurements, we applied several 25 ns pulses with amplitudes above the coercive field. These pulses switched the polarization direction parallel to the applied field. A series of 5,000 pulses were applied at a repetition rate of 3 kHz. The x-ray photons scattered during the pulses were selected from the stream of x-ray photons arriving at times outside the pulses,

as in Section 1.7.4.2. The intensity of the x-ray reflection was determined by summing the number of diffracted photons using one channel of a scaler (Joerger, Inc.). The intensity measurement was repeated in steps of 0.8 ns, starting 5 ns before the rising edge of the voltage pulse and ending 40 ns later. The entire process was then repeated for each angle of a θ-2θ scan. The intensities acquired in this way were then plotted to show the evolution of the intensity near the $BiFeO_3$ (002) Bragg reflection as a function of time.

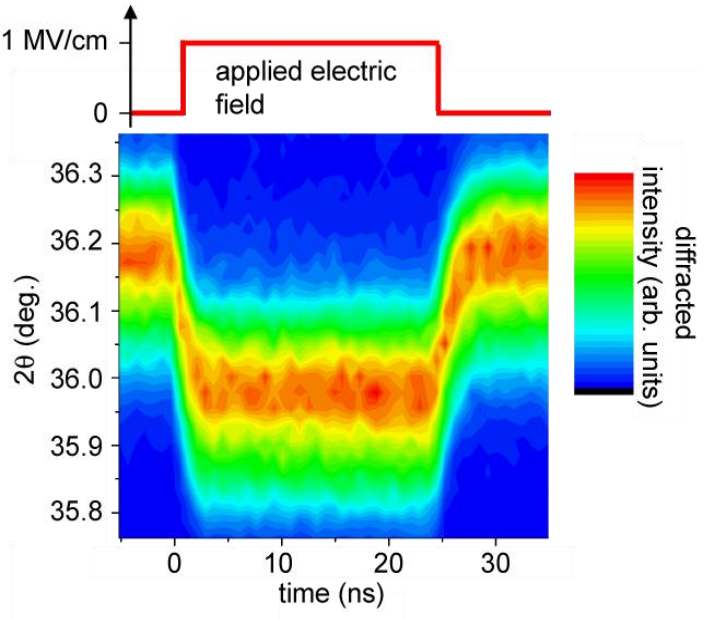

Figure 4.2. Time resolved θ-2θ scan of the $BiFeO_3$ (002) reflection during a 25 ns voltage pulse. The x-ray photon energy was 10 keV.

Figure 4.2 is the intensity versus time at the (002) $BiFeO_3$ Bragg reflection during a voltage pulse corresponding to E=1.04 MV/cm. The field applied to the capacitor is shown in the upper panel of the figure. The lower panel shows the diffracted intensity as a function of time. The vertical axis is the detector angle (2θ) in a θ-2θ scan. The horizontal axis indicates time, where 0 on the time axis corresponds to the beginning of the rising edge of the voltage

pulse. Each vertical line is a θ-2θ scan at one point in time. The center of the (002) reflection shifts to a lower angle once the field is applied.

The structural signature of the capacitor charging time can be seen at the beginning and end of the voltage pulse. The structural transient apparent just after the beginning of the voltage pulse in Figure 4.2 has an RC time constant of 3.1 ns. The rise time of the pulse generator is far shorter than this, approximately 300 ps. We suspect that the rise time of the Bragg reflection is caused by the time required to charge the capacitor and that the rise time thus depends on the time constant for charging the device rather than on a fundamental physical time scale. We measured the piezoelectric strain using the angular position of the (002) reflection several RC time constants after the beginning of the electrical pulse.

4.3. Measurement of out-of-plane piezoelectric coefficient d_{33}

The piezoelectric coefficient in the out-of-plane direction was measured from the shift in angle of the $BiFeO_3$ (002) reflection. The strain induced by an electric field along the out-of-plane direction is defined as ε_3 in our notation. Using the Bragg equation for interplanar spacing we find that the strain is given by:

$$\varepsilon_3 = \frac{\sin\theta_0}{\sin\theta} - 1$$

Here the subscript 0 indicates the initial condition without electric field. Fitting a Gaussian function to the zero-electric-field $BiFeO_3$ (002) reflections in Figure 4.2 gives $\theta_0 = 35.978°$.

The field-induced shift of the (002) was measured for many strengths of electric field. The (002) reflections for several electric fields are shown above in Figure 4.3. The 1.04

MV/cm θ-2θ scan was taken from the data in Figure 4.2. The 478 kV/cm line was taken from θ-2θ scans during the middle of similar voltage pulses with half the amplitude, 15 ns after the beginning of the pulse. We chose to measure at a single point in time instead of scanning in order to reduce the total number of pulses applied to the device. The zero-field line was taken during an identical scan without electric field as a baseline for comparison.

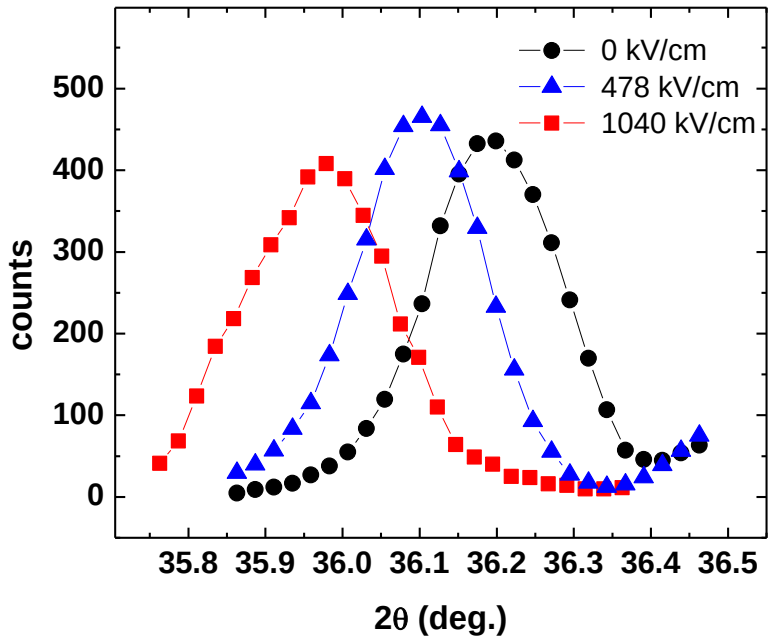

Figure 4.3. θ-2θ scans across the $BiFeO_3$ (002) reflection at several electric fields.

The field we applied during the data acquisition of Figures 4.2 and 4.3 was directed along the *z* direction only, so that $\varepsilon_3 = d_{33}E_3$. The piezoelectric coefficient d_{33} was calculated from a least-squares fit of a line to the strain as a function of electric field, shown below in Figure 4.4. No hysteresis is observed in the piezoelectric strain because the polarization of

the film was switched to be parallel to the applied field before the piezoelectric strain was measured.

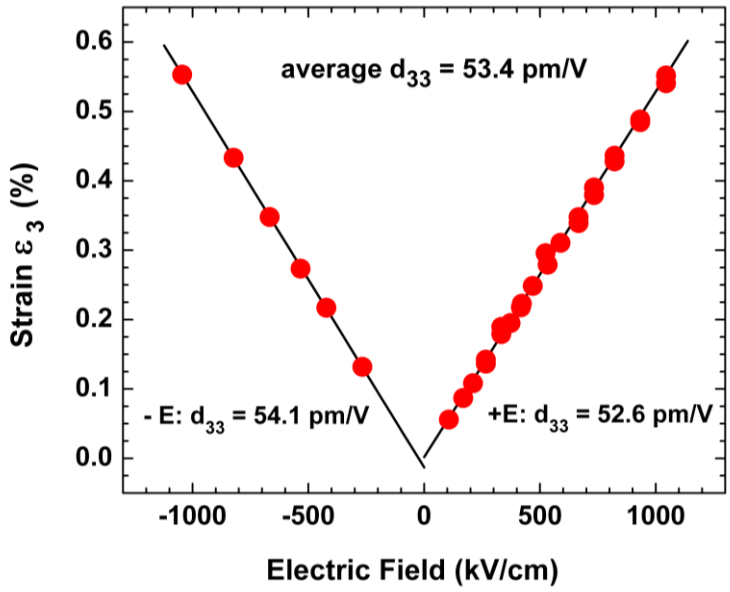

Figure 4.4. Strain ε_3 versus applied electric field for positive and negative polarity fields.

The piezoelectric coefficient is determined from the slopes of the linear fits to the strain versus *E* in Figure 4.4. The piezoelectric strain is proportional to the applied field for both signs of the applied electric field, as expected at these magnitudes of electric field.[14] The value of d_{33} determined from Figure 4.4 is 53 pm/V. This coefficient is similar to values found by piezoresponse force microscopy (PFM), which range from 50 to 60 pm/V.[15]

Agreement between PFM and x-ray diffraction measurements of d_{33} indicate that the film is strained homogenously. This is because PFM experiments measure the displacement of the film underneath a conductive tip, whereas diffraction measures the average lattice constant. The width of an x-ray reflection in θ-2θ is a measure of the variation in interplanar spacing within the diffraction volume. An increase in the width of the reflection would

indicate that the film was not strained homogeneously. The peak width of the (002) reflection is constant with *E* below 1 MV/cm. This means that the entire film has the same piezoelectric strain rather than having regions with different piezoelectric coefficients with an average value of 53 pm/V.

4.4. In-plane piezoelectric response and d_{31}

The piezoelectric tensor includes components that lead to distortions of the crystal in directions that are orthogonal to the applied field. In thin films, elastic constraints due to the substrate and to the shape of the thin film make the piezoelectric distortion in this direction difficult to predict. We predict that a piezoelectric strain in the in-plane direction, i.e. in the plane of the surface, will only be possible if the film is not coherent and epitaxial. In an epitaxial film with no defects, the film is clamped by the substrate and the film is prevented from expanding or contracting along the in-plane direction.[16] Clamping effects force the effective d_{31} to be zero in thin films that cannot change their lateral dimensions or relax elastically in some other way.[17]

We measured the in-plane piezoelectric response using changes in the (103) $BiFeO_3$ reflection while the sample was subjected to an electric field. First, a reciprocal space map of the (103) $BiFeO_3$ reflections was acquired without an electric field in order to identify the structural variants present in the film. The structural variants are signatures of polarization domains, as described in Chapter 2. Then reciprocal space maps are taken as a function of time while electric field is applied. The change in angle of each reflection is used to calculate

the strain for each structural variant. Finally, the linear dependence of strain on electric field was measured to obtain the piezoelectric coefficients for each structural variant.

4.4.1. Multiple (103) reflections of structural variants

The zero-field $BiFeO_3$ (103) reflections were measured to identify the structural variants present in the film and to determine the strain state before applying electric field. The in-plane strain can be measured using an x-ray reflection with a wavevector that has a component in the plane of the surface of the sample. For a pseudocubic thin film grown with a (001) orientation this would correspond to any reflection in which the Miller index *h* or *k* is not zero. The change in interplanar spacing due to piezoelectricity can be found by applying the Bragg equation to the magnitude of the wavevector of the reflection. Decomposing the distortion into in- and out-of-plane components of strain is more difficult. .

We chose the (103) x-ray reflection for studies of the in-plane piezoelectricity for several reasons. First, the (103) reflection is geometrically accessible using x-rays at the photon energies that we could focus onto the sample using the Fresnel zone plate. Second, the x-rays incident on the sample in studies of the (103) reflection have a large incident angle of 43.8° at 11.5 keV. This allows us to have a small footprint of the focused beam on the sample, which is useful in studying the piezoelectricity of individual grains or mosaic blocks.

A structural study of the $BiFeO_3$ thin film reveals that it is not completely pseudomorphic. The distribution of intensity in reciprocal space near the (103) x-ray reflection of $BiFeO_3$ is shown in Figure 4.5, in which reflections from $BiFeO_3$ and $SrRuO_3$ appear. The presence of multiple reflections from $BiFeO_3$ indicates that more than one

polarization domain is present within the volume illuminated by the focused x-ray beam. A similar structural issue was discussed in Section 2. Since the diffraction data in Figure 4.5 is a two-dimensional scan, rather than the three-dimensional reconstruction of reciprocal space discussed in Chapter 2, we lack the necessary information in the $\boldsymbol{q_y}$ direction required for identifying polarization direction. We can, however, determine that there are four $BiFeO_3$ variants in the volume illuminated by the focused x-ray beam.

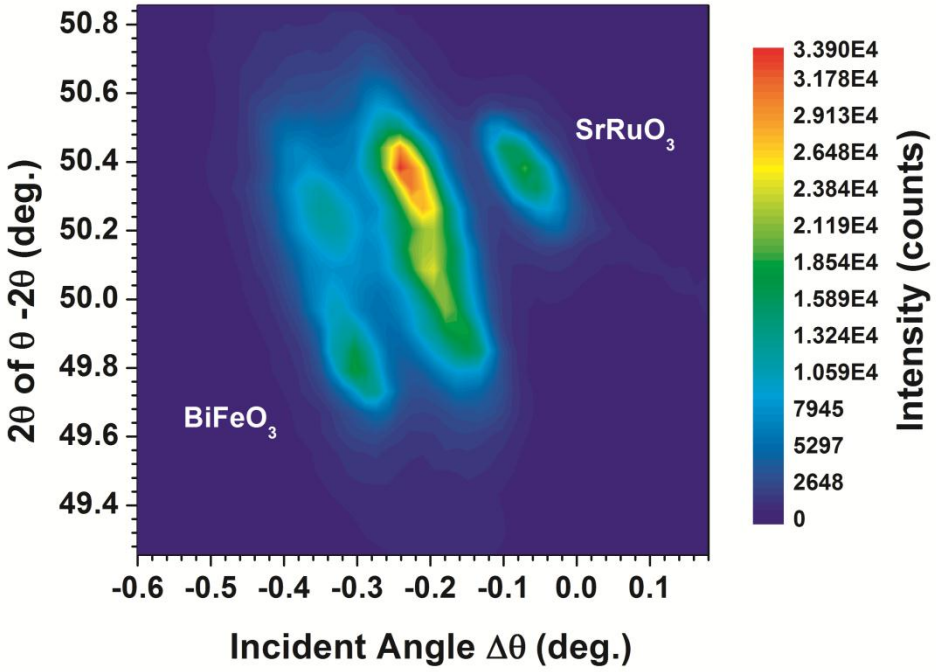

Figure 4.5. Reciprocal space map of the pseudocubic (103) reflections from $BiFeO_3$ and $SrRuO_3$. There are four $BiFeO_3$ peaks, each from a different structural domain.

Calculating the in-plane strain accurately is very difficult because of uncertainty in the crystallographic orientation. In an epitaxial film, the $\boldsymbol{q_x}$ and $\boldsymbol{q_z}$ components of $\boldsymbol{q(E)}$ can be used to determine the projections of the piezoelectric strain onto the in-plane [100] direction and the out-of-plane [001] direction, respectively. In a relaxed film, each mosaic block has a

slightly different orientation with respect to the substrate, and the (103) reflection will be rotated about in reciprocal space. The coordinate axes, and therefore the projections of $\boldsymbol{q}$ onto $\boldsymbol{q_x}$ and $\boldsymbol{q_z}$ are different for each mosaic block. The mosaic block structure of the $BiFeO_3$ is such that the orientation of the individual blocks varies randomly on the 1 μm scale. Changes in $\boldsymbol{q_x}$ can thus in principle arise from either changes in the lattice constant or in the orientation of the blocks.

One solution to this problem is to measure more than one reflection from the same domain. By measuring multiple reflections we would be able to determine both the orientation of the mosaic block and its lattice constants. This is not feasible because it requires rotating the sample in order to reach the Bragg condition of the next reflection. After rotating to a different incident angle, the focused beam hits a different spot on the sample because the sample and focused beam are not exactly in the center of rotation of the goniometer. Previous attempts to re-find the same spot on the sample after rotating between the (002) and (103) reflections were not successful, even when we used landmarks visible to the diffracted intensity maps, such as the edge of an electrode. The best registry between (002) and (103) intensity maps we achieved was on the order of several microns, which is insufficient considering the mosaic block size of 1 μm.

4.4.2. Variations of the in-plane piezoelectricity

We observe that the in-plane piezoelectric response is not zero as expected for an epitaxial thin film. For a perfectly clamped film in which the in-plane lattice constants are fixed to that of the substrate, there can be no piezoelectric contraction along the in-plane direction. We thus expect d_{31} to be zero for a clamped film. In the opposite, bulk-like case,

in which there is no mechanical constraint imposed by the substrate we expect d_{31} to be non-zero, as in bulk ceramics.[18] We know that the 400 nm $BiFeO_3$ film is partially relaxed, so we expect d_{31} to be non-zero as in polycrystalline piezoelectric materials.

A reciprocal space map of several $BiFeO_3$ pseudocubic {103} reflections was measured as a function of time to determine the piezoelectric strain in each structural variant. The time dependent diffraction pattern was obtained using the millisecond-scale method described in Chapter 1.7.4.1. The result was a series of reciprocal space maps, each taken with a different electric field. Within one reciprocal space map, the four $BiFeO_3$ reflections were fit to Gaussian functions to determine the angle at the center of the peak. These angles were used to calculate the positions in reciprocal space of the $BiFeO_3$ reflections. This process was repeated for each reciprocal space map to get the peak positions as a function of electric field.

The piezoelectric response was visualized by plotting the $BiFeO_3$ pseudocubic {103} positions in reciprocal space at several electric fields. Figure 4.6 shows a plot of the reciprocal space positions of the $BiFeO_3$ pseudocubic {103} reflections. The evolution of these reflections in an applied electric field is shown as a trail of points in Figure 4.6. Arrows indicate the direction of motion with increasing E, ranging from 0 to 250 kV. The distortion evident in Figure 4.6 is a result of two closely related effects in piezoelectricity. The first is the piezoelectric expansion of the lattice. A second more subtle effect is the rotation of the {103} planes as the c lattice constant increases, which rotates the peak position about the origin in reciprocal space.

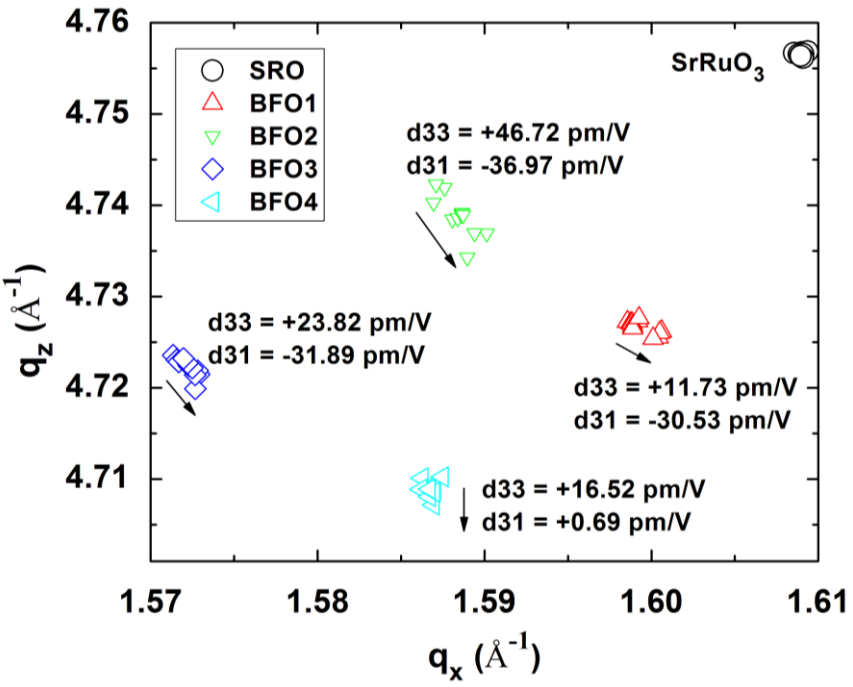

Figure 4.6. Peak position of $BiFeO_3$ {103} reflections under electric fields from 0 to 250 kV/cm. The $SrRuO_3$ reflection does not move, indicating no strain in the bottom electrode.

Apparent values of d_{33} and d_{31} for each domain are shown next to the reflections in Figure 4.6. The piezoelectric constants were determined by calculating the change in q_x and q_z at each electric field and fitting them to linear functions, where the slope of each line is taken to be the piezoelectric coefficient. The coefficients calculated in this manner do not account for rotations of the atomic planes and only represent apparent values. Nevertheless, it is clear that the piezoelectric response is different for each domain. The apparent value of d_{31} of domains at this position ranges from -37 pm/V to +0.69 pm/V. At another position on the sample, a domain with an even more positive d_{31} = +10pm/V was found.

We interpret the non-zero d_{31} to mean that these domains are no longer completely clamped. The likely explanation for the different values of d_{31} is that each domain is under

different stress states due to the incomplete relaxation of the film. A domain near the edge of a mosaic block any other type of defects would be under very different mechanical constraints than one in a perfectly epitaxial region of the film.

Crystal symmetry also plays a large role in the piezoelectric response. The effective d_{33} measured in this experiment is not along one of the rhombohedral crystal's high symmetry directions. In $BiFeO_3$, the largest piezoelectric response is parallel to the polarization direction along the pseudocubic [111] direction.[19] When the electric field is applied along the $[001]_{pc}$ direction instead, the piezoelectric tensor projected onto the new coordinate system, and d_{34}, d_{35}, and d_{36} become large. These are responsible for shear strains which deform the shape of the unit cell, rotating the atomic planes. Instead of variations in d_{33}, we believe that the variations in apparent d_{33} and d_{31} are caused by different shear strains for each structural variant. The amount of shear strain would be affected by mechanical constraints of neighboring domains, defects, or boundaries between mosaic blocks, resulting in variations in the rotation of the (103) planes observed in Figure 4.6.

Shear strains are observed in other rhombohedral ferroelectric thin films. Ouyang *et al*. demonstrate that for rhombohedral $0.67Pb(Mg_{1/3}Nb_{2/3})O_3–0.33PbTiO_3$ (PMN-PT) the piezoelectric response along the pseudocubic [001] is nearly at the maximum due to contributions from d_{35} and d_{36}.[20] When grown on cubic (001) $SrTiO_3$ substrates, the film forms multiple domains similar to $BiFeO_3$ films on $SrTiO_3$ substrates. Ouyang *et al*. suggest the shear components of the strains from neighboring domains are locked in place by each other as well as the substrate clamping. We hypothesize that polarization domain patterns

exist in which the shear strains in neighboring domains are parallel. This would allow neighboring domains to move. The motion of the (103) would be a combination of expansion from d_{33} and rotation from d_{35}.

The in-plane piezoelectric response of the partially relaxed $BiFeO_3$ lies between the polycrystalline and epitaxial regimes. A completely clamped film would have an effective d_{31} of zero.[21] Sol-gel polycrystalline $Pb(Zr,Ti)O_3$ films show increasing d_{31} with increasing film thickness, likely because of a decrease in the clamping effect of the substrate as the film gets thicker.[22] $BiFeO_3$ domains which have non-zero d_{31} are likely to be in regions which are more relaxed than regions with no in-plane piezoelectric response.

4.5. Conclusions

Relaxation of the epitaxial strain has significant consequences for the piezoelectric response of a ferroelectric thin film. Clamping by the substrate is predicted to reduce the out-of-plane piezoresponse.[23] In this study, we found that the out-of-plane piezoelectric coefficient d_{33} was 53 pm/V. It was uniform across the entire film, unlike the in-plane response. The in-plane coefficient d_{31} has a wide range of non-zero values. The variation in d_{31} is a consequence of epitaxial strain relaxation. The changes in magnitude and direction are likely caused by differences in local mechanical constraints on the domain. These include stresses from residual epitaxial strain and the local microstructure near a particular domain.

4.6. Chapter 4 references

[1] R. J. Zeches, M. D. Rossel, J. X. Zhang, A. J. Hatt, Q. He, C. H. Yang, A. Kumar, C. H. Wang, A. Melville, C. Adamo, G. Sheng, Y. H. Chu, J. F. Ihlefeld, R. Erni, C. Ederer, V. Gopalan, L. Q. Chen, D. G. Schlom, N. A. Spaldin, L. W. Martin, and R. Ramesh, *"A Strain Driven Morphotropic Phase Boundary in $BiFeO_3$,"* Science **326**, 977 (2009).

[2] A. J. Hatt, N. A. Spaldin, C. Ederer, "*Strain-induced isosymmetric phase transition in $BiFeO_3$*", Phys. Rev. B **81**, 054109 (2010).

[3] S. Tinte, K. M. Rabe, and D. Vanderbilt, *"Anomalous enhancement of tetragonality in $PbTiO_3$ induced by negative pressure,"* Phys. Rev. B **68**, 144105 (2003).

[4] S. Lisenkov, D. Rahmedov, and L. Bellaiche, *"Electric-Field-Induced Paths in Multiferroic $BiFeO_3$ from Atomistic Simulations,"* Phys. Rev. Lett. **103**, 047204 (2009).

[5] Q. Y. Qiu, R. Mahjoub, S. P Alpay, and V. Nagarajan, "*Misfit strain-film thickness phase diagrams and related electromechanical properties of epitaxial ultra-thin lead zirconate titanate films,"* Acta Mater. **58**, 823 (2010).

[6] H. Schmid, "*Multiferroic Magnetoelectrics*," Ferroelectrics **162**, 317 (1994).

[7] A. M. Glazer, *"Simple Ways of Determining Perovskite Structure,"* Acta Cryst. A **31**, 756 (1975).

[8] J. B. Goodenough, *"Theory of the role of covalence in the perovskite-type manganites $[La,M(II)]MnO_3$,"* Phys. Rev. **100**, 564 (1955).

[9] C. E. Ederer and N. A. Spaldin, *"Weak ferromagnetism and magnetoelectric coupling in bismuth ferrite,"* Phys. Rev. B **71**, 060401 (2005).

[10] J. F. Nye, *Physical Properties of Crystals*, (Oxford University Press, London, 1985).

[11] J. F. Shepard, P. H. Moses, and S. Trolier-McKinstry, *"The wafer flexure technique for the determination of the transverse piezoelectric coefficient d_{31} of PZT thin films,"* Sensors and Actuators A **71**, 133 (1998).

[12] I. Kanno, S. Fujii, T. Kamada, and R. Takayama, "*Piezoelectric characteristics of c-axis oriented $Pb(Zr,Ti)O_3$ thin films,"* Appl. Phys. Lett. **70,** 1378 (1997).

[13] F. Kubel, H. Schmid, "*Structure of a Ferroelectric and Ferroelastic Monodomain Crystal of the Perovskite $BiFeO_3$.*" Acta Cryst B. **46**, 698 (1990).

[14] S. E. Park and T. R. Shrout, *"Ultrahigh strain and piezoelectric behavior in relaxor based ferroelectric single crystals,"* J. Appl. Phys. **82**, 1804 (1997).

[15] S. Y. Yang, F. Zavaliche, L. Mohaddes-Ardabili, V. Vaithyanathan, D. G. Schlom, Y. J. Lee, Y. H. Chu, M. P. Cruz, Q. Zhan, T. Zhao, and R. Ramesh, *"Ferroelectric domain structure in epitaxial $BiFeO_3$ films ,"* Appl. Phys. Lett. **87**, 102903 (2005).

[16] R. N. Torah, S. P. Beeby, and N. M. White, "Experimental investigation into the effect of substrate clamping on the piezoelectric behaviour of thick-film PZT elements." J. Phys. D: Appl. Phys. **37**, 1074 (2004)

[17] V. Nagarajan, A. Roytburd, A. Stanishevsky, S. Prasertchoung, T Zhao, L. Chen, J. Melngalis, O. Auciello, and R. Ramesh, *"Dynamics of ferroelastic domains in ferroelectric thin films,"* Nature Mater. **2**, 43 (2003).

[18] D. Lebeugle, D. Colson, A. Forget, M. Viret, P. Bonville, J. F. Marucco, and S. Fusil, *"Room-temperature coexistence of large electric polarization and magnetic order in $BiFeO_3$ single crystals,"* Phys. Rev. B **76**, 024116 (2007).

[19] Y. H. Chu, M. P. Cruz, C. H. Yang, L. W. Martin, P. L. Yang, J. X. Zhang, K. Lee, P. Yu, L. Q. Chen, and R. Ramesh, *"Domain Control in Multiferroic $BiFeO_3$ through Substrate Vicinality,"* Adv. Mater. **19**, 2662 (2007).

[20] J. Ouyang, D.-M. Kim, C.-B. Eom, R. Ramesh, and A. L. Roytburd, *"Orientation dependence of the intrinsic converse longitudinal piezoelectric constant for $0.67Pb(Mg_{1/3}Nb_{2/3})O_3$-$0.33PbTiO_3$ ferroelectric films with a rhombohedral structure,"* Smart Materials & Structures **14**, 524 (2005).

[21] D.-H. Do, *Investigation of ferroelectricity and piezoelectricity in ferroelectric thin film capacitors* (PhD thesis), University of Wisconsin-Madison, (2006).

[22] J. F. Shepard, F. Chu, I. Kanno, and S. Trolier-McKinstry, *"Characterization and aging response of the d_{31} piezoelectric coefficient of lead zirconate titanate thin films,"* J. Appl. Phys. **85**, 6711 (1999).

[23] Q. Y. Qiu, R. Mahjoub, S. P Alpay, and V. Nagarajan, "*Misfit strain-film thickness phase diagrams and related electromechanical properties of epitaxial ultra-thin lead zirconate titanate films,"* Acta Mater. **58**, 823 (2010).

Chapter 5. Resonant and Non-Resonant Diffraction from Forbidden Reflections in $BiFeO_3$

The pseudocubic representation of $BiFeO_3$ is a powerful tool for understanding its structure, but it is also an oversimplification that misses important details. The pseudocubic unit cell makes it easy to visualize the displacements of Fe^{3+} ions, rotations of the oxygen octahedra, and the relationship to the substrate in epitaxial thin films. Nevertheless, it does not adequately describe the antiferromagnetic ordering, the rhombohedral symmetry, or the glide plane parallel to the [111] direction. For these reasons, it was realized by 1969 that a rhombohedral or hexagonal setting was necessary to describe the structural nuances of $BiFeO_3$.[1] Recent studies of single crystals have used the point group R3c and revealed additional modulations of the magnetic ordering.[2] The epitaxial strain in $BiFeO_3$ thin films introduces even more complexity to the structure by modifying the lattice constants and rotating the film.

We have observed x-ray reflections in thin films and in single crystals of $BiFeO_3$ which are not consistent with a rhombohedral R3c symmetry. Modulations at twice the pseudocubic interplanar spacings produce reflections that can be indexed as pseudocubic ½(*hkl*) planes. Initially, we believed reflections at the ½{111} could arise from magnetic scattering, but the reflections were orders of magnitude more intense than magnetic structure factor calculations predict. In order to determine the origin of these reflections and refine the structure further, we measured the intensities of ½(*hkl*) reflections in several $BiFeO_3$ thin films and in a bulk sample. The photon-energy dependence of the intensity of one of these

reflections was measured in order to determine which ions were displaced from the published structures. In the following sections, I describe the reflections we observed in thin film and bulk $BiFeO_3$, critically evaluate the possibility that the reflections arise from magnetic scattering, and discuss other possible origins of these reflections. We have found that small displacements of the Fe^{3+} ion and rotations of oxygen octahedra which are inconsistent with R3c symmetry can result in scattering at these wavevectors.

5.1.Predicted intensities of magnetic scattering

In order to design a magnetic scattering experiment and probe the antiferromagnetic response to an electric field, we calculated the positions and intensities of x-ray reflections produced by the magnetic order in $BiFeO_3$. The magnetic structure factor for ions with delocalized magnetic orbitals is similar to the structure factor F_{hkl} that is used in charge scattering calculations.[3] The spin magnetic unit cell structure factor $\boldsymbol{S}$ is given by[4]

$$\boldsymbol{S}(\boldsymbol{q}) = \sum_n \langle \boldsymbol{s}_n \rangle \, f_m(q) \exp[2\pi i \boldsymbol{q} \cdot \boldsymbol{r}_n]$$

where $\boldsymbol{q}$ is the reciprocal space vector and $\boldsymbol{r_n}$ is the fractional atomic position of the n^{th} ion. $<\boldsymbol{s_n}>$ is the spin angular momentum operator of the n^{th} ion and has units of Bohr magnetons. $f_m(q)$ is the magnetic form factor which depends on the magnitude of $\boldsymbol{q}$ and is different for each ion analogous to the atomic scattering factor. Since the orbital magnetization **L** for Fe^{3+} is nearly zero, the magnetization unit cell structure factor is assumed to be zero as well.[4]

Magnetic scattering also depends on the polarization of the x-rays and the spin direction. *M* is the scattering amplitude which includes the polarization dependent factor

calculated by Blume and Gibbs.[3] *M* is written in terms of the components of polarization of the incident beam parallel and perpendicular to the scattering plane. These are given in the bottom and top rows of the matrix, respectively. The prefactor $\hbar\omega/mc^2$ is the ratio of the photon energy to the energy equivalent of the mass of the electron photon, which is 511 keV. This factor comes from the fundamental origin of the magnetic scattering process in the relativistic description of Thomson scattering.[5]

$$M(\boldsymbol{k_0}, \boldsymbol{k'}, \boldsymbol{S(q)}) = r_0 \frac{\hbar\omega}{mc^2} \begin{bmatrix} \boldsymbol{S} \cdot \boldsymbol{k_0} \times \boldsymbol{k'} & \frac{-|q|^2}{2k^2} \boldsymbol{S} \cdot \boldsymbol{k'} \\ \frac{-|q|^2}{2k^2} \boldsymbol{S} \cdot \boldsymbol{k_0} & \boldsymbol{S} \cdot \boldsymbol{k_0} \times \boldsymbol{k'} \end{bmatrix}$$

The largest factor in the magnetic scattering amplitude for the diagonal components of *M* is $\boldsymbol{S}\cdot\boldsymbol{k}_0\times\boldsymbol{k}'$. This factor is largest when the spin direction is perpendicular to the scattering plane. The intensity of a reflection is proportional to the magnetic scattering amplitude times its complex conjugate, *MM**.

The relative intensities of magnetic and charge scattering was estimated. Magnetic scattering from the G-type antiferromagnetism in $BiFeO_3$ creates reflections at $\boldsymbol{q} = ½(hkl)$, half the wavevector of charge scattering reflections. The magnetic scattering intensity was estimated for a horizontal scattering geometry, the pseudocubic ½(111) planes in $BiFeO_3$, a horizontally polarized incident beam, and a photon energy of 7.1 keV. The magnetization of $BiFeO_3$ is 4.1 μ_B for each Fe^{3+} ion.[6] The magnetic form factor for Fe^{3+} at $\boldsymbol{q} = 1/d_{1/2(111)} =$ 0.219 $Å^{-1}$ is 0.7.[7] The highest intensity occurs when the spin polarization direction is perpendicular to the scattering plane, in which case the magnetic scattering factor is:

$$M = sin\ 2\theta\ \frac{\hbar\omega}{mc^2} r_0 \sum_{n=1}^{n=6} f_m(q)\,\langle \boldsymbol{s_n} \rangle \exp[2\pi i \boldsymbol{q}\cdot\boldsymbol{r}_n]$$

where 2θ is twice the Bragg angle and the scattering factor is summed over the six Fe^{3+} ions in the $BiFeO_3$ unit cell. Using the atomic positions given in Kubel and Schmidt[8] at 7.1 keV, the magnetic scattering for the ½(111) reflection is:

$$M = \sin 22° \frac{7.1\ keV}{511\ keV} r_0 \sum_{n=1}^{n=6} 0.7 \cdot 4.1\mu_B \cdot (-1)^n \cdot \exp[2\pi i \boldsymbol{q}\cdot\boldsymbol{r}_n]$$

which reduces to 0.008 r_0^2, compared to the squared structure factor for the (111) reflection of 93,969 r_0^2. Based on these calculations, we expect magnetic reflections in $BiFeO_3$ to be approximately eight orders of magnitude less intense than the charge scattering reflections.

5.2. Experimental setup

We measured the intensities of ½{*hkl*} type reflections using x-ray diffraction in thin films and bulk samples of $BiFeO_3$. Four samples were used in these experiments. The thicknesses, orientations, and layer structures of these samples are summarized in Table 5.1. The two (001) oriented films were compared to examine the effects of thickness on the half order reflections. A bulk crystal of $BiFeO_3$ grown by Sang-Wook Cheong is used as a strain-free comparison to the thin films. A 600 nm (111)-oriented $BiFeO_3$ film was chosen as well because this orientation avoids the cubic/rhombohedral symmetry mismatch which complicates the film structure. The rocking curves for this sample were very small, which caused problems described in Section 5.2.3.2, so this sample was mainly used as a reference.

Name	Thickness / size	Substrate	Orientation	Substrate miscut
B3-2	400 nm	15 nm $SrRuO_3$ on $SrTiO_3$ substrate	(001)	4° towards [010]
B-180-C	600 nm	$SrTiO_3$	(001)	4° towards [100]
B-180-E	600 nm	$SrTiO_3$	(111)	vicinal
SS-16	0.5 mm ×3 mm ×3mm	n/a	(001)	n/a

Table 5.1. Descriptions of the samples used in experiments described in Chapter 5. Sample B3-2 was also used in Chapter 2.

5.2.1. Synchrotron x-ray diffraction

Synchrotron x-ray diffraction experiments were conducted at Sector 2-ID-D of the Advanced Photon Source to study the weak reflections at ½(*hkl*) wavevectors. A small beam was used to eliminate broadening of the reflections from mosaic spread. The beam was focused using a 320 µm Fresnel zone plate with a 35 µm diameter beamstop. A 20 µm diameter pinhole used as an order sorting aperture. The spot size was not measured during the experiments, but 400 nm is a typical value for the 320µm zone plate at 2-ID-D. A vertical scattering geometry was used for the 600 nm (001) film; all other measurements were performed using horizontal geometries. Photon energies of 7.05 keV and 7.1 keV were chosen to reduce the background from Fe x-ray fluorescence, which appears above the Fe K absorption edge at 7.112 keV. Further details are given in Section 5.4. Attenuators were placed in the beam during measurements from the {111} family of structural reflections to avoid damaging detectors with large intensities.

The direct beam passed through an ion chamber after going through the attenuators, before reaching the sample. The ion chamber provides a measure of the beam intensity, as well as accounting for the decay of the electron current in the storage ring. The ion chamber intensity was used for normalization when comparing intensities of different reflections. The ion chamber proved not to be useful a normalization when comparing between reflections at different energies because the counting efficiency of the ion chamber significantly varies with energy.

Samples were mounted on a kappa diffractometer,[9] placed at the focal point of the incident x-ray beam, and rotated to meet the diffraction conditions. The (001)-oriented thin film and bulk samples were placed on a 35.3° wedge to bring the (111) planes parallel to the scattering plane. The wedge angle was chosen to be the complement of the angle between the (001) face of the sample and the (111) plane. When the samples were mounted on the wedge, it was possible to make scans in which the incident angle is half of 2θ along the [111] direction. This geometry made it significantly easier to find the weak half order reflections.

Two detectors were used to measure the diffracted x-rays in these experiments. A scintillation detector (Bicron, Inc.) was used to measure the weak ½(*hkl*) reflections because it was capable of counting individual photons. A helium-filled flight path was placed between the sample and detector to reduce attenuation of the beam in air. Slits were placed just in front of the detector, defining the angular acceptance. Guard slits closer to the sample reduced background from air scatter of the direct beam. The amplified output of the scintillation detector was filtered using a single channel analyzer (SCA) to eliminate counts from x-ray photons with energies much higher or lower than 7.1 keV. The energy resolution

was limited by the scintillator to approximately 50%. The output from the SCA was counted by a scaler.

For the brighter {111} reflections, a charge-coupled device (CCD) area detector was used to quickly locate the reflections and to acquire three-dimensional reciprocal space maps. No flight paths were necessary with the CCD because the {111} reflections were orders of magnitude more intense than background. The angular location of the CCD was calibrated by recording the attenuated direct beam when the detector arm was at $2\theta = 0°$. The angle spanned by each pixel of the CCD was determined by recording the direct beam position after moving the detector in 2° steps in 2θ and del, the angle perpendicular to the horizontal scattering plane.

Changes in the half order reflections in response to electric field were probed using the millisecond-scale time resolved diffraction described in Section 1.7.4.1. A 200 μm diameter top electrode on the 400 nm (001) sample was contacted by a tungsten probe tip with a 5 μm radius at its end (Cascade Microtech DCP-150R). The $SrRuO_3$ bottom electrode was grounded. Prior to beginning a time resolved measurement, a voltage was applied across the capacitor in order to switch the polarization parallel to the electric field. Unipolar triangle pulses with a duration of 20 ms were applied to the electrode using a function generator (Agilent 33120A). The multichannel scaler measured the number of counts over a period of 2 seconds in 1 ms increments. Hysteresis loops were measured periodically to make sure the capacitor had not undergone dielectric breakdown. When a capacitor was found to be shorted, the probe tip and x-ray beam were moved to a new device.

5.2.2. X-ray Diffraction using a rotating anode source

A rotating anode x-ray diffractometer in our laboratory at the University of Wisconsin was used to measure the ½{111}, {111}, and ½{113} reflections from the bulk $BiFeO_3$ sample. X-rays produced by a copper rotating anode x-ray generator (Rigaku UltraX 18 Rotaflex) were monochromatized by a bent LiF crystal. The Cu K_β component of the spectrum emitted by the source was eliminated by the monochromator. The beam that reached the sample contained largely Cu $K_{\alpha 1}$ radiation, but still contained some Cu $K_{\alpha 2}$ because the energy resolution of the monochromator was not sufficient to completely eliminate the Cu $K_{\alpha 2}$ component. The sample was mounted on a four-circle diffractometer (Huber) and oriented to meet the diffraction conditions of each reflection. The diffracted beam passed a flight path evacuated using a membrane pump. A scintillation detector was used to detect the diffracted beam. Slits placed in front of the detector determined the angular resolution in 2θ.

The incident beam on the rotating anode was much less intense than at the synchrotron. Because the half order reflections could have intensities as low as a 1 count per second eliminating the background was extremely important. The first step was setting the SCA window to be as small as possible so that only 8 keV x-rays were counted. The energy resolution of the scintillation counter is relatively poor, so that x-rays with the same wavelength can produce output pulses with heights that differ by up to 50%.[10] The signal from the $\lambda/2$ x-rays were eliminated by filtering the amplified output using a single channel analyzer (SCA, Ortec 550).

A lead cap around the end of the scintillation counter eliminated much of the background from very high-energy x-rays. The background near the ½(111) consisted of around 15 counts per second of x-rays which produced very high pulse heights in the amplified output of the scintillation counter. Several layers of lead tape placed over the guard slits were not sufficient to completely absorb these x-rays. A lead cap with a thickness of 1/16" with a square hole in the center placed over the end of the scintillation counter reduced the background to 1-2 counts/sec around $2\theta = 22°$.

5.2.3. Eliminating sources of scattering at ½(*hkl*)

Since the reflections at ½(*hkl*) had such low intensities, it was very important to eliminate any other sources of scattering and increase the intensity of the diffracted beam. The first source of background was a relatively uniform distribution of intensity arising from the scattering of the direct beam by air. This contribution was removed by placing a set of slits near the sample which block the air scatter. These guard slits had an opening larger than the angular acceptance of the slits in front of the detector, so their only role was to block photons scattered by the air. Flight paths filled with helium gas were placed between the guard slits and the detector to reduce attenuation of diffracted beam by air.

5.2.3.1. ½(*hkl*) reflections from rotations of oxygen octahedra

Rotations of the oxygen octahedra produce reflections at ½(*hkl*) wavevectors which can obscure weaker sources of scattering. They reduce the symmetry from the space group of the pseudocubic perovskite Pm3m. The rotations of oxygen octahedra can be described using a notation based on a hypothetical doubling of a cubic unit cell along each axis.[11] Rotations

in opposite directions of successive octahedra along an axis, for example along the ***a*** axis, require doubling the unit cell in that direction. These are called a^- rotations. In the most general case, the new unit cell is twice as large in each direction, corresponding to a volume $2\boldsymbol{a}_{pc}\times 2\boldsymbol{b}_{pc}\times 2\boldsymbol{c}_{pc}$.

The larger unit cell leads to new x-ray reflections that are not observed in the parent structure. Glazer derived a relationship between the type of octahedral rotation and the reflections allowed by octahedral rotations.[12] For $a^- a^- a^-$ tilt systems such as $BiFeO_3$, reflections of the type ½(*hkl*) with *hkl* odd and $h\neq k$, $k\neq$l, or $h\neq l$ are allowed. For example, $\frac{1}{2}(113)_{pc}$ or $\frac{1}{2}(311)_{pc}$ are allowed by the octahedral rotation but $\frac{1}{2}(112)_{pc}$ is not. The intensities of reflections from octahedral rotations are proportional to the rotation angle.[12] The integrated intensity of these reflections as function of temperature has been used to determine the onset of phase transitions in PZT thin films.[13]

In the x-ray scattering experiments using the rotating anode diffractometer, we have observed octahedral rotation reflections in bulk $BiFeO_3$ at ½{113} type wavevectors. Structure factor calculations using atomic positions from powder diffraction refinements of $BiFeO_3$ predict these reflections to be two to three orders of magnitude less than the {111} reflections. We observe these reflections at the predicted wavevector. These reflections are 4.4×10^{-2} times the intensity of the corresponding (111) reflections, compared to the calculated value of 3.7×10^{-2}. Two reflections are shown below in Figure 5.1. The peak intensities are different because the structure factor for the ½(-113) is larger than for the ½(-1-13) and because the crystal has unequal volumes of each ferroelastic domain. The domain

populations were determined from the intensities of four (111) reflections, measured in 90° rotations of the azimuthal angle.

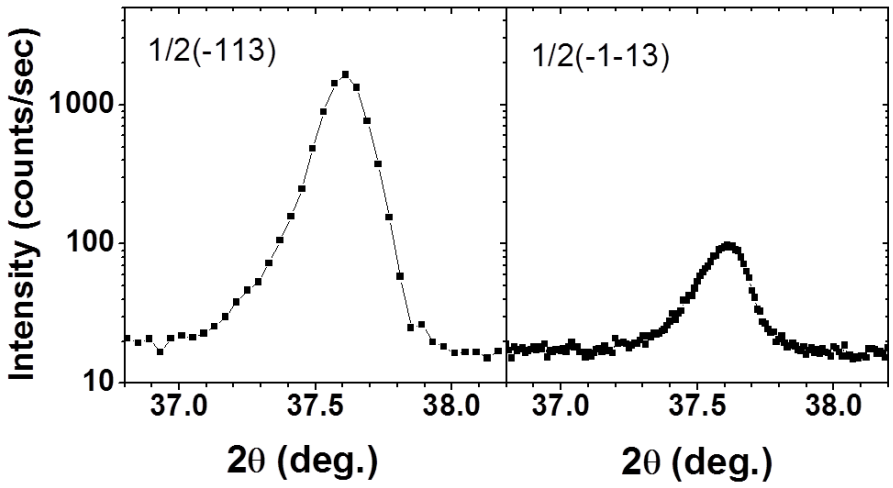

Figure 5.1. ½{113}$_{pc}$ reflections caused by rotations of the oxygen octahedra in bulk $BiFeO_3$. The (-111) and (-1-11) reflections in this sample were 4×10^4 and 2×10^4 counts per second, respectively.

Magnetic scattering is predicted to be much weaker than these octahedral rotation reflections. The magnetic scattering at the ½(113) at 8.05 keV is 3×10^6 times less than the ½(1-13) reflection. In order to avoid trying to measure a small signal on top of a large one, we chose to look for magnetic scattering at wavevectors which are forbidden to octahedral rotation reflections. For the $a^-a^-a^-$ rotation pattern, the structure factors for ½(*hhh*) type reflections are zero. We chose to look for magnetic scattering from the ½(111) and ½(333) planes.

5.2.3.2. Multiple scattering

Multiple diffraction within a crystal produces intensity at forbidden reflections, making it difficult to observe weak scattering signals at the same wavevectors. If an x-ray

beam is diffracted from a set of planes that is allowed and is then diffracted a second time while still inside the crystal, the doubly-diffracted beam can exit at an angle associated with a forbidden reflection.[14] This is shown schematically below in Figure 5.2.

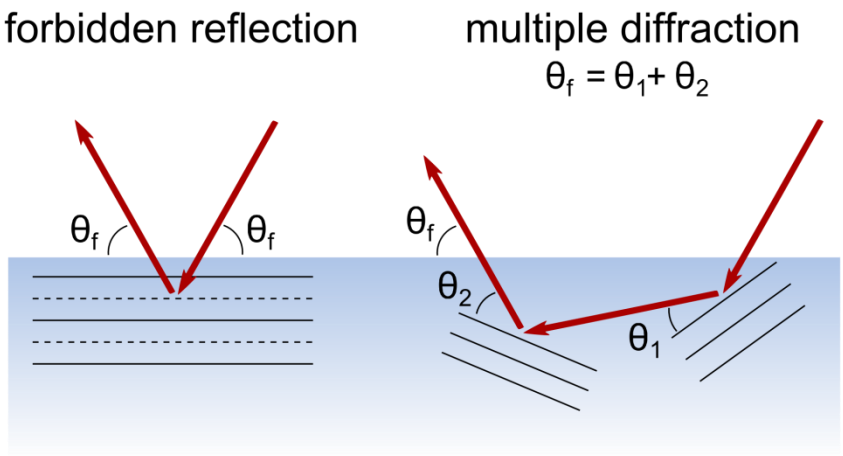

Figure 5.2. Multiple diffraction can result in intensity at an angle associated with the Bragg angle of a forbidden reflection, θ_f. ($h_1k_1l_1$) and ($h_2k_2l_2$) are allowed reflections with Bragg angles θ_1 and θ_2, respectively. By diffracting from two allowed reflections in succession, the beam exits the sample at θ_f.

Multiple diffraction requires precise azimuthal orientation of the crystal because often planes only meet the Bragg conditions when the beam is incident with a particular three-dimensional direction. The incident beam must diffract at the correct angle to meet the Bragg condition of the second set of planes. Multiple diffraction peaks can be distinguished from singly diffracted beams by rotating about the plane normal. These reflections have small angular widths (less than 0.5°) but singly diffracted beams do not change intensity.

Multiple scattering at the ½(111) can be observed in (111) $BiFeO_3$ thin films. Synchrotron x-ray microdiffraction at 7.1 keV revealed a relatively weak reflection at the ½(111), but not at the ½(-111), ½(-1-11), or ½(-1-11). The reflections with negative Miller indices were not observed because this film had a single structural variant. No splitting of the

(111) reflection was observed, so (111) oriented $BiFeO_3$ thin films, consistent with other groups' observations of monodomain films. In order to determine whether the ½(111) was caused by magnetic scattering or multiple diffraction, the incident angle and diffracted angle 2θ were fixed while the azimuthal angle was rotated and the intensity was recorded (Figure 5.3).

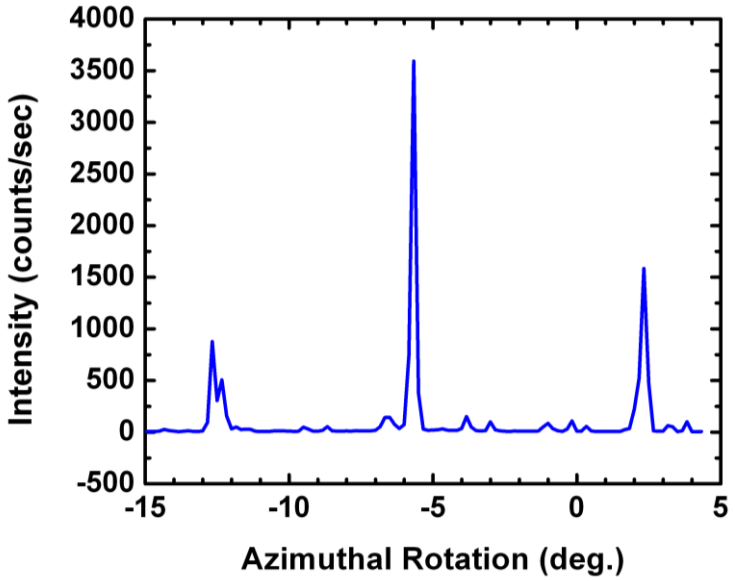

Figure 5.3. Intensity of $BiFeO_3$ ½(111) as a function of azimuthal angle in a (111) oriented thin film.

The sharp dependence of intensity on azimuthal angle in Figure 5.3 is characteristic of multiple scattering. In principle, the multiple scattering peaks can be indexed and used to determine the in-plane orientation of the film and to measure the in-plane lattice constants.[14] For us, however the multiple diffraction peaks are a nuisance which has to be avoided in order to measure scattering from other sources. For example, magnetic scattering in antiferromagnetic Fe_3O_4 is orders of magnitude less than the double diffraction peaks.[15]

5.3. Forbidden ½{111} reflections in thin films

We observed Bragg reflections at pseudocubic ½{111} wavevectors. First, reciprocal space maps of the $BiFeO_3$, $SrRuO_3$, and $SrTiO_3$ (111) reflections were acquired to obtain an estimate of the domain populations and to find the angular splitting of the $BiFeO_3$ {111}. The intensities of these reflections were also used as a baseline for comparing calculated scattering factors to observed intensities. The incident angle was varied as a series of two-dimensional diffraction patterns were recorded with a CCD detector. The intensity in each image was summed over the out-of-plane direction (del) to give a 2D reciprocal space map. One such map of the $BiFeO_3$ {111} reflections from sample B3-2 is shown in Figure 5.4. The focused synchrotron x-ray beam had a photon energy of 7.1 keV. The intensity is plotted as a function of $\boldsymbol{q_x}$ and $\boldsymbol{q_z}$, where $|\boldsymbol{q}|$ is in units of $1/d$. The sample was aligned on the diffractometer such that the $\boldsymbol{q_x}$ was nearly parallel to the $SrTiO_3$ [110] direction and $\boldsymbol{q_z}$ was parallel to the $SrTiO_3$ [111] direction.

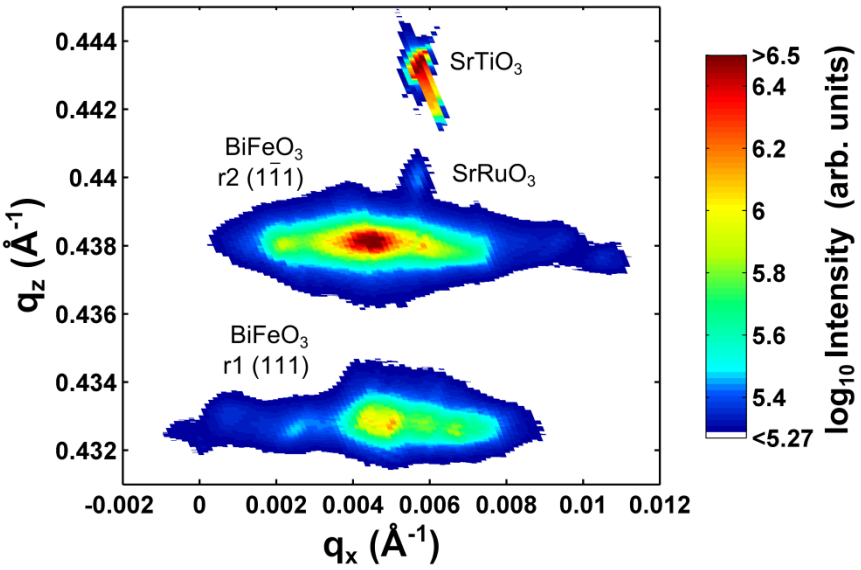

Figure 5.4. Reciprocal space map of the $SrTiO_3$, $SrRuO_3$, and $BiFeO_3$ pseudocubic (111) reflections of sample B3-2. Diffraction pattern measured using a focused x-ray beam with a photon energy of 7.1 keV.

There are two $BiFeO_3$ reflections near the (111) in Figure 5.4. The two $BiFeO_3$ reflections are broad in $\boldsymbol{q_x}$ and $\boldsymbol{q_y}$, but sharper in $\boldsymbol{q_z}$. This indicates a variation in the orientation of the planes, but little variation in the interplanar spacing. Each $BiFeO_3$ reflection comes from a structural variant of the strained rhombohedral film, as described in Section 2.5. The two reflections are have indices (1-11), which arises from r2 domains and (111), arising from r1 domains. The $BiFeO_3$ reflections have oscillations in the intensity in the $\boldsymbol{q_x}$ direction, likely from the interference of coherent scattering between domains in two mosaic blocks.

A reciprocal space map acquired at half the wavevector of the (111) reflections is shown in Figure 5.5. The scintillation detector and flight paths were chosen because we

could detect weaker diffracted signals in this way. Reflections at the ½(111) from r1 domains and ½(1-11) from r2 domains were observed.

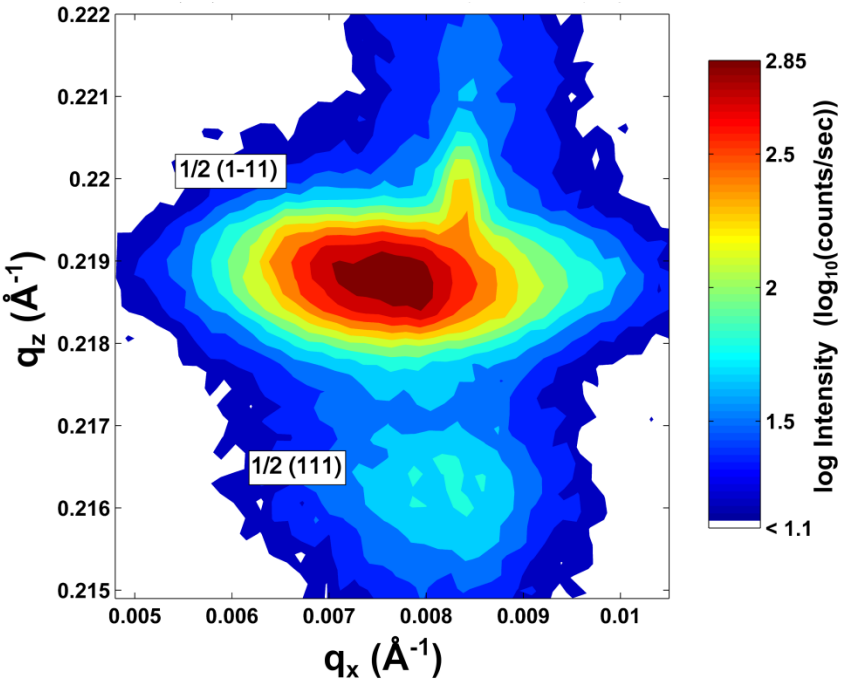

Figure 5.5. Reciprocal space map of ½(1-11) and ½(111) $BiFeO_3$ reflections from sample B3-2.

The intensities of the ½{111} reflections were compared to the {111} reflections in order to relate calculated structure factors to real intensities. The ½(1-11) reflection is more intense and much broader than the ½(111) reflection. The ½(111) reflection is 2×10^{-4} times the intensity of the (111); the ½(1-11) is 1×10^{-3} times the intensity of the (1-11). Although the intensity of these reflections varied at different positions on the sample, the ½(1-11) was always observed to be brighter than the ½(111) at all positions that we probed in the 400 nm film. Based on the observed intensities of the {111} reflections, we predicted that magnetic scattering reflections would have intensities of 0.5 counts per second. The reflections observed here were 1,000 times more intense than the magnetic scattering signal, making it

extremely difficult to probe the magnetic ordering using x-ray diffraction. Thus we have considered other possible origins of the high-intensity ½{111} reflections.

We determined that multiple scattering is does not occur in (001)-oriented $BiFeO_3$ films by measuring the intensity of the ½(111) as a function of azimuthal angle. The mounting wedge made it impossible to scan about the surface normal on the kappa diffractometer at Sector 2-ID-D. The mu rotation is a good approximation for the azimuth for small angles, but at large angles the incident angle is changed by increasingly larger amounts. Scans of mu versus peak intensity show a slow decrease in intensity caused by gradually changing the incident angle (Figure 5.6).

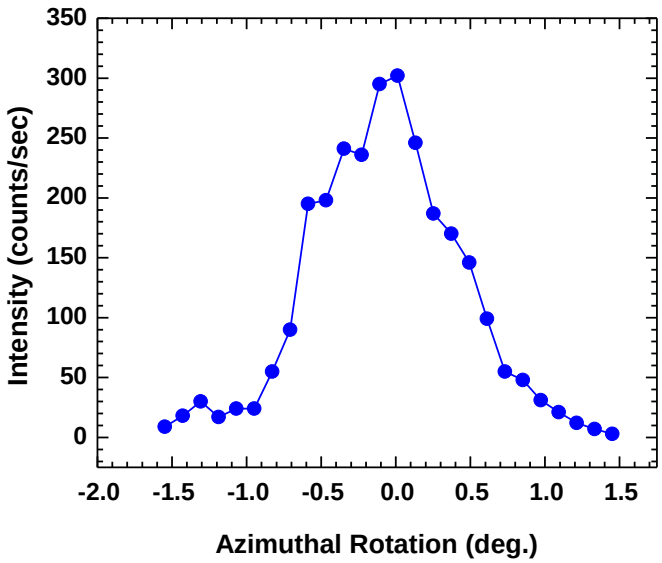

Figure 5.6. Dependence of diffracted intensity at the ½(111) on azimuthal angle in a 600 nm (001) $BiFeO_3$ film (B-180-C).

The intensity of the ½(111) is not sharply dependent on the azimuthal angle. It decreases large rotations of the azimuthal angle similar to any other Bragg reflection because

of the gradual change in incident angle of the x-rays. The ½(111) is thus not caused by multiple scattering in the (001) thin films.

Structure factor calculations for charge scattering predict zero intensity at the ½{111} family of reflections. These calculations used the atomic positions for $BiFeO_3$ reported in Kubel and Schmidt and the structure factor of Chapter 1.[8] It should be noted that these reflections are forbidden in R3c symmetry and no charge scattering is expected at these wavevectors. The large intensity of the ½{111} reflections suggests that there is a structural distortion that is unaccounted for in atomic positions found by neutron diffraction studies. Using the ratio of intensity for the ½(111) to that of the (111), we found that the observed intensity of the ½(111) corresponds to 18.8 r_0^2, or approximately equal to the scattering from an arrangement of four electrons with this periodicity.

5.4. ½{111} reflections in bulk $BiFeO_3$

We wanted to determine if the structural distortion causing these reflections was related to epitaxial strain. We measured the ½{111} reflections in a thicker (001) film and a bulk sample of $BiFeO_3$. Epitaxial strain can change the symmetry and atomic structure of a thin film and might induce structural distortions unique to thin films. To determine the effects of varying strain states, we measured half order reflections from a 600 nm (001) film and a bulk crystal.

The 600 nm film had reflections at the ½(111) similar but not identical to the 400 nm film. Reciprocal space maps were acquired near the $BiFeO_3$ ½(111), (111), and ½(333)

Bragg reflections (Figure 5.7). The photon energy was chosen to be below the Fe K edge (7.1 keV) in order to reduce background scattering. The intensity at each point in $\boldsymbol{q_x}$ and $\boldsymbol{q_z}$ is plotted as a function of color, where the color bar to the right of each map relates count rate to color. Attenuators were necessary for the allowed Bragg reflections. The intensities in the plots of Figure 5.7 were normalized to the intensity simultaneously measured with an ion chamber so the attenuation factor is accounted for.

The 600 nm film serves as a comparison because it is more relaxed than the 400 nm film but has not completely relaxed to the bulk lattice parameters. We find that the unmixed ½(111) reflection in the 600 nm film is weaker than that of the 400 nm film. Accurately comparing intensities can be extremely complicated, however. The intensity of a thin film Bragg reflection measured with a small beam is affected by the domain population inside the diffraction volume, the reflection's structure factor, and the orientation of the mosaic block with respect to incident x-ray beam. We measured the {111} reciprocal space map in several places on the sample and consistently found that the (111) reflection was brighter than the (-111) reflection. The intensities ($F_{hkl} \cdot F^*_{hkl}$) for the mixed index peaks are calculated to be approximately 20% higher than for the unmixed reflections. The reciprocal space map was taken with detector slits that had an acceptance of about 1° in the direction perpendicular to the scan of the plane (roughly equivalent to the chi rotation of the sample), which was large enough to accept both reflections. After accounting for domain populations, rotations of the mosaic blocks, and structure factor differences, we conclude that the ½(111) in the 600 nm film is weaker than in that of the 400 nm film. This indicates that strain changes the magnitude or direction of the distortions causing the ½{111} reflections.

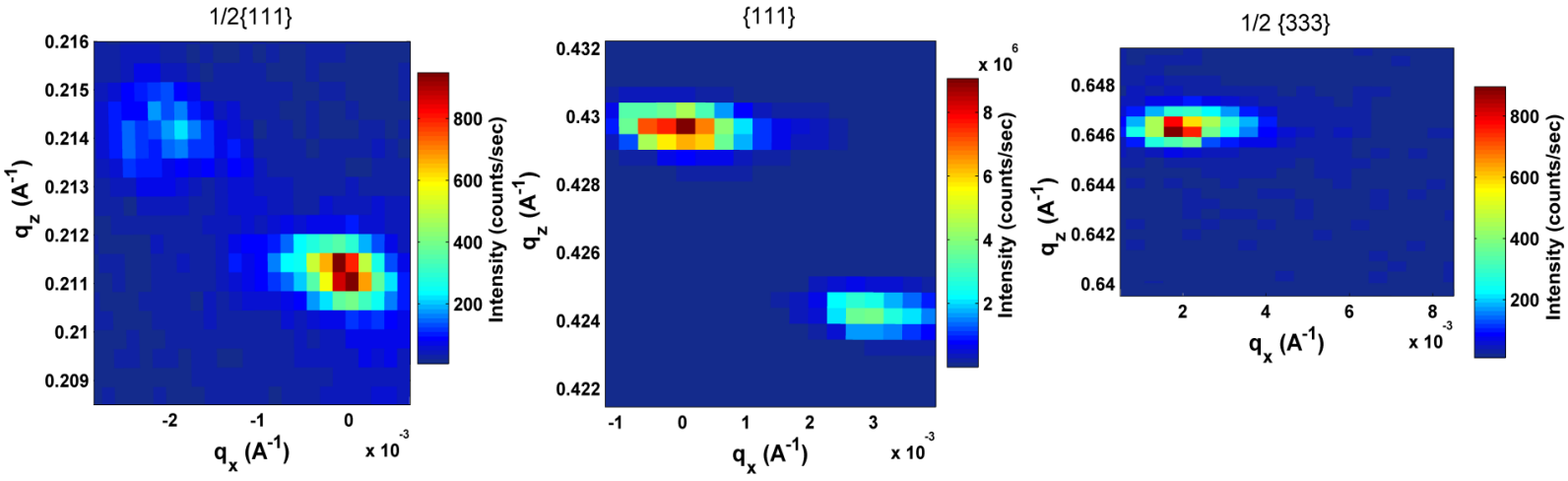

Figure 5.7. Reciprocal space maps of the ½(111), (111), and ½(333) $BiFeO_3$ Bragg reflections from the 600 nm $BiFeO_3$ thin film. The center plot has a significantly larger intensity scale than the other two plots since the (111) reflections are three orders of magnitude brighter than the ½(111) and ½(333). The white section in the ½(333) plot is left intentionally because the scan did not cover the portion of reciprocal space containing one of the expected reflections.

The thin films are strained and misfit defects are introduced during the relaxation process which may contribute to the intensity of the ½{111} type reflections. To determine whether the half order reflections are a byproduct of epitaxial constraints or the relaxation process, the same reflections were measured in an unstrained bulk $BiFeO_3$ crystal. The bulk sample contained all four structural variants described in section 2.5.1. Measurements with an unfocused beam show that the sample contains more of variant r1 than of the other three. The scattering geometry was designed such that the (111) planes of the r1 variant were in the scattering plane. We observed ½{111} reflections from the r2, r3, and r4 variants which were aligned to diffract from the ½(-111), ½(-1-11), and ½(1-11), respectively. These three reflections had the same interplanar spacing and diffract at the same *2θ*. A two-dimensional scan of the incident angle and the detector's out of plane angle del measured a plane in reciprocal space which cut through the center of all three mixed reflections (Figure 5.8).

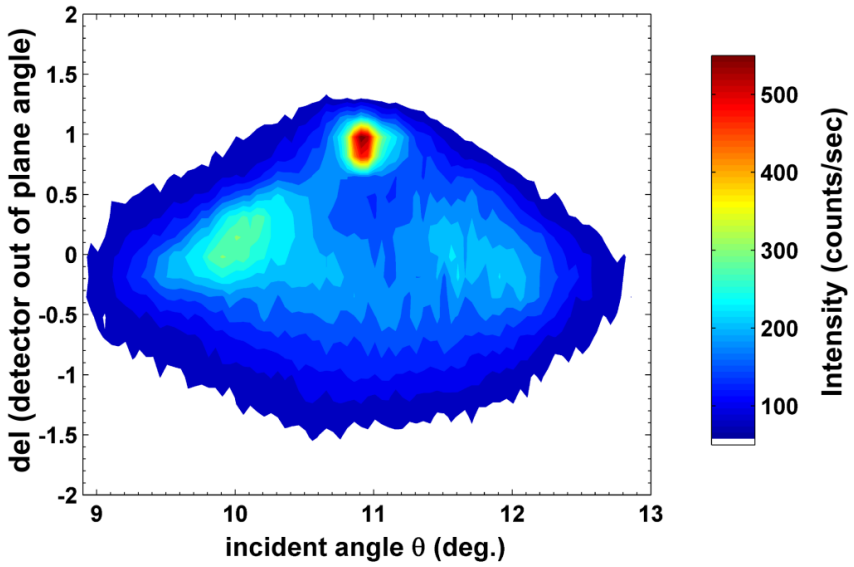

Figure 5.8. Reciprocal space map at constant *2θ* of the mixed ½ (-111), ½ (-1-11), and ½(1-11) reflections in bulk $BiFeO_3$.

In the bulk sample, the ½{111} reflections were less intense than in the 600 nm film. Count rates were normalized to the {111} reflections to compare intensities accurately. Measurements taken at the synchrotron at 7.1 keV failed to detect the unmixed ½(111) reflection. Figure 5.9 is a reciprocal space map showing two of the three possible mixed reflections, along with the theoretical position of the unmixed ½(111) reflection.

The red circles in Figure 5.9 indicate the theoretical positions of scattering from the spin spiral found in bulk $BiFeO_3$. Neutron diffraction studies of the magnetic ordering in bulk $BiFeO_3$ show a spiral modulation of the spin direction within the (111) plane with a period of 62 nm.[16,17] Non-resonant scattering from the spin spiral in the bulk is possible as well – satellite peaks at $\boldsymbol{q_{1/2(hkl)} \pm q_{spiral}}$ are marked with red circles. None of these reflections were found in the bulk at this energy. If the unmixed reflection is present, it at least 10^5 times less intense than the (111) reflection.

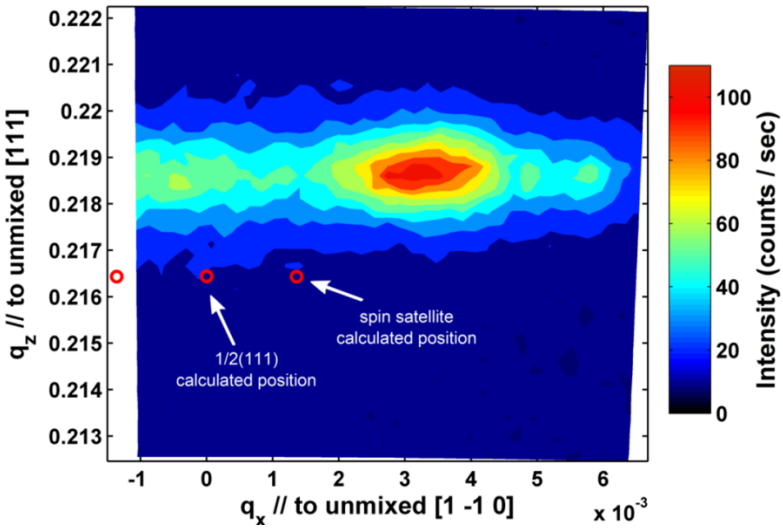

Figure 5.9. Reciprocal space map of the 1/2(-111) and 1/2(-1-11) reflections in bulk $BiFeO_3$. Red circles indicate the theoretical position of the ½(111) reflection and satellite reflections from the magnetic spin spiral.

Although synchrotron microdiffraction reciprocal space maps did not find the ½(111) reflection in the bulk, it was observed using a rotating anode x-ray diffractometer. The ½(111) was 3 counts per second, 10^{-5} times the (111) intensity. It is not immediately clear why this reflection was observed using a rotating anode diffractometer but not with the synchrotron measurements. One possibility is that the ½(111) reflection is dependent on the iron scattering factor. The synchrotron measurements were conducted below the Fe K edge, and the rotating anode experiments above the edge at 8.05 keV. If the intensity of the ½(111) depends on the Fe scattering factor, then it would be more intense at energies above the Fe K edge where f'' is larger. Another possible explanation is that the diffraction volume for the synchrotron measurements was small enough to completely miss the r1 structural variant that produced the ½(111) reflection. The rotating anode has a large spot size of several square millimeters, so the diffraction volume would be large enough to include all structural variants and the ½(111) reflection was observed.

The pattern we observed is that the intensities of the ½{111} reflections increase with epitaxial strain. The bulk had weak reflections, the 600 nm was less so, and the ones from the 400 nm film were brightest of all. The structural distortion causing these reflections is increased in thin films, but the reflections from the bulk sample show that these distortions are not caused by epitaxial strain alone. In order to quantify the relation between intensity and strain, we applied a piezoelectric strain to the 400 nm film and measured the intensity of the ½{111}.

5.5. Response of ½{111} reflections to piezoelectric strain

Time-resolved microdiffraction experiments determined that the intensities of the ½{111} reflections were proportional to piezoelectric strain. The ½{111} diffraction patterns were measured while an electric field was applied to the 400 nm $BiFeO_3$ (001) film. The sample geometry was carefully chosen so the half order reflections from different structural variants would be easy to identify. The sample was mounted so the (111) planes of r1 domains and the (1-11) planes of r2 domains were in the scattering plane. r1 and r2 type domains made up the majority of ferroelectric domains in the as-grown state of this sample, as discussed in Chapter 2. The sample was positioned so the focused beam diffracted only from regions of $BiFeO_3$ which were subjected to the electric field. The ½(111) has a larger interplanar spacing than reflections with mixed positive and negative indices, so the reflection at smaller 2θ can easily be indexed as ½(111) and the mixed reflection ½(1-11).

The intensity of the half order reflections was measured as a function of electric field. The time resolved diffracted intensity was measured at each point in a scan of the incident angle, θ. The detector angle 2θ was not scanned at the same time – instead the angular acceptance of the detector was increased to 0.078°. The maximum applied electric field was 175 kV/cm, which changes 2θ by a maximum of 0.03°, estimated by calculating the strain assuming piezoelectric constants of d_{33} = 53pm/V and d_{31} = 20 pm/V. The intensity at each point is the sum of counts detected during a 1 ms window, repeated 1,000 times to give a total counting time of 1 second. An example of the incident angle vs. time for field ranging from 0 to 175 kV/cm is shown below in Figure 5.10.

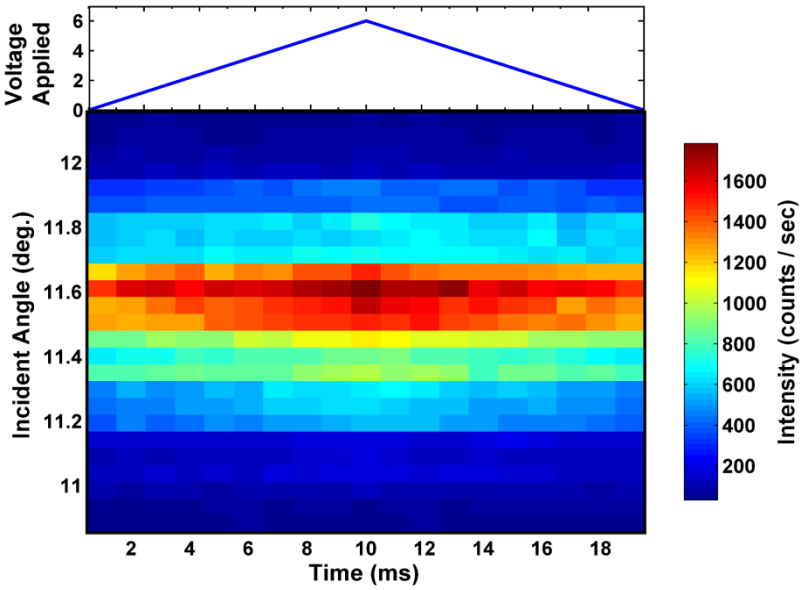

Figure 5.10. Response of ½(1-11) reflection to electric field in B3-2, the 400 nm film. (a) Voltage applied to the top electrode as a function of time. This pulse was repeated 1,000 times in order improve counting statistics for the diffracted intensity. (b) Time resolved intensity of ½(1-11) reflection. The intensity vs time (horizontal axis) was measured at each point of an incident angle scan (vertical axis).

The peak intensity increased when the electric field was applied. The piezoelectric strain induced peak shift was not measurable from these θ scans; the center of the peak was predicted to shift by -0.015° and the scan step size was 0.052°. The ½(1-11) intensity increases with electric field and is brightest in the center of Fig. 5.11(b). Structure factor calculations for the allowed {111} reflections predict no change in intensity as a function of electric field, assuming that the fractional coordinates of the atoms do not change. This is not necessarily a valid assumption. Perovskite materials subjected to large strains have been found to keep the bond lengths nearly constant for five B-O bonds at the cost of lengthening the sixth.[18,19] Holding bond lengths constant under strain changes the fractional coordinates, which could account for the observed intensity change. To test this hypothesis, the intensity

of allowed reflections (111) and (1-11) as well as the ½(111) were measured as a function of electric field.

Quantitative values for the intensity change were calculated by summing over the θ scan at each point in the time scan to give integrated intensity versus electric field. The electric field dependence for two ½{111} reflections and their corresponding {111} reflections are plotted below in Figure 5.11. Change in intensity was calculated as a percentage of the intensity near $E = 0$, taken to be the average of the intensities at 0 ms and 20 ms.

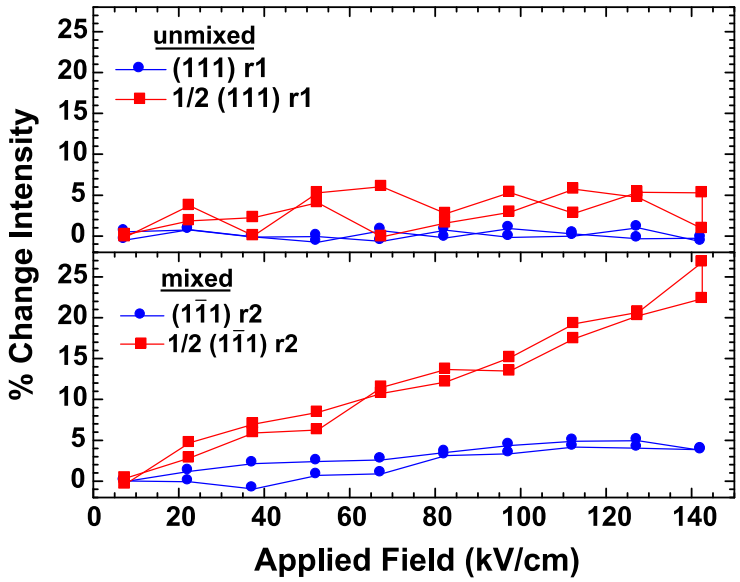

Figure 5.11. Change in intensity of (111), (1-11), ½(111), and ½(1-11) reflections versus electric field.

The intensity of three out of the four reflections increases proportionally with the applied electric field. Only the (111) reflection does not measurably increase in intensity. The integrated intensity of the (1-11) reflection increases by 5% at 150 kV/cm. These are both allowed reflections which mainly consist of charge scattering, so the increased intensity

is caused by changes in the atomic positions within the unit cell. Atoms moved perpendicular to the (1-11) plane, but stayed the same distance away from the (111) plane.

The half-order reflections both increased more than the corresponding {111} reflections. The ½(1-11) reflection increased by 26%, more than any other reflection. The unmixed ½(111) also increases, but was difficult to accurately estimate the percent change at 150 kV/cm because of poor counting statistics. A least squares fit to a linear function estimates the maximum change to be 4.5%. The ½(111) was very weak, so we had to count for longer amount of time in order to measure the change. Longer counting times meant more pulses applied to the sample. 260,000 pulses had to be applied for the scan shown above. Applying this many low frequency pulses to the sample increased the leakage current. Large current through the film leads to dielectric breakdown and the development of a conducting paths which short the capacitor structure.

The linear response to electric field suggested the intensity change was related to strain. Strain is hysteretic with electric field, so we applied a field antiparallel to the polarization direction to see if the intensity change was hysteretic also. The intensity of the ½(1-11) reflection was measured for electric fields from -150 kV/cm to +250 kV/cm. The fractional change as a function of field was calculated as described above and the results are shown in Figure 5.12.

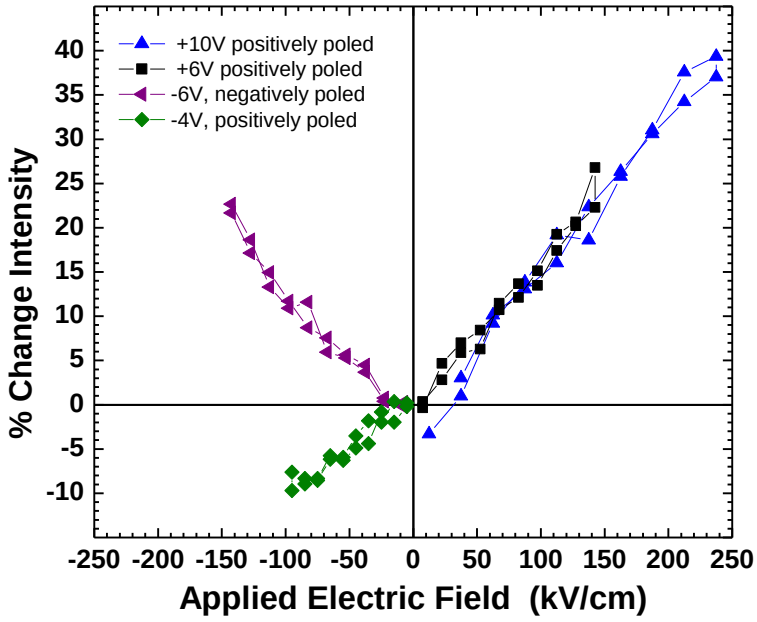

Figure 5.12. Intensity of ½(1-11) versus electric field. The intensity is hysteretic with electric field. The maximum voltage applied to the top electrode and the poling direction for each scan is listed in the legend.

The intensity of the ½(1-11) reflection exhibits hysteresis with electric field. The intensity increases when the polarization direction is parallel to the applied field, and decreases when they are antiparallel. The response is not symmetric about E=0 because the coercive field on the positive direction is much smaller than in the negative direction. No data for negative polarization direction and positive electric field are available because the polarization switched before the measurement could be completed.

The proportional increase in intensity and hysteretic response strongly suggests that the order parameter responsible for the half order reflections is coupled to the piezoelectric strain. Although the distortion is enhanced with increasing strain, it is not caused by epitaxial strain alone, since the ½{111} reflections are also observed in bulk $BiFeO_3$.

In order to determine which electrons contributed to the ½{111} reflections, we measured the intensities of the half order reflections as a function of energy near the Fe K edge. We observe a resonant enhancement of the intensity near the Fe K edge, demonstrating that scattering from electrons bound to the iron contributes to the ½{111} reflections.

5.6. Resonant diffraction and chemical shift of ½{111} reflections

The energy dependence of a diffraction peak gives information about the atomic scattering factors, absorption coefficients, and bonding states of the scattering electrons. Measuring the integrated intensity of a reflection near an absorption edge can give element specific information. The scattering factors dramatically increase at an absorption edge, enabling the experimenter to determine which electrons are contributing to a given reflection. In order to probe the source of scattering at the ½(111) reflection, we measured the intensity as a function of photon energy near the Fe K edge.

Previous x-ray absorption studies of $BiFeO_3$ thin films and powders show that the Fe K edge in $BiFeO_3$ shifts to higher energies than in pure Fe.[20] The intensity of the x-ray reflection depends on the atomic scattering factors. The imaginary part of the dispersion correction, f'', is proportional to the absorption cross section. The intensity of reflections that depend on the iron scattering factor is expected to dramatically change at transition edges. The previous studies also reveal a small peak in the absorption at 7.11 keV, below the observed K edge.[20] This peak corresponds to the Fe 1s $\rightarrow$3d transition, which is forbidden to electric dipole transitions.

We measured the intensity of the ½(111) as a function of energy in the (111) film and the 600 nm (001) film. *θ-2θ* scans over the reflections were taken at each photon energy. The undulator energy was tuned to 7.1 keV and was held fixed during energy scans. The undulator produces the most photons at the tuning energy, but the bandwidth is large enough to create appreciable intensity, even at energies of approximately 50 eV from the photon energy with highest intensity.[21] The incident beam energy was scanned by changing the monochromator angle. The monochromator was calibrated by measuring the intensity of x-rays transmitted through a Fe foil and varying the energy over the Fe K edge at 7.112 keV.

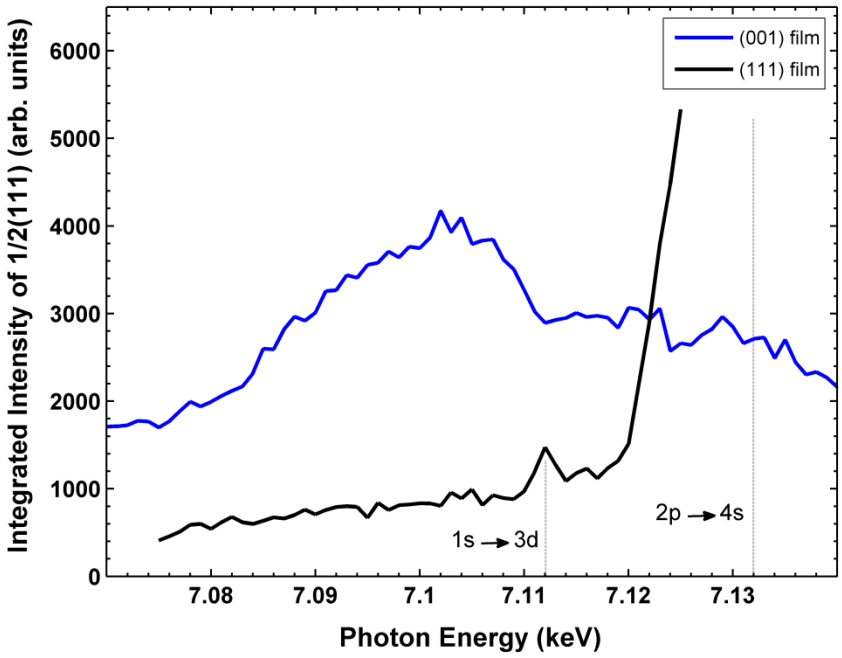

Figure 5.13. Intensity of ½(1-11) reflection versus energy for the 600 nm (001) film and the intensity of the ½(111) reflection from the (111) film. Dotted lines indicate the energies of electronic transitions near the Fe^{3+} K edge in powder $BiFeO_3$ measured using XANES (from Lee et al.[20]). The ½(111) reflection from the (111) film increases in intensity at the absorption edges in the powder sample. The ½(111) reflection from the (001) film increases intensity at a much lower energy.

We find that the intensity of the ½(1-11) reflection increased near the Fe K edge. Figure 5.13 is a plot of the integrated intensity of half order reflections as a function of x-ray photon energy. The multiple scattering ½(111) reflection from the (111) oriented $BiFeO_3$ film was acquired with an unfocused beam and is a measure of charge scattering from allowed reflections. The ½(1-11) reflection in the (001) film B-180-C was measured using a focused beam. This indicates that the electrons contributing to this reflection are excited into Fe orbitals. There is some modulation of these electrons which scatters x-rays at the ½(1-11) wavevector. The resonant enhancement at the Fe K edge implies that these electrons are bonded to the iron cations.[4]

Accurately comparing the intensities at different energies is complicated because the performances of the undulator, monochromator, and ion chamber all depend on photon energy. For example, the counting efficiency (number of counts per photon) of a typical ion chamber using nitrogen gas will change by 10% over the 100 eV range scanned here.[22] Since we did not measure the energy dependent characteristics of the monochromator or the ion chambers, intensities are simply normalized to the current in the storage ring. Each point in Figure 5.13 represents the summed intensity over a θ-2θ scan at a given energy, normalized to the storage ring current.

The (111) films also show a resonant enhancement of the intensity of the ½(111) reflection at the Fe^{3+} K edge and at the pre-edge peak. The increase in intensity from the (001) film is shifted by about 200 eV and shows no pre-edge peak. Measurements at different locations on the sample all increase in intensity at 7.085 keV, although the width of the resonant enhancement varies. The intensity variations above 7.09 keV are different at

each place on the sample. This suggests that the local bonding environment of atoms contributing to the ½(111) reflection is inhomogeneous.

Variations in local bonding environments can be caused by any change in the lattice. For example, atoms near a Frenkel defect, twin boundary, or miscut dislocation have different bonding states than in the middle of a bulk single crystal.[23] Oxygen vacancies could be responsible for variations in the local bonding. Mixing between the O 2p orbital and Fe 3d orbitals have been reported in materials like Fe_2O_3 which also contain octahedrally coordinated Fe^{3+} ions.[24] An oxygen vacancy site would shift the energy states of neighboring Fe^{3+} ions, affecting the resonant scattering at the pre-edge feature.[25]

The resonant enhancement near the Fe K edge in Figure 5.13 indicates that some of the electrons contributing to the ½(111) are either bound to iron or are part of a covalent bond with iron. The ½(111) of the $BiFeO_3$ film has a resonant enhancement at 7.08 keV, indicating that these electronic states are different from those contributing to multiple scattering. The intensity of the ½(111) versus photon energy was measured at several places on the sample surface with the focused beam. The onset of the resonant enhancement always started at 7.08 keV, but the width of the peak varied. Changes in the resonant enhancement at different places in the (001) film show that the electronic states vary spatially as well.

5.7. Structural distortion models for ½(hkl) reflections

The ½{111} and ½{333} reflections are a signature of a distortion of $BiFeO_3$ from the reported R3c symmetry. We considered three possible sources of scattering which would

contribute to the observed intensity at the half order reflections: antiparallel cation displacements, rotations of the oxygen octahedra, and anisotropy in the atomic scattering factors. Structure factors for each model were calculated for the ½{111} reflections. The details of each model are discussed below, along with the supporting and detracting evidence. We believe antiparallel cation displacements to be the most likely source of scattering at the ½{111} reflections.

5.7.1. Antiparallel cation displacements

Moving two cations in neighboring perovskite unit cells in opposite directions breaks the symmetry and can produce reflections at ½(*hkl*) wavevectors. The structure factor of a modified unit cell with antiparallel displacements of the iron ions was calculated. I focused on displacements of the Fe^{3+} cation because of the resonant enhancement of the ½(1-11) intensity near the Fe K edge. Displacements within the (111) plane were ruled out because they produced no intensity for the ½(111) reflection. Cation displacements of 0.1 Å in opposite directions along the [111] and [001] directions produce reflections a factor of 10^4 to10^5 times less intense than the {111} type reflections, similar to what we observe in the bulk. Displacements of 0.2 Å produce half order reflections 10^3 times less than the intensity of the {111} family of reflections. These intensities are similar to the intensity of the ½(1-11) reflection observed in the 400 nm film. Antiparallel displacements of Fe ions could be the structural distortion that causes the ½{111} reflections.

Charge disproportionation is known to cause displacements of the B site cations in perovskite materials. Charge disproportionation is a redistribution of charge such that two

chemically distinct sites exist for one element in the material. It is observed in some perovskite materials including $BaFeO_3$,[26] $CaFeO_3$,[27] $BaBiO_3$,[28] and $YNiO_3$.[29] In hexagonal $BaFeO_{2.91}$, oxygen deficiencies are accommodated by charge disproportionation of the iron ions, which nominally have a 4+ oxidation state.[26] Alternating sheets of Fe^{+4+r} and Fe^{+4-r} parallel to the hexagonal (001) planes are formed. The different valences affect the Fe-O bond length; Fe^{+4+r} ions have shorter bond lengths due to increased Coulombic repulsion and Fe^{+4-r} ions have longer bond lengths.

We propose that the ½{111} reflections in $BiFeO_3$ are a signature of antiparallel displacements of the iron cations induced by a reordering of charge, similar to charge disproportionation. In $BiFeO_3$ thin films, oxygen vacancies change the oxidation state of the neighboring cations from Fe^{3+} to Fe^{2+}. Iron ions with a nominal 2+ valence would be displaced from the atomic positions in the rest of the film, so that they had longer bond lengths than those with Fe^{3+} valence states. Ordering of these displacements would produce a reflection at the ½(111). The intensity would be dependent on the atomic scattering factors of Fe^{2+} and Fe^{3+} ions. Our observations of the resonant intensity of the ½(111) near the Fe K edge are consistent with this explanation. The dispersion correction f'' of octahedrally coordinated Fe^{3+} in Fe_3O_4 has a peak below the Fe K edge which is 200 eV wide.[30] The enhancement of the ½(111) between 7.0 and 7.2 keV would be explained by this resonance.

5.7.2. Anisotropic octahedral rotations

Structure factors for $BiFeO_3$ with several variations of rotation patterns of the oxygen octahedra were calculated in order to determine whether these rotations could be responsible for the ½ {111} and ½{333} reflections. In bulk $BiFeO_3$, oxygen octahedra in neighboring unit cells are rotated in opposite directions about the $[111]_{pc}$ axis. When the rotations about each axis are exactly equal, the ½(*hhh*) reflections are not allowed. When the rotations are anisotropic, however, the ½(111) is slightly allowed. Hatt and Spaldin suggest anisotropic rotations of octahedra may help relieve small amounts of strain in perovskite films, even on cubic substrates.[31] The $BiFeO_3$ films are known to relax anisotropically because of the miscut of the $SrTiO_3$ substrate, so anisotropic rotations of the octahedra are likely as well.

In order to test this hypothesis, we calculated the structure factor of a modified perovskite cell in which the oxygen octahedra were rotated anisotropically. The positions of atoms in 2×2×2 pseudocubic unit cells of $BiFeO_3$ were calculated using the Megaw program.[32] Atomic positions were calculated by modifying a pseudocubic structure to include Fe^{3+} displacements, the interaxial angle of 89.4°, and rotations of the oxygen octahedra about the ***a***, ***b***, and ***c*** pseudocubic axes. The positions of the oxygen atoms were calculated as a function of octahedral rotation angles. The lattice constants *a*, *b*, and c were sets to the pseudocubic bulk value of 3.96 Å. The intensity of the ½{111} reflections were calculated using these new oxygen positions. When the rotations about the a, b, and c axes are all different, the structure factor for ½(111) reflections is non-zero. For example, rotations of 5°, 15°, and 20° (tilt system $a^-b^-c^-$) produce reflections 10^5 to 10^6 times less than

the {111} reflections. Many tilt patterns were tested, but the intensity of the ½(111) reflection no more than 10^{-5} times the intensity of the (111). While anisotropic rotation may contribute to the reflections we observe, they make up no more than 10% of the ½(111) intensity found in the 400 nm $BiFeO_3$ film.

We conclude that anisotropic rotation of the oxygen octahedra induced by epitaxial strain is not the sole source of scattering at the ½{111} reflections in $BiFeO_3$. Firstly, the rotation angles required to produce just 10% of the observed intensities are quite large. Secondly, the ½{111} reflections are still observed in the bulk sample that has no epitaxial strain at all. While anisotropic rotation of the oxygen octahedra may contribute to the intensity of the half order reflections, it is not the only source of scattering.

5.7.3. Anisotropic scattering factors

Anisotropy in atomic scattering factors causes reflections at ½(*hkl*) wavevectors. Anisotropy in the electronic susceptibility at x-ray frequencies makes the atomic scattering factor anisotropic as well.[33,34] The atomic scattering factor is commonly assumed to depend on photon energy and the magnitude, but not the direction, of $\boldsymbol{q}$. In fact, the atomic scattering factor is a tensor property which does depend slightly on the direction of $\boldsymbol{q}$ for several reasons, such as point defects and anisotropy in thermal vibrations.[33] The tensor nature of f can usually be ignored because the anisotropy is very small in the x-ray region, but it becomes more relevant near resonant energies. However, when the atomic scattering factor tensor has a lower symmetry than the unit cell, forbidden reflections can appear. Forbidden

reflections in YVO_3 caused by anisotropic scattering factor show a resonant enhancement near the vanadium K edge.[35]

We estimated the intensity of reflections in $BiFeO_3$ from anisotropic scattering factors. Dmitrienko suggests that the intensity of these reflections should be on the same order as the change in x-ray absorption for different polarization directions.[33] The absorption at the Fe K edge in a $BiFeO_3$ thin film was measured for s and p polarization of the x-rays by Lee et al.[20] At the maximum of the K edge reflection, the absorption changes by approximately 12%. Using Dmitreinko's rule of thumb and Lee's measurement of μ, we estimate a 12% change in f'' of iron at the K edge. Assuming that f' varies by a similar 12%, the predicted intensity would then be about 16 r_0^2. The observed reflections range from 16 to 20 r_0^2 and match the predictions for anisotropic scattering factor reflections quite well at the Fe K edge.

The anisotropy in the absorption coefficient vanishes at energies far from the edge, however, along with the intensity of the forbidden reflection. The XANES data for $BiFeO_3$ show that the polarization dependence of μ disappears within 10 eV of the resonant peaks.[20] The resonant enhancement of ½(111) in Figure 5.13 is 50 eV wide. Furthermore, we observe the ½(111) and ½(-111) in the bulk sample far from the Fe K edge at 8.05 keV at approximately the same intensities as at 7.1 keV. Anisotropy in the scattering factors may contribute to the resonant enhancement of the intensity near the Fe K edge, but it does not explain the non-resonant scattering of the ½{111} reflections.

5.8. Discussion

There are multiple sources of scattering at the ½{111} and ½{333} reflections. These reflections are more intense than expected for pure magnetic scattering. Non-resonant magnetic scattering calculations predict that magnetic reflections should be 10^8 times less intense than the {111} reflections. The observed half-order reflection intensities, however, range from 10^5 to 10^3 times less than the {111} reflections. It should be noted that magnetic scattering from antiferromagnetic Fe_2O_3 was observed to be one or two orders of magnitude more intense than the calculated value. De Bergevin and Brunel found magnetic reflections which were only five orders of magnitude less than the charge scattering.[15] Even with this additional 'fudge factor', the observed intensities are still 10 – 1000 times too large to be consistent with our magnetic scattering model. We conclude that there is another source of scattering contributing to these reflections in addition to any non-resonant magnetic scattering.

We eliminated several potential sources of scattering at the half order reflections. Higher harmonic x-rays were excluded by selecting only detected x-rays with the correct photon energy. Multiple scattering reflections were avoided by varying the diffraction geometry and choosing samples with smaller coherent regions and larger mosaic spreads. We chose reflections which did not have reflections from the pattern of octahedral rotations found in the literature. Changes in the octahedral rotation pattern may be present and contribute to the ½{111} reflection intensities, especially in the thin film samples. However, the reflections are also observed in the unstrained bulk sample so octahedral rotations induced by

epitaxial strain cannot be the only cause. Anisotropy in the atomic scattering factors would explain the intensity of these reflections near the Fe K edge. Far from the edge, this model predicts that forbidden reflections are orders of magnitude weaker than the intensities we observe at 7.08 and 8.05 keV. Differences in anisotropic scattering factors may contribute to the intensity of the ½{111} reflections near the Fe K edge, but are negligible in non-resonant scattering at these wavevectors.

Antiparallel displacements of the Fe^{3+} cations are consistent with our observations. In order to test this hypothesis, more ½(*hkl*) reflections should be measured to accurately refine the structure. Higher x-ray energies would allow access to many of these half order peaks. This should be done for thin films as well as single crystal samples. Monodomain samples will eliminate potential scattering from interference between coherent scattering of multiple polarization domains. The thin film sample should be grown on an (001) $SrTiO_3$ substrate miscut along the [110] direction to select a single ferroelectric polarization domain.[36] The single crystal sample should be poled before x-ray measurements to switch the ferroelectric domains into a monodomain state. In order to distinguish between antiparallel cation displacements and anisotropic scattering factors, the variation of the ½{111} reflections should be measured as a function of azimuthal angle.[33] This experiment should be conducted with a single crystal that has a large (111) face so the azimuthal rotation coincides with a rotation axis of the goniometer.

5.9. Summary

Half order reflections were observed in epitaxial $BiFeO_3$ thin films and bulk crystals at wavevectors corresponding to a doubling of the perovskite unit cell. ½{111} and ½{333} reflections are forbidden by the bulk R3c symmetry, but are commensurate with the antiferromagnetic ordering. ½{113} type reflections were also observed and are the result of rotations of oxygen octahedra.

½{111} reflections were characterized in order to determine their origin. The ½{111} reflections are more intense in partially relaxed thin films than in bulk samples. The energy dependence of the ½(111) intensity shows an enhancement at energies below the bulk $BiFeO_3$ Fe^{3+} K edge. The integrated intensity of the ½(1-11) reflection is proportional to the piezoelectric strain and even demonstrates a hysteretic effect when the electric field is antiparallel to the polarization direction. The ½(111) intensity changes only slightly when piezoelectric strain is applied.

A number of theories were explored in order to explain the unusually large intensity of the ½{111} and ½{333} reflections. Multiple scattering was ruled out in the (001) films by measuring the intensity dependence on azimuthal angle, but was found to be the origin of the ½(111) in (111) oriented films. Magnetic scattering calculations predict that non-resonant magnetic scattering contributes no more than 1% of the total intensity of these reflections in the bulk sample and (001) thin films. Anisotropic oxygen octahedral rotations contribute no more than 10% of the intensity found in thin film samples. Anisotropy in the atomic scattering factors could account for the resonant enhancement of the ½(111) intensities near the Fe K edge but it does not play a role in non-resonant scattering. The most likely cause is

antiparallel displacements of the Fe cations which are not included in current structural refinements of $BiFeO_3$. The antiparallel cation displacements could be caused by different valence states of Fe ions as a result of oxygen vacancies, similar to the charge disproportionation effect in $BaFeO_{0.91}$. We conclude that the current understanding of $BiFeO_3$ structure is incomplete and there are additional distortions present which have a periodicity twice the dimensions of pseudocubic unit cell, most likely of the iron and oxygen octahedra.

5.10. Chapter 5 references

[1] C. Michel, J.-M. Moreau, G. D. Achenbechi, R. Gerson, and W.J. James, *"The atomic structure of $BiFeO_3$,"* Solid State Commun. **7**, 701 (1969).

[2] R. Przeniosło, M. Regulski And I. Sosnowska, "*Modulation in Multiferroic $BiFeO_3$: Cycloidal, Elliptical or SDW?,"* Journal of the Physical Society of Japan **75**, 084718 (2006).

[3] M. Blume and D. Gibbs, "*Polarization Dependence of Magnetic X-ray Scattering*", Phys. Rev. B **37**, 1779 (1988).

[4] S. W. Lovesey and S. E. Collins, *X-ray Scattering and Absorption from Magnetic Materials*, (Oxford Publishing, 1996).

[5] M. Blume, "*Magnetic Scattering of X-Rays*", J. Appl. Phys. **57**, 3615 (1985).

[6] D. Lebeugle, D. Colson, A. Forget, M. Viret, A. M. Battaille, and A. Gukasov, "*Electric-Field-Induced Spin Flop in $BiFeO_3$ Single Crystals at Room Temperature*", Phys. Rev. Lett. **100,** 227608 (2008).

[7] Andrey Zheludov, website. Magnetic form factors on this site were calculated using empirical formulae given in P. J. Brown, *Magnetic form factors*, Section 4.4.5, *International Tables for Crystallography Vol. C* (A. J. C. Wilson, ed.), pp. 391-399. https://protos.ethz.ch/neutron/research/resources/formfactor/index/edit/fe3.gif downloaded 7/4/2011.

[8] F. Kubel, H. Schmid, "*Structure of a Ferroelectric and Ferroelastic Monodomain Crystal of the Perovskite $BiFeO_3$.*" Acta Cryst B. **46**, 698 (1990).

[9] S. Poot, *"Goniometric Apparatus for an X-ray Diffractometer,"* U.S. Patent number 3636347, (1972).

[10] E. D. Dufresne, http://sector7.xor.aps.anl.gov/manuals/bicron.pdf, downloaded 6/6/2011.

[11] A. M. Glazer, *"The Classification of Tilted Octahedra in Perovskites,"* Acta Cryst. B **28**, 3384 (1972).

[12] A.M. Glazer, "*Simple Methods of Determining Perovskite Structures*," Acta Cryst. A **31** 756 (1975).

[13] D. Tinberg, R. L. Jonson-Wilke, D. D. Fong, T. T. Fister, S. K. Steiffer, Y. Han, I. M. Reaney, and S. Trolier-McKinstry, "*Octahedral tilt transitions in relaxed epitaxial $Pb(Zr_{1-x}Ti_x)O_3$ films*", J. Appl. Phys. **109**, 094104 (2011).

[14] S.-L. Chang, *Multiple Diffraction of X-rays in Crystals*, (Springer-Verlag, Berlin, 1984).

[15] M. Brunel, F. de Bergevin, "*Diffraction of X-rays by Magnetic Materials. II. Measurements on Antiferromagnetic Fe_2O_3",* Acta Cryst. A **37**, 324 (1981).

[16] I. Sosnowska, T. Peterlin-Neumaier and E. Steichele, "*Spiral magnetic ordering in bismuth ferrite*," J. Phys. C: Solid State Phys. **15,** 4835 (1982).

[17] S. Lee, T. Choi, W. Ratcliff, R. Erwin, S. W. Cheong, and V. Kiryukhin, "*Single ferroelectric and chiral magnetic domain of single-crystalline $BiFeO_3$ in an electric field*," Phys. Rev. B **78**, 100101 (2008).

[18] A. J. Hatt, N. A. Spaldin and C. Ederer, "*Strain-induced isosymmetric phase transition in $BiFeO_3$*", Phys. Rev. B **81**, 054109 (2010).

[19] S. Tinte, K. M. Rabe, and D. Vanderbilt, "*Anomalous enhancement of tetragonality in PbTiO3 induced by negative pressure*", Phys. Rev. B 68,144105 (2003).

[20] D. Lee, M. G. Kim, S. Ryu, H. M. Jang, S. G. Lee, "*Epitaxially grown La-modified $BiFeO_3$ magnetoferroelectric thin films",* Appl. Phys. Lett. **86**, 222903 (2005).

[21] R. J. Dejus, I. B. Vasserman, S. Sasaki, and E. R. Moog, *"Undulator A Magnetic Properties and Spectral Performance,"* Argonne National Laboratory Technical Bulletin, TB-45 (2002).

[22] A.C. Thompson, "*X-ray Detectors*", in *X-ray Data Booklet*, (Lawrence Livermore National Laboratory, Berkeley, 2008). Information from the X-ray Data Booklet can be found online at http://xdb.lbl.gov/ .

[23] S. Karazhanov, Y. Zhang, L.-W. Wang, A. Mascarenhas and S. Deb, *"Resonant defect states and strong lattice relaxation of oxygen vacancies in WO_3,"* Phys. Rev. B **68**, 233204 (2003).

[24] D. M. Sherman, *"The electronic structures of Fe^{3+} coordination sites in iron oxides: Applications to spectra, bonding, and magnetism,"* Physics and Chemistry of Minerals **12,** 161 (1985).

[25] F. G. Requejo, J.M. Ramallo-López, A. R. Beltramone, L. B. Pierella, O. A. Anunziat, *"Fe-containing ZSM-11 zeolites as active catalyst for SCR of NO_x Part II. XAFS characterization and its relationshipwith the catalytic properties,"* Applied Catalysis A **266**, 147 (2004).

[26] K. Mori, T. Kamiyama, H. Kobayashi, K. Oikawa, T. Otomo and S. Ikeda , *"Structural Evidence for the Charge Disproportionation of Fe^{4+} in $BaFeO_3$,"* Journal of the Physical Society of Japan **72**, 2024 (2003).

[27] P. M. Woodward, D. E. Cox, E. Moshopoulou, A. W. Sleight, S. Morimoto, *"Structural studies of charge disproportionation and magnetic order in $CaFeO_3$,"* Phys. Rev. B **62**, 844 (2000).

[28] D. E. Cox and A. W. Sleight, *"Mixed-Valent $Ba_2Bi^{3+}Bi^{5+}O_6$ - Structure and Properties vs Temperature,"* Acta Cryst. B **35**, 1 (1979).

[29] J. A. Alonso, J. L. Garcia-Munoz, M. T. Fernandez-Diaz, M. A. G. Aranda, M. J. Martinez-Lope and M. T. Casias, *"Charge disproportionation in $RNiO_3$ perovskites: Simultaneous metal-insulator and structural transition in $YNiO_3$,"* Phys. Rev. Lett. **82**, 3871 (1999).

[30] A. I. Frenkel, J. O. Cross, D. M. Fanning, and I. K. Robinson, *"DAFS analysis of magnetite,"* J. Synchrotron Rad. **6**, 332 (1999).

[31] A. J. Hatt and N. A. Spaldin, "*Structural phases of strained $LaAlO_3$ driven by octahedral tilt instabilities*", Phys. Rev. B **82**, 195402 (2010).

[32] A. M. Glazer, "MEGAW: Computation of the effect of rotating octahedra in perovskites," http://www.amg122.com/programs/page10.html, downloaded 6/1/2011.

[33] V. E. Dmitrienko, "*Forbidden Reflections due to Anisotropic X-ray Susceptibility of Crystals*", Acta Cryst. A **39**, 29 (1983).

[34] A. Kirfel, A. Petcov and K. Eichhorn, *"Anisotropy of anomalous dispersion in X-ray diffraction,"* Acta Cryst. A **47**, 180 (1991).

[35] T. A. W. Beale, R. D. Johnson, Y. Joly, S. R. Bland, P. D. Hatton, L. Bouchnoire, C. Mazzoli, D. Prabhakaran, and A. T. Boothroyd, "*Resonant x-ray scattering from the 4p quadrupole moment in YVO_3*", Phys. Rev. B **82**, 024105 (2010).

[36] H. W. Jang, D. Ortiz, S. H. Baek, C. M. Folkman, R. R. Das, P. Shafer, Y. Chen, C. T. Nelson, X. Pan, R. Ramesh, and C. B. Eom, "*Domain engineering for enhanced ferroelectric properties of epitaxial (001) $BiFeO_3$ thin films*," Adv. Mater. **21**, 817 (2009).